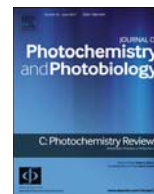




Contents lists available at ScienceDirect

Journal of Photochemistry and Photobiology C: Photochemistry Reviews

journal homepage: www.elsevier.com/locate/jphotochemrev

Tailored indium sulfide-based materials for solar-energy conversion and utilization



Jingjing Zhang^{a,b}, Hou Wang^{a,b,c,*}, Xingzhong Yuan^{a,b,*}, Guangming Zeng^{a,b},
Wenguang Tu^c, Sibow Wang^c

^a College of Environmental Science and Engineering, Hunan University, Changsha 410082, PR China

^b Key Laboratory of Environment Biology and Pollution Control, Hunan University, Ministry of Education, Changsha 410082, PR China

^c School of Chemical and Biomedical Engineering, Nanyang Technological University, Singapore 637459, Singapore

ARTICLE INFO

Article history:

Received 11 July 2018

Received in revised form 25 October 2018

Accepted 10 November 2018

Available online 16 November 2018

Keywords:

Indium sulfide

Photoelectrochemistry

Photocatalysts

Solar cell

ABSTRACT

To relieve the growing pressure originated from the energy shortage and environmental issues, solar-energy conversion into chemical or electrical energy has undergone an unprecedented development as a promising strategy in recent years. Indium sulfide (In_2S_3), an efficient visible-light harvester, has been extensively investigated in the field of photoconversion, owing to the fascinating merits including superior photo-absorption coefficient, photoelectric sensitivity, favorable carrier mobility, moderate band gap, excellent stability, and low toxicity. To take full advantage of these properties and further expand beyond the existing short board like low quantum efficiency, various In_2S_3 -based functional nanostructures like nanoparticles, nanotubes, atomic two-dimensional sheets, and nanosheets-assembled complexes have been developed. Meanwhile, pleasurable characters of In_2S_3 have been modulated via defective engineering, doping, and hybridization (with inorganic materials or bio-molecules). Gratifyingly, In_2S_3 -based photocatalytic, photoelectrocatalytic and photovoltaic systems have made significant impact on the field of energy and environmental issues. Therefore, this review provides an overview of crystal and morphologic structures of pristine In_2S_3 as well as many outstanding properties. Moreover, the pristine In_2S_3 and its derivatives with diverse synthesis routes are systematically summarized. Further, the advancement of In_2S_3 -based photocatalytic, photoelectrocatalytic and photovoltaic systems, especially in environmental decontamination, artificial photosynthesis for renewable fuels and solar cells, are highlighted in detail. Ultimately, we conclude with a summary and propose some invigorating perspectives on the challenges from atomic (or macroscopical) structure modulation in material nature, photochemical behavior understanding to solar photovoltaic applications at the forefront of this research platform.

© 2018 Elsevier B.V. All rights reserved.

Contents

1. Introduction	2
2. Pivotal ingredients of indium sulfide-based photoconversion materials	3
2.1. Atomic and crystal structure	4
2.2. Intrinsic properties	4
2.2.1. Electronic, transport and band gap properties	4
2.2.2. Optical properties	5
2.3. Morphology modulation for diversified properties	5
3. A systematic summary of constructing In_2S_3 -based materials	5
3.1. Adjustment of phase structure and morphology for pristine indium sulfide	5
3.2. Heteroatom doping	7
3.3. Heterostructured hybrids	9

* Corresponding authors at: College of Environmental Science and Engineering, Hunan University, Changsha 410082, PR China.

E-mail addresses: huankewanghou024@163.com (H. Wang), yxz@hnu.edu.cn (X. Yuan).

<https://doi.org/10.1016/j.jphotochemrev.2018.11.001>

1389-5567/© 2018 Elsevier B.V. All rights reserved.

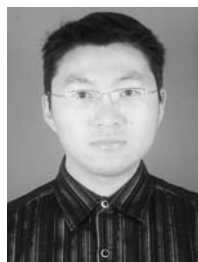
4.	Applications.....	11
4.1.	Photochemically environmental decontamination.....	11
4.2.	Artificially photosynthetic renewable fuels.....	14
4.2.1.	Hydrogen energy via water splitting.....	14
4.2.2.	Biology-assisted photocatalytic hydrogen and oxygen production.....	16
4.2.3.	Carbon-based fuel production from carbon dioxide reduction.....	18
4.3.	Solar cell.....	19
5.	Conclusions and perspectives.....	20
	Conflicts of interest.....	22
	Acknowledgments.....	22
	References.....	22



Jingjing Zhang received her B.S. in environmental engineering from Wuhan University of Science and Technology. She is currently a postgraduate student in Prof. Xingzhong Yuan's lab at Hunan University. Her research interests include the study of solar-energy conversion based on advanced nanomaterials.



Sibowang Wang received his Ph.D. degree from the College of Chemistry at Fuzhou University in 2016. At present, he is working as a research fellow at Nanyang Technological University, Singapore. His research interests mainly focus on the design, synthesis, and application of nanostructured semiconductors for photocatalytic CO₂ reduction and water splitting. He has published over 20 papers, with 1698 citations, H-index of 15.



Hou Wang received his Ph.D. degree at Hunan University in 2016. At present, he is working at Nanyang Technological University. His research focuses on the synthesis and application of advanced nanomaterials. He has published 90 peer-reviewed articles with a total citation of more than 3040 and H-index of 31.



Kingzhong Yuan obtained his Ph.D. degree from the School of Environmental Science and Engineering at Hunan University in 2003. He began his independent career in 1990 at Hunan University and was promoted to associate professor in July 1997 and professor in June 2004. His current research interests focus on the materials design and photochemical application. He has published over 270 papers, with 5374 citations, H-index of 41.



Guangming Zeng has been the head of the School of Environmental Science and Engineering at Hunan University since 1996. He received his Ph.D. degree from Wuhan University in 1988. He was invited as reviewers for over 50 journals and has over 320 scientific publications (journal & conference papers) with total citations at 31095 and H-index at 82. He is Highly Cited Researchers in 2017 from Clarivate Analytics. He is also the Most Cited Chinese Researchers in 2014–2017 according to Elsevier's statistics. His research interests focus on the development of novel functional materials for environmental and energy systems.



Wenguang Tu obtained his B.S. degree in 2010 from Southwest University, China. He is pursuing his Ph.D. degree under the guidance of Prof. Yong Zhou in ERERC, School of Physics, National Laboratory of Solid State Microstructures, Nanjing University, China. He is a research fellow at Nanyang Technological University (NTU), Singapore. His current research involves the synthesis of nanomaterials for photocatalysis. He has published over 60 papers, with 2639 citations, H-index of 24.

1. Introduction

Energy consumption and the increasing environmental pollution have become two of the world's largest crises we face today. Splitting water into hydrogen via simply using solar energy and inorganic semiconductors is so fascinating for renewable energy applications since the discovery of photoelectrochemical water splitting on TiO₂ electrode in 1972 [1–3]. Thereafter, the photosensitive semiconductor-based photocatalytic, photoelectrochemical and photovoltaic systems have been established for renewable solar-energy conversion [4]. The solar-energy conversion into chemical or electrical form is available for immediate chemical/electrochemical reactions or for electric power accumulation [5–7]. Correspondingly, the derived photoconversion applications toward photochemically environmental decontamination, artificial photosynthesis for renewable fuels, and solar cells have gotten into a new period of vigorous advancement [8–11].

Generally, the solar-energy conversion reaction contains three successive processes [4,12,13]. Semiconductor absorbs photons whose energy is equal to or greater than the bandgap energy, leading to the transfer of electrons located in the valence band (VB) to the conduction band (CB) with positively charged holes left in the VB. Subsequently, the photogenerated electron-hole pairs separate spatially on the crystal faces or different components surface of the heterostructure, or by an internal electric field. Ultimately, respective holes and electrons participate in the redox reactions with the medium on the surface of the semiconductor, which means the accumulation of the solar energy is in the chemical form. Alternatively, the photoelectrons transfer into the electric circuit to generate a photocurrent in photovoltaic systems, resulting in the accumulation of the solar energy in the electrical form. Evidently, solar light absorption is the key to all photocatalytic, photoelectrochemical and photovoltaic photoconversion systems, while the semiconductor often suffers from low solar energy utilization efficiency [14]. For instance, titania exhibits photoactivity only in the ultraviolet (UV) light due to its wide band gap of 3.2 eV [13,15]. However, the UV light merely accounts for 5% of the total solar energy [16]. The visible (Vis) and near-infrared (NIR) light occupy the proportion of 46% and 49%, respectively [17,18]. Therefore, great passion has been devoted to the exploitation of novel semiconductor capable of being excited under visible and even the

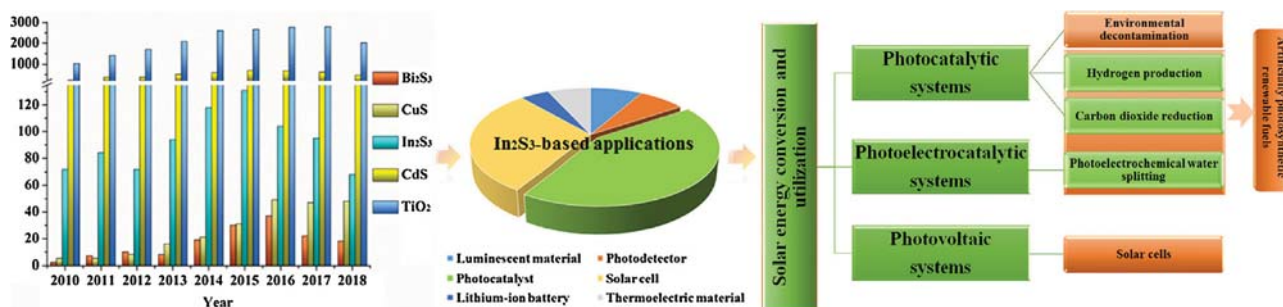


Fig. 1. The number of Bi₂S₃, CuS, In₂S₃, CdS, TiO₂ based research works from 2010 to 2018 in photochemistry field, and proportion of In₂S₃-based materials in each research fields, and schematic of the focused solar energy conversion system.

near-infrared light to achieve the maximum utilization efficiency of solar energy [19–23]. Exactly, as a Vis-light-responsive semiconductor, In₂S₃ has interested the global researchers due to its fascinating merits, such as outstanding absorption coefficient, photoelectric sensitivity, superior carrier mobility, moderate band gap, excellent stability and low toxicity [24–27]. Especially, our groups found that In₂S₃ had a wide response to the full solar spectrum via doping with rare earth ions Yb³⁺/Tm³⁺ and exhibited superior photoactivity even in NIR light, indicating In₂S₃ a promising material to realize the maximum solar energy [28].

Several outstanding characteristics regarding the compositions, structures and properties of indium sulfides are highlighted as follows. First, according to the atom stoichiometry in indium sulfides, there are three kinds of composition forms, InS, In₂S₃ and In₆S₇, with band gaps of ~2.44 eV, 2.0~2.3 eV, and ~0.93 eV respectively [24,29–31]. Suitable band gap provides the prerequisite conditions for facilitating the solar light absorption and conversion. Among them, the In₂S₃ becomes the most popular star owing to the unique crystalline structures, photoelectric properties, and stability. There are also five crystalline structures in the In₂S₃ including α -phase defect cubic structure (α -In₂S₃), β -phase defect spinel structure (β -In₂S₃), γ -phase layered hexagonal structure (γ -In₂S₃), ϵ -phase rhombohedra structure (ϵ -In₂S₃) and Th₃P₄-type phase cubic defect structure (Th₃P₄-In₂S₃) [32]. Second, a host of vacancies (e.g. sulfur vacancy, oxygen vacancy, indium vacancy) in ordered In₂S₃ crystals can not only exhibit electron affinity and serve as electron traps, but also favor for the formation of a transitionally defect band above the VB of In₂S₃ nanoparticles, providing a favorable platform for carrier mobility from UV region to NIR light irradiation [33]. Due to the formation of trapping levels within the bandgap of In₂S₃, a host of the surplus energy of excited electrons/holes could be captured in Coulomb repulsive centers. In turn, more electron/hole pairs are excited by the absorbed surplus energy, boosting the excellent photocurrent capability and photoelectric sensitivity of In₂S₃ [24]. Third, In³⁺ has much lower toxicity compared to Cd²⁺ and Pb²⁺ ions, which means less secondary pollution brought about in the photoconversion process using In₂S₃-based nanostructures [32].

Nevertheless, similar to another narrow band gap photosensitive semiconductor, the pure In₂S₃ also possesses low quantum efficiency due to the rapid recombination of photo-generated electrons-holes pairs [26]. Moreover, In₂S₃ suffers from the photo-corrosion inevitably as a metal chalcogenide semiconductor, especially in a strong oxidizing condition where S²⁻ could be easily oxidized to solid S accompanied with the elution of In³⁺ [34,35]. To improving quantum efficiency and photochemical stability, many significant breakthroughs on In₂S₃-based nanostructures have been made by controlling the crystalline structure and morphology, introducing metal impurities (doping) or constructing In₂S₃-based heterostructures.

According to the data from *Web of Science* in Clarivate analytics (Fig. 1), over a thousand papers on In₂S₃-based materials have emerged in a few years from the start of the studies to an explosive growth. Although much attention has been focused on the field of CdS and TiO₂, In₂S₃-based materials are still attractive in comparison to Bi₂S₃ and CuS due to good photosensitivity, stable chemical and physical characteristics, and low toxicity. These research works have exploited the maximum employ of In₂S₃-based materials as photocatalyst, solar cell component, lithium-ion battery, thermoelectric material, photodetector, and luminescent materials. Among them, the applications for solar energy conversion as photocatalyst and solar cell component occupy a proportion of 43% and 30%, respectively. Through the photocatalytic reaction, various environmental pollutants including organic and inorganic contaminants and harmful biota in air and water could be eliminated. And the abundant water resource and greenhouse gas could be transformed into renewable fuels via photocatalytic or photoelectrocatalytic process [36–39]. Solar cells can transform solar light energy into electric power to favor the growing demand. However, the thorough summary and assessment on the recent breakthroughs towards the In₂S₃-based photoconversion systems remain a gap in the knowledge base.

Herein, this review begins with an overall description of microscopic crystal structures and macroscopic morphologic structures at different dimensionalities, as well as the properties of pure In₂S₃ nanostructures. Then the synthesis and characterization of pure In₂S₃, doped In₂S₃, and In₂S₃-based composites are discussed. Further, the remarkable progress in photochemically environmental decontamination, artificial photosynthesis for renewable fuels, and solar cells are highlighted. More importantly, many interesting outlooks on the challenges from atomic (or macroscopic) structure modulation, photoconversion behavior understanding to new applications at the forefront of this research platform have been energetically proposed. It is anticipated that this review can stimulate a new doorway to develop the next generation of indium sulfide-based photoconversion systems with ameliorated performances by harnessing the excellent structural, electronic, and optical characters for green and sustainable development without environmental detriment.

2. Pivotal ingredients of indium sulfide-based photoconversion materials

In order to have a deep understanding of In₂S₃-based photoconversion materials, it is crucial to make clear the atomic and crystal structures which is closely bound up with the electronic, transport and optical properties. Macroscopic morphology of materials at different dimensionalities is also a nonnegligible factor in modulating these properties. Accordingly, the following section sheds light on the atomic and crystal structure, properties, as well as properties modulation based on morphology.

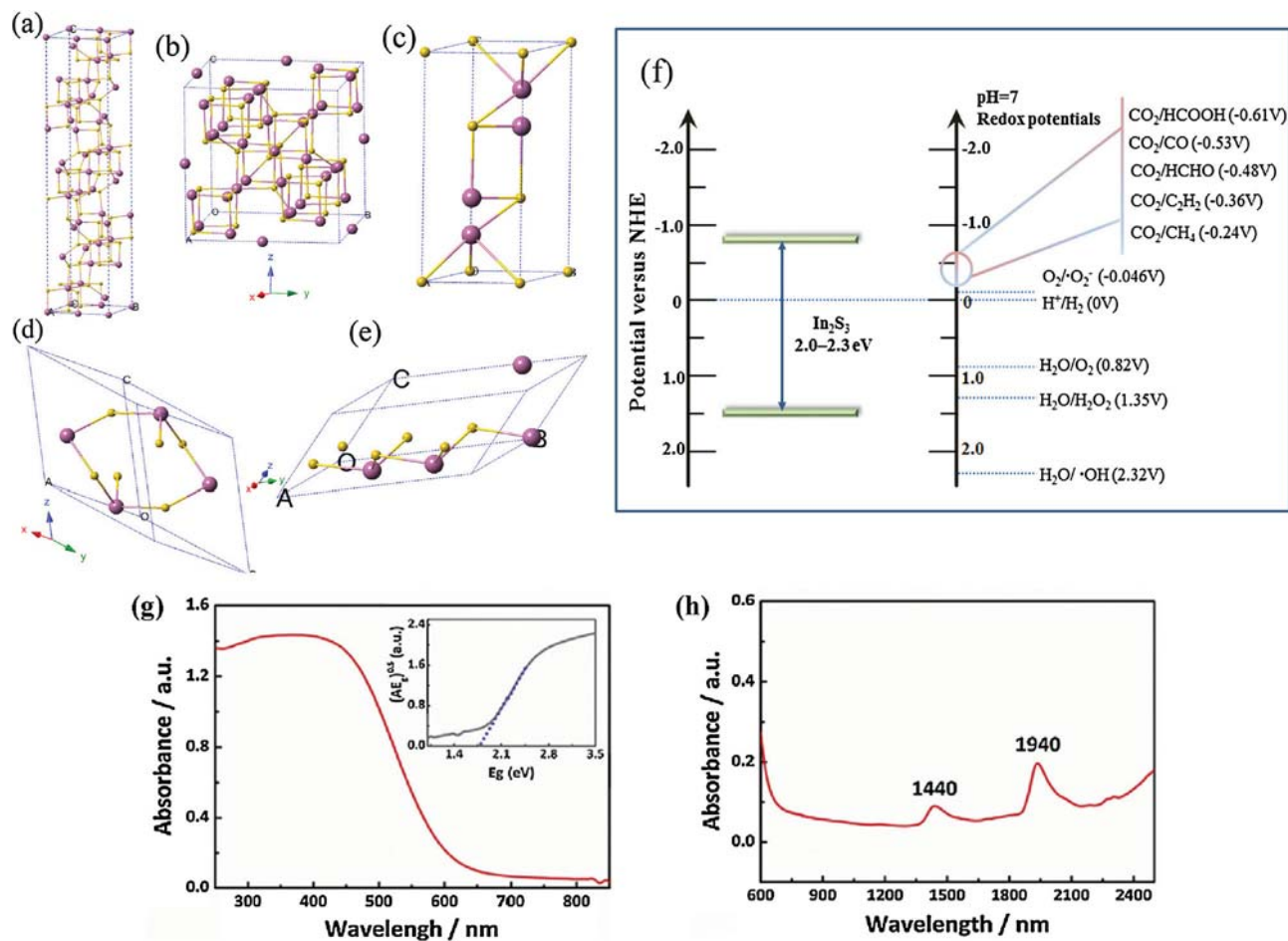


Fig. 2. Crystalline structures of In₂S₃: (a) tetragonal In₂S₃, (b) cubic In₂S₃, (c) trigonal In₂S₃, (d) hexagonal In₄S₆ and (e) monoclinic In₄S₆. Yellow and purple balls stand for sulfur and indium atoms, respectively. (f) Conduction band and valence band potentials of In₂S₃ relative to energy levels of the redox couples. (g) UV-vis DRS spectrum and (h) Vis-NIR DRS spectrum of In₂S₃ nanoparticles. Adapted with permission [33]. Copyright 2015, Elsevier.

2.1. Atomic and crystal structure

There are five crystalline structures for In₂S₃ materials (Fig. 2a–e). At room pressure, the phase of In₂S₃ is ordered by reaction temperature as α -In₂S₃, β -In₂S₃ and γ -In₂S₃, which will transform into the ϵ -In₂S₃ and Th₃P₄-In₂S₃ under high-pressure condition [40–42]. The β -In₂S₃ with tetragonal crystalline structure is stable up to 420 °C [43]. Above 420 °C, the disordering of vacancies in the tetrahedral cell proceeds and the tetragonal β -In₂S₃ transform into cubic β -In₂S₃ and cubic α -In₂S₃ with a different lattice constant [42]. The γ -In₂S₃ with layered hexagonal crystal structure appears above 750 °C [42]. And modified γ -In₂S₃ with trigonal crystalline structure is obtained above 1049 °C [44]. The γ -In₂S₃ can also be stabilized at room temperature if the In atoms are partly replaced by As, Sb or Bi [41]. What's more, the monoclinic ϵ -In₂S₃ can be prepared at 35 Kbar and 500 °C and the cubic Th₃P₄-phase In₂S₃ with high density and substantial coordination numbers is obtained at 356 Kbar [41,42].

Among the different phases, the β -In₂S₃ with stable and defective spinel structure at room temperature attracts the most considerable attention because of optimal photoelectric properties [45]. β -In₂S₃ crystal is obtained either in the tetragonal or cubic form [46]. In the tetragonal form, only 2/3 of the tetrahedral sites are occupied with indium atoms, the other 1/3 site is empty to maintain the stoichiometry of In₂S₃, thus leading to a large number of indium vacancies ordering in β -In₂S₃ crystals [47]. Nevertheless, all octahedral sites are filled by indium atoms in the octahedral

form. The cubic form hence arises out of vacancies disordering in the octahedral cation sites [47]. Selective tuning in the crystal phase of β -In₂S₃ can be achieved via a solvothermal method using task-specific ionic liquids as structure directing agents which is expounded in Section 3.1. [48]. Notably, the positions and arrangement characteristics of vacancies in n-type β -In₂S₃ play decisive roles in nearest-neighboring atoms and even all the atoms in the molecular layer, further affecting the electronic structure and photophysical properties [43]. For example, it was proposed that the sulfur-bridged indium ions were crucial to transfer the photogenerated charges. The presence of ordered indium vacancies blocked the transportation efficiency of the carrier transfer pathway [43]. Therefore, it is expected that the modulation of atomic arrangement and vacancies distribution in In₂S₃ crystalline structures is a feasible mode for rationally designing more efficient photoconversion systems.

2.2. Intrinsic properties

2.2.1. Electronic, transport and band gap properties

Notably, the β -In₂S₃ exhibits n-type conductivity, while the α -In₂S₃ and γ -In₂S₃ exhibits p-type conductivity [49]. A large number of intrinsic vacancies originated from the defect spinel structure of β -In₂S₃ shows electron affinity and can act as electron traps, thus endowing β -In₂S₃ semiconductor with relatively attractive electrochemical properties [47]. The carrier concentration of β -In₂S₃ is about 10¹⁸ cm⁻³ and the carrier mobility of β -In₂S₃ could

reach as high as $17.6 \text{ cm}^2 \text{ V}^{-1} \text{ s}^{-1}$ [24,29,50]. Electrical transport properties are related to the Seebeck coefficient and electrical conductivity [51]. The absolute value of the Seebeck coefficient for $\beta\text{-In}_2\text{S}_3$ exceeds 250 mVK^{-1} over a wide temperature range from 400 K to 700 K [52]. On account of the low coordination numbers of the In3 and S2 atoms, the corresponding In3-5s states and S2-3p states at different lattice positions crucially contribute to the composition of band-edge electronic structure, resulting in special optical and optoelectronic properties [53]. According to the calculated band structure of $\beta\text{-In}_2\text{S}_3$ by density functional theory (DFT), the VB and CB position edge with the measured value of 1.37 eV and -0.97 eV respectively, are mainly formed by the hybridization effect between S-3s, S-3p states and In-5s, In-5p states [26,53]. Within the band gap (2.0–2.3 eV) of $\beta\text{-In}_2\text{S}_3$ (Fig. 2f), an indirect band gap of about 1.977 eV is observed in both calculated and experimental research [54]. The trapping levels and intermediate band (IB) are formed due to the defect spinel structure [24,29]. For example, the defective bulk $\beta\text{-In}_2\text{S}_3$ exhibits distinctive photoconductivity response below the band gap, which is induced by the multiphoton absorption through IB, and shows a broadband spectral response [24,55].

2.2.2. Optical properties

Absorption coefficient, dielectric functions, and transmittance spectra are the basic factors related to the optical properties [49]. As shown in the UV–vis diffuse reflectance absorption (DRS) spectrum (Fig. 2g), In_2S_3 nanoparticles exhibit significant absorption up to 650 nm, nearly covering the entire visible region [33]. In the NIR light region (Fig. 2h), due to the presence of a defect band located above the VB, In_2S_3 nanoparticles display two obvious broad absorption peaks at 1440 nm and 1940 nm [33]. The dielectric function sensitive to the electronic band structure of the crystal is used to describe the response to an electric field [49]. Particularly, $\beta\text{-In}_2\text{S}_3$ photodetector shows a photo-responsivity of 137 A W^{-1} , an external quantum efficiency of $3.78 \times 10^4 \%$, and a detectivity of 4.74×10^{10} Jones, accompanied with a fast rise and decay time of 6 and 8 ms, respectively [24]. The $\beta\text{-In}_2\text{S}_3$ has a transmittance of 85% incident light in the NIR region, 50% Vis light and falls to 20% in UV region [49,56]. The morphology of In_2S_3 nanostructure also makes a great influence on the optical transmittance [56]. Compared with tilted nanorods, the screws and vertical nanorods possess less incident light transmittance, and more more light-absorbance [56].

In short, due to the favorable electrical conductivity and the broad photoresponse region, In_2S_3 -based materials have been widely used in various fields including solar cells, lithium-ion batteries, photodetectors, luminescent materials, and photocatalysis. Designing In_2S_3 crystals in the desired crystal phase or morphologic dimension with optimal properties are promising for further augmenting the performance of these technologies.

2.3. Morphology modulation for diversified properties

Nanostructures with proper morphologies not only make influence on the light harvest efficiency but also promote mass-transfer and separation of photocarriers [57,58]. Significant advancements have been made in designing In_2S_3 nanostructures and investigating relations between morphology characteristics and photo (electro) chemical performance. As shown in Fig. 3, the In_2S_3 materials with various morphologic structures can be categorized into zero-dimensional structure (e.g. quantum dots, nanoparticles, nanospheres), one-dimensional structure (e.g. nanowires, nanorods, nanotubes), two-dimensional structure (e.g. nanobelts, nanosheets, nanoplates, nanoflakes), three-dimensional structure (e.g. nanocubes, nanoflowers, hollow microspheres) [24,27,29,33,45,59–67]. With a large exciton Bohr diameter of

33.8 nm, the size of zero-dimensional (0D) In_2S_3 nanoparticles is always smaller than or close to the Bohr radius, thus quantum confinement effect is distinctly induced [68]. The tetragonal In_2S_3 nanoparticles with a single crystalline phase and defective nature are active over the full electromagnetic spectrum [33]. In terms of one-dimensional (1D) structure nanocrystalline materials, there are several advantages including efficient electron transport, facile strain relaxation on flexible substrates, and a short diffusion length perpendicular to charge collecting substrate, therefore hindering the recombination of the electron-hole pair [61,69]. As a contrast, two-dimensional (2D) nanostructures, especial in the nanosheet with atomic thickness, have enough specific surface area ($12 \text{ m}^2 \text{ g}^{-1}$) and an opening flat architecture to capture electrons from the redox couples [25]. As a result, 2D nanostructures acquire better electronic mobility, more available active sites, strong light-matter interactions, favorable transparency and mechanical flexibility [24,57,70]. Under the same conditions, 2D In_2S_3 nanosheets were found to exhibit the best electrochemical performance compared with 1D nanotubes and 3D nanoflowers [71]. Usually, three-dimensional (3D) structure of In_2S_3 materials assembled from low dimensions via an orderly manner have a large surface area with capacious interspaces and could afford a direct electron transport path when the main junction remain epitaxial [72]. Herein, 3D nanostructures are able to provide more “space” towards the transportation or storage for the electron/ion, gas and liquid [73]. Different morphologies of In_2S_3 nanocrystals from 1D to 3D structures are tunable by controlling the synthesis strategies and reaction conditions [45,74]. For instance, it was discovered that the morphologies of In_2S_3 were sensitive to the solvothermal reaction parameters including temperature, sulfur source and solvent, additional metal ion (e.g. Ca^{2+} , Al^{3+}), organic ligands and an ionic liquid, which is described in Section 3.1. [45,71,62,65,75].

Hence, to optimize the favorable properties and performances of In_2S_3 -based materials, it is vital to design In_2S_3 structures with a single dimension or mixed dimension according to the respective advantages.

3. A systematic summary of constructing In_2S_3 -based materials

Until now, tremendous efforts have been made to develop synthetic methods for pure In_2S_3 and its derivatives. Intuitively, the synthesis route adopted would influence the surface chemistry of materials and consequentially the function [7,76]. To fully exploit the advantages of In_2S_3 , especially in various composites, it is important to shed light on the synthesis, mechanism, and characterization.

3.1. Adjustment of phase structure and morphology for pristine indium sulfide

According to the difference in stoichiometry, binary indium sulfide exists in three composition forms, orthorhombic InS, monoclinic In_6S_7 , and In_2S_3 . The preparation of InS nanorods, nanotubes, platelets, and nanospheres was achieved via solution-phase reaction assisted by benzenethiol as a catalyst [31]. Besides, Revaprasadu et al. reported a single source route to synthesize InS nanoparticles [77]. In_6S_7 layered crystals were synthesized by Ho et al using chemical vapor transport (CVT) technology [30]. When the reaction kept 240 h at 750°C , large single In_6S_7 crystals was obtained [30]. Attracted by its superior properties, the various synthetic techniques have been rapidly developed to prepare In_2S_3 with different crystal phase or diverse morphologies at different dimensions, including dry synthesis and wet chemical methods. The dry synthesis includes spray pyrolysis, slurry painting, laser-

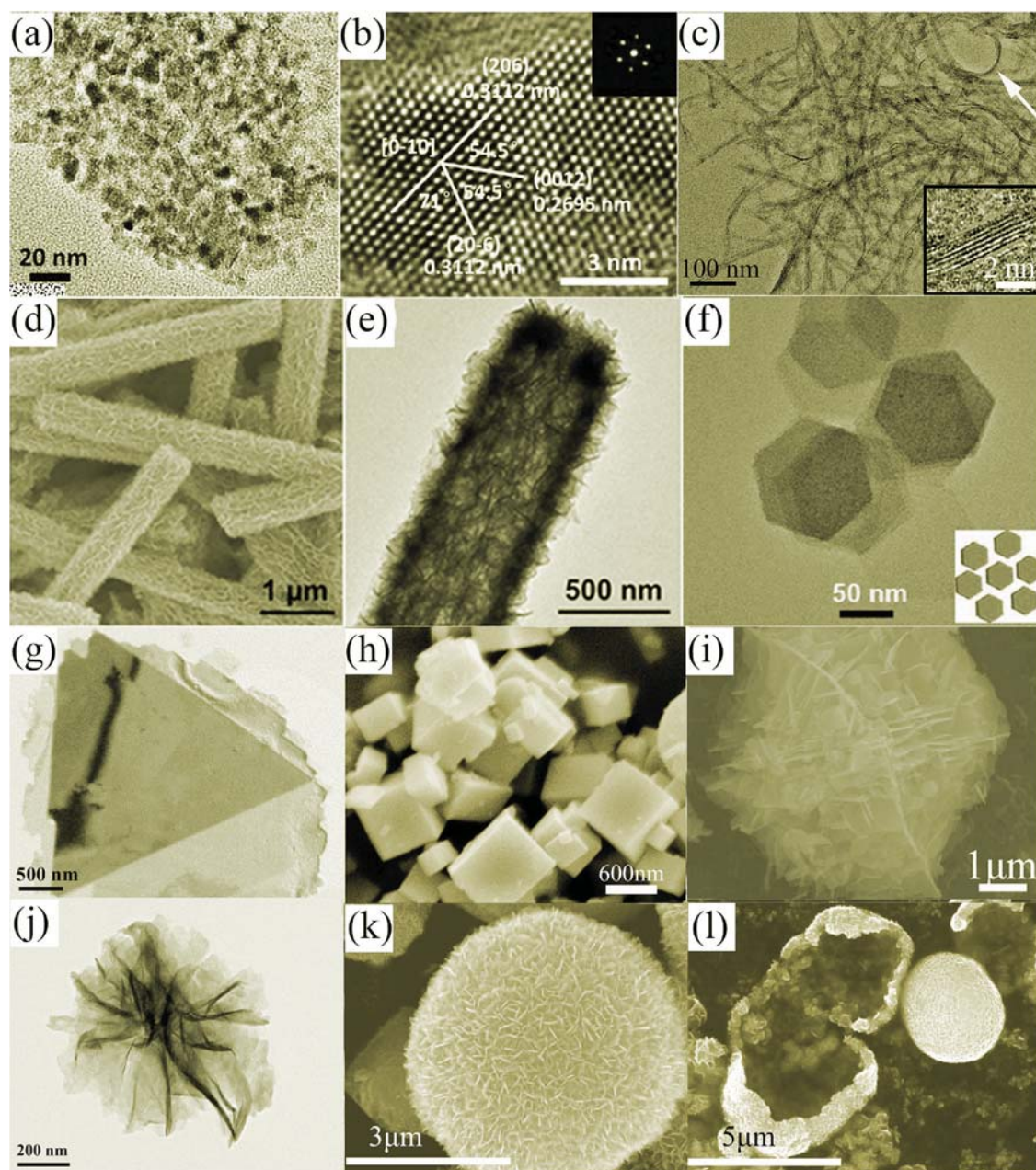


Fig. 3. Different morphologies of β - In_2S_3 : (a) TEM image and (b) HRTEM image of In_2S_3 nanoparticles. Reproduced with permission [33]. Copyright 2015, Elsevier. (c) TEM image of In_2S_3 nanobelts. Reproduced with permission [62]. Copyright 2015, Royal Society of Chemistry. (d) SEM and (e) TEM image of In_2S_3 nanotubes. Reproduced with permission [27]. Copyright 2017, American Chemical Society. (f) TEM image of In_2S_3 nanoplates. Reproduced with permission [64]. Copyright 2016, American Chemical Society. (g) TEM image of In_2S_3 flakes. Reproduced with permission [24]. Copyright 2017, Wiley. (h) SEM image of In_2S_3 nanocubes. Reproduced with permission [45]. Copyright 2012, Elsevier. (i) SEM image of In_2S_3 walnut-like microspheres. Reproduced with permission [65]. Copyright 2012, Royal Society of Chemistry. (j) TEM image of In_2S_3 nanoflower. Reproduced with permission [66]. Copyright 2017, Springer Science + Business Media. (k, l) SEM image of In_2S_3 hollow microspheres. Reproduced with permission [67]. Copyright 2011, American Chemical Society.

induced evaporation, sonochemical method, and chemical vapor deposition (CVD) [24,78–87]. Wet chemical methods are mainly involved in solvent-reduction route, hydrothermal or solvothermal method and chemical bath deposition [88–92].

Phase structure and composition may affect the photoinduced electron-transfer pathway [49]. It is necessary to rationally control the synthesis routes and conditions. Three crystal phases of In_2S_3 (α -, β -, or γ -) could be synthesized by direct reaction of the elements with the increase of temperature. The β - In_2S_3 was firstly obtained in 309 K and then the transitions of α -phase and γ -phase occurred at temperatures of 717 K and 1049 K, respectively [44]. Selective tuning of the tetragonal and cubic phase of β - In_2S_3 could

be realized by adding ionic liquids under solvothermal condition [48]. The alkyl side chain length and the aromatic π -stacking ability of 1-alkyl-3-methylimidazolium bromide ionic liquids ($[\text{C}_n\text{mim}]\text{Br}$, $n = 2, 4, 6, 8, \text{ and } 10$) was found to make an influence on crystal phase of In_2S_3 nanocrystals. Cubic β - In_2S_3 was obtained in the shorter alkyl side chain length ($n \leq 4$), while the tetragonal β - In_2S_3 polymorph formed in longer chain length of ionic liquids ($n \geq 6$) [48]. In addition, tetragonal and cubic phases β - In_2S_3 could be synthesized by a microwave-assisted solvothermal process in aqueous and methanol media, respectively [93]. In microwave condition, both water and methanol liquid were transformed into the vapor phase. With the vapor started cooling down, the crystal structure

came into being. The rapid release of water vapor energy induced the formation of vacancy disordered cubic β - In_2S_3 phase. While in the methanol media, it needed to spend too much time for the formation of vacancy ordering in tetragonal phase owing to the relatively slow cooling rates [93].

Morphology and geometrical structure of materials, closely related to the mass-transfer pathway during the chemical interaction, could be regulated via wet chemical methods, typically solvo/hydrothermal method [72–75]. The wet chemical technique is beneficial to prepare well-crystallized products at low temperatures and simply control the morphology and structure of products by adjusting the synthesis conditions such as sulfur source, solvent, reaction temperature, and templates [45,71,74,94–98]. The β - In_2S_3 quantum dots were synthesized in the sonochemical process. Heterogeneous sonochemical effects accelerated the nonspherical implosion of bubbles in liquid-solid interfaces, leading to the decrease of β - In_2S_3 quantum dots radius from 2.5 to 2.0 nm [99]. With the aid of oriented attachment of nanoparticles, the β - In_2S_3 nanotubes were prepared via an organic solution pyrolysis route, in which the β - In_2S_3 grown from hexagonal nanoplates to nanotubes simply by changing the reaction time [69]. Serving as a surfactant, oleylamine adsorbed preferentially on the {111} surface of In_2S_3 nanoparticles. Because of the low binding energy on the {111} surface, oriented attachment of β - In_2S_3 nanocrystals along the $\langle 110 \rangle$ axis induced the growth of In_2S_3 from nanoparticles to hexagonal nanoplates and finally formed nanotubes with reaction time increasing (Fig. 4a) [69]. Remarkably, hierarchical 1D cubic In_2S_3 nanotubes were synthesized through a template-assisted liquid phase sulfidation process [27]. Using In-based MOF (MIL-68) hexagonal prisms as the precursor, the obtained In_2S_3 1D nanotubes inherited the morphology from MIL-68 precursors with the diameter of 600 nm and rather rough surface with a shell thickness of about 100 nm (Fig. 3d and e) [27]. For 2D lamellate structure, In_2S_3 nanosheets was usually fabricated with the assistance of surfactant CTAB and the formation scheme was shown in Fig. 4b [97]. The CTA^+ was firstly ionized from CTAB, which owned a positively charged tetrahedron with a long C16 alkyl chain. Then, with the aid of CTA^+ , In_2S_3 crystal seeds were squeezed into layered nanosheets. Open lamellar In_2S_3 structures were finally formed due to the electrostatic repulsion and the steric hindrance of the CTA^+ ions [97]. Parallely, 2D β - In_2S_3 nanobelts and nanoflakes with a thickness of 2 nm were synthesized via oriented-attachment (OA) growth process controlled by Ca^{2+} and Al^{3+} metal ions respectively as shown in Fig. 4c and d [62]. In the early reaction stage of formation, octylamine molecules was deposited on the {110} planes of β - In_2S_3 nanoparticles, which induced OA growth of nanoparticles along the $\langle 001 \rangle$ direction. Then, the addition of Al^{3+} led to some of the octylamine molecules desorbing from {110} planes because of the combination between the octylamine and Al^{3+} . Partial {110} planes hence were exposed and caused OA growth of nanoparticles along the $\langle 110 \rangle$ direction. Finally, due to the concurrent OA growth along $\langle 001 \rangle$ and $\langle 110 \rangle$ directions, 2D β - In_2S_3 nanoflakes were obtained. While in Ca^{2+} solution, fewer octylamine molecules desorbed from the planes owing to the much lower atomic potential (Z/r) of Ca^{2+} than Al^{3+} metal ions. As a result, the OA growth along the $\langle 110 \rangle$ in the Ca^{2+} solution was much weaker, resulting in the formation of quasi-2D β - In_2S_3 nanobelts through the preferential growth along $\langle 001 \rangle$ direction [62]. As for 3D hierarchical structure, Wu et al. used inorganic-organic hybrid (InS-TETA, TETA = triethylenetetramine) as the precursor to prepare porous flower-like In_2S_3 via hydrothermal chemical transformation route at 180 °C (Fig. 4e) [100]. In the initial reaction phase, the InS-TETA decomposed into small nanoparticles and TETA molecules dissolved into deionized water. Induced by the TETA as capping ligands and nucleation centre, InS nanoparticles grew into 2D ultrathin nanosheets with a small size. The layered single-crystalline nanosheets with a diameter of

1.75 nm served as the building blocks to assemble into flower-like In_2S_3 (Fig. 4f) [100].

Differing from wet chemical methods, chemical vapor deposition (CVD) has also been used in the preparation of In_2S_3 -based materials [24]. In the years of 2004, Afzaal et al. firstly prepared 1D β - In_2S_3 nanorods via CVD using $[\text{Et}_2\text{In}(\text{S}_2\text{CNMe}^t\text{Bu})]$ as a single-source precursor. Noticeably, it was performed on a glass substrate, avoiding the use of toxic substances under 375 °C [87]. A facile space-confined CVD technology was further improved for controlled synthesis of ultrathin 2D β - In_2S_3 flakes [24]. As shown in Fig. 4g, the CVD system was equipped with two individually controlled heating systems, the precursors containing indium iodide (InI) and sulfur (S) powders were put in the two different heating zones, respectively [24]. Thereinto, the microreactor with two stacked mica substrates were then used to create a confined reaction space [24]. By optimizing the growth parameters including InI amount, growth time and gap size, a large amount of high-quality cubic β - In_2S_3 flakes with a single crystal and regular triangular shape had been obtained. The size of β - In_2S_3 flakes was 10 μm and the thickness was 1.5 nm (Fig. 4h) [24]. The obtained ultrathin β - In_2S_3 flakes exhibited unique defective structure and intrinsic optical properties [24]. However, some disadvantages including the relatively expensive equipment, complicated operation, and relatively high reaction temperature have gradually hindered the development. Synthetic methods for In_2S_3 have a great influence on its crystal structure, morphology, and properties. It is expected that continuing efforts are still required to accomplish a cost-effective and scale-up synthesis for multifunctional In_2S_3 . Especially, the preparation of atomic scale indium sulfide structures like clusters with different stoichiometry atomic ratio may become a new direction.

3.2. Heteroatom doping

Doping, designed by deliberately introducing impurities, is one of the most effective strategies to improve the spectral response of a photocatalyst and thus ameliorating photocatalytic efficiency of semiconductors [101–104]. Generally, the introduction of metal impurities inflicts splitting of crystal field in the host lattice structure, which would bring about several new energy levels within the band gap, subsequently make an influence on the absorption coefficient and electron motion [105,106]. Exactly, a large number of vacancies in the β - In_2S_3 crystal structure can act as a reservoir for the implant of metal ions intentionally as dopants [107]. In the past decades, there have been various methods developed for the synthesis of metal ions doped β - In_2S_3 , such as hydrothermal method, solid-state reaction method, gas-liquid phase chemical deposition and atomic layer deposition [52,108–114].

As an effective atomization doping method, a gas-liquid phase chemical deposition technology was frequently applied for the preparation of doped In_2S_3 nanoparticles by metal ions such as Ho^{3+} , Ce^{3+} , Tb^{3+} , Dy^{3+} , Tb^{3+} , Yb^{3+} and Tm^{3+} [113,115–117]. Take the case of the preparation of Ho^{3+} doped cubic In_2S_3 nanoparticles, the synthetic facility was shown in Fig. 5a [115]. Flowing H_2S gas was initiated and controlled by the chemical reaction between HCl and Na_2S solution. Under the help of ultrasonic nebulizer, the atomized reactive droplets including In^{3+} and Ho^{3+} cations complexes (the organic linker is β - $\text{HOCH}_2\text{CH}_2\text{SH}$) would react with the H_2S gas. Meanwhile, the dissolved S^{2-} anions prompted the complexes to gradually dissociate and form ionic bonds between In^{3+} and Ho^{3+} cations, thus resulting in the Ho^{3+} cations successfully entering into the host In_2S_3 lattice. The diameter of In_2S_3 : Ho^{3+} nanoparticles was 3–5 nm [115]. Additionally, different from the gas-liquid phase chemical deposition technology being aimed for the preparation of doped In_2S_3 nanoparticles, facile hydrothermal (solvothermal) route may be more suitable to fabricate doped β - In_2S_3 with 2D

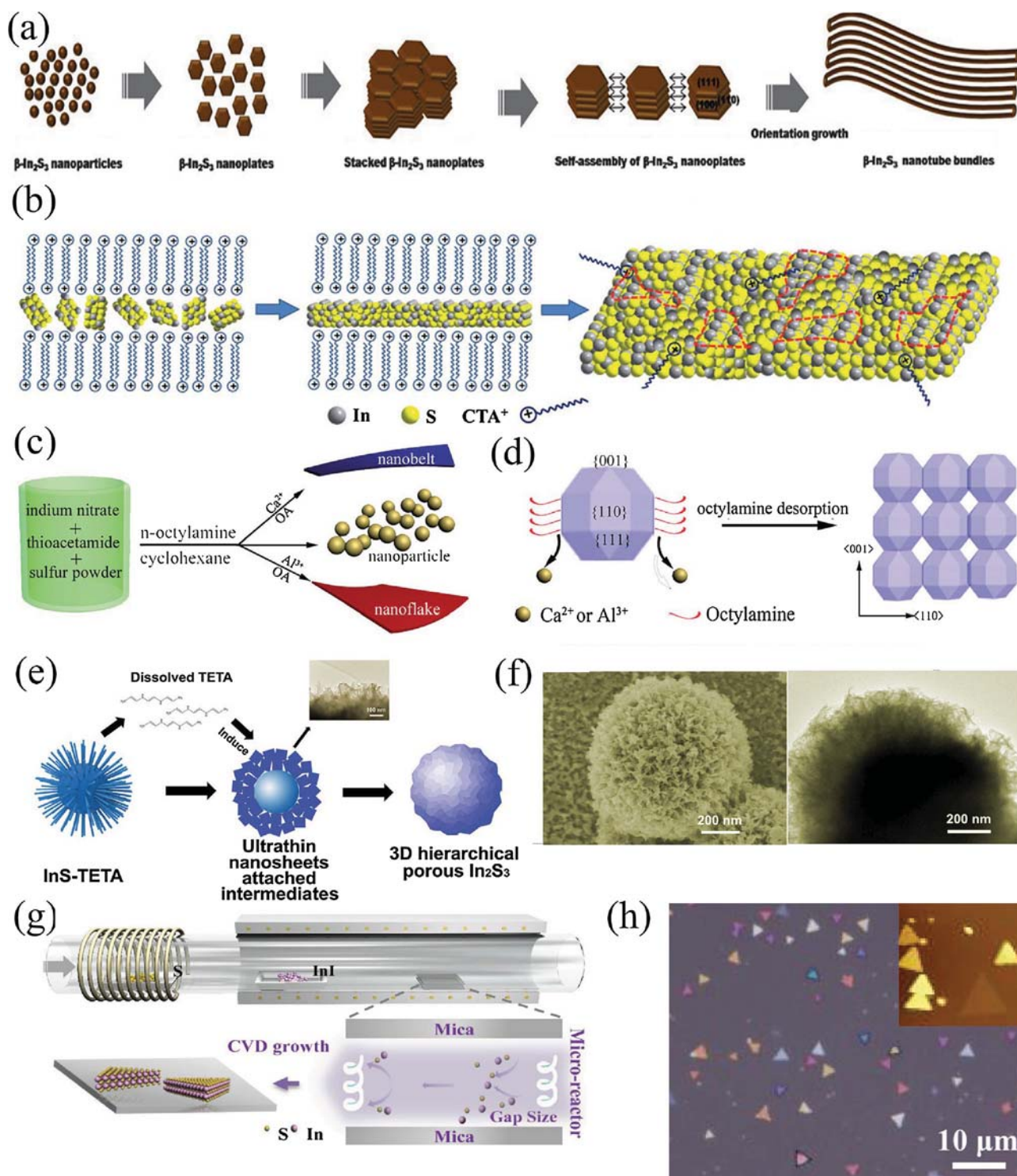


Fig. 4. (a) Formation scheme of In_2S_3 nanotubes. Reproduced with permission [69]. Copyright 2010, Royal Society of Chemistry. (b) Formation scheme of defective In_2S_3 nanosheets in highly concentrated CTAB solution. Adapted with permission [97]. Copyright 2016, Royal Society of Chemistry. (c) Formation scheme of In_2S_3 nanobelts, nanoparticles and nanoflakes. (d) Schematic mechanism of OA growth of 2D $\beta\text{-In}_2\text{S}_3$ nanocrystals. (e) Schematic illustration of the evolution mechanism of In_2S_3 microspheres through 2D ultrathin nanosheets. (f) SEM (left) and TEM (right) images of In_2S_3 microspheres. Adapted with permission [62,100]. Copyright 2015, Royal Society of Chemistry. (g) Schematic diagram of a space-confined CVD system and the microreactor constructed by two stacked mica substrates. (h) Bright field optical images of $\beta\text{-In}_2\text{S}_3$ flakes. Adapted with permission [24]. Copyright 2017, Wiley.

or 3D nanostructure. For instance, Zr^{4+} ions doping into $\beta\text{-In}_2\text{S}_3$ 2D ultrathin nanoflakes was achieved via one-pot solvothermal method using $\text{In}(\text{NO}_3)_3$, thioacetamide and ZrCl_4 in the presence of octanol and octylamine at 220°C [118]. Similarly, our groups also synthesized $\text{Yb}^{3+}/\text{Tm}^{3+}$ co-doped tetragonal $\beta\text{-In}_2\text{S}_3$ flower-

like nanostructures [28]. V-substituted In_2S_3 nanocrystalline with the size of 20 nm was further prepared via solvothermal route using InCl_3 , VCl_3 , and Na_2S as reagents [119]. Notably, Lei et al fabricated atomically thin 2D Co-doped In_2S_3 sheets via scalable lamellar inorganic-organic hybrid intermediate strategy, as shown in Fig. 5b

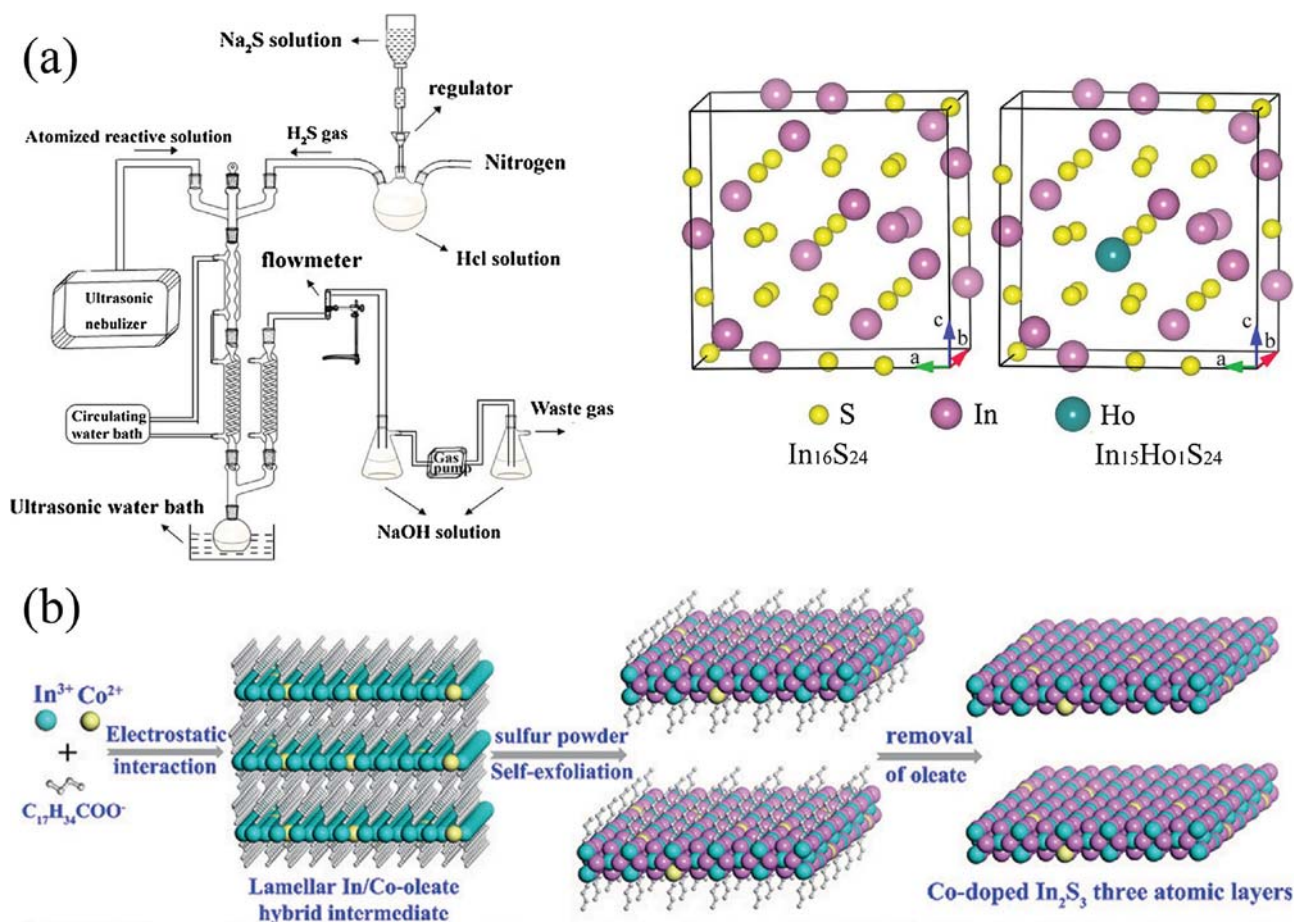


Fig. 5. (a) Right: synthetic facility of gas–liquid phase chemical method. Left: two calculation models for pure In_2S_3 ($\text{In}_{16}\text{S}_{24}$) and Ho^{3+} doped In_2S_3 ($\text{In}_{15}\text{Ho}_1\text{S}_{24}$). Adapted with permission [115]. Copyright 2017, Royal Society of Chemistry. (b) The formation diagram of Co-doped In_2S_3 three atomic layers. Adapted with permission [105]. Copyright 2015, Wiley.

[105]. Because of the electrostatic interaction between In^{3+} , Co^{2+} and oleate ions, a lamellar In/Co-oleate complex intermediate firstly formed in which the oleate ions arranged in a head-to-head bilayer order. After the addition of sulfur source through hydrothermal treatment, Co^{2+} doped In_2S_3 grew along the lamellar In/Co-oleate hybrid. As the reaction continuously proceeded, the self-exfoliation of the lamellar mesostructure was achieved and freestanding Co-doped In_2S_3 atomic layers came into being after the removal of surface oleate ions [105]. Hence, the facile improved hydrothermal method assisted by organic intermediate is a promising route to synthesize atomic-layer doped In_2S_3 materials.

Despite the prosperity of metal ions doped In_2S_3 photocatalysts, profound explorations on the preparation of non-metal (P, N, Cl etc.) doped In_2S_3 materials are promising. Besides, a thorough fundamental investigation of doped β - In_2S_3 materials based on advanced electron microscope platforms and theoretical simulation is urgently necessary towards the controlling of vacancies distribution, the analysis of corresponding doping sites in the crystal structure, as well as the influence of dopants on the morphology of In_2S_3 .

3.3. Heterostructured hybrids

Heterostructured composites have attracted great interest in making up for respective shortcomings in the area of materials science [13,120–122]. Vis-light responsive In_2S_3 with a relatively narrow band gap can act as a sensitizer or active constituent for coupling with another charge acceptor (and/or

carrier) [123]. In recent years, various In_2S_3 -based heterostructured hybrids have been synthesized, which can be classified into In_2S_3 /metal sulfides composites, In_2S_3 /carbonaceous composites, noble metal/ In_2S_3 composites, metal-oxide/ In_2S_3 composites, and In_2S_3 /metal-organic frameworks composites. Also, these synthetic routes can be summarized into precipitation, solvo/hydrothermal method, sonochemical method, electrodeposition technique and chemical welding [124–131].

With favorable redox reaction sites, electrical conductivity, good thermal stability, and earth abundance, metal sulfides (Bi_2S_3 , ZnS , Cu_2S , MoS_2 , MnS , CdS , Cu_3BiS_3 , AgInS_2 , CuInS_2 , ZnIn_2S_4 , etc) have been demonstrated to couple with In_2S_3 for superior performance and specific properties [132,133]. For instance, hierarchical Bi_2S_3 nanoflower/ In_2S_3 nanosheet composite were hydrothermally synthesized by virtue of differently seeded growth rates of two sulphides (solubility $K_{\text{sp}}(\text{Bi}_2\text{S}_3) = 1.0 \times 10^{-97}$ and $K_{\text{sp}}(\text{In}_2\text{S}_3) = 5.7 \times 10^{-73}$) [134]. The formation diagram was exhibited in Fig. 6a. In the reaction system, preferentially deposited Bi_2S_3 formed the sea-urchin-shaped crystal seeds with the adsorbed positively In^{3+} on the surface. With the reduction of surface activation energy, the In^{3+} was desorbed and the Bi^{3+} was depleted gradually. Accordingly, many vigorous energy sites in Bi_2S_3 nanoflowers initialized the nucleation process of In_2S_3 and facilitated the formation of uniformly ultrathin nanosheets [134]. This one-step synthetic process was of better repeatability to prepare uniform coating surface because of the compatibility between Bi_2S_3 nanoflower and In_2S_3 nanosheet. Similarly, $\text{ZnS}@ \text{In}_2\text{S}_3$ core@shell hollow nanospheres were fabricated via a facile refluxing method

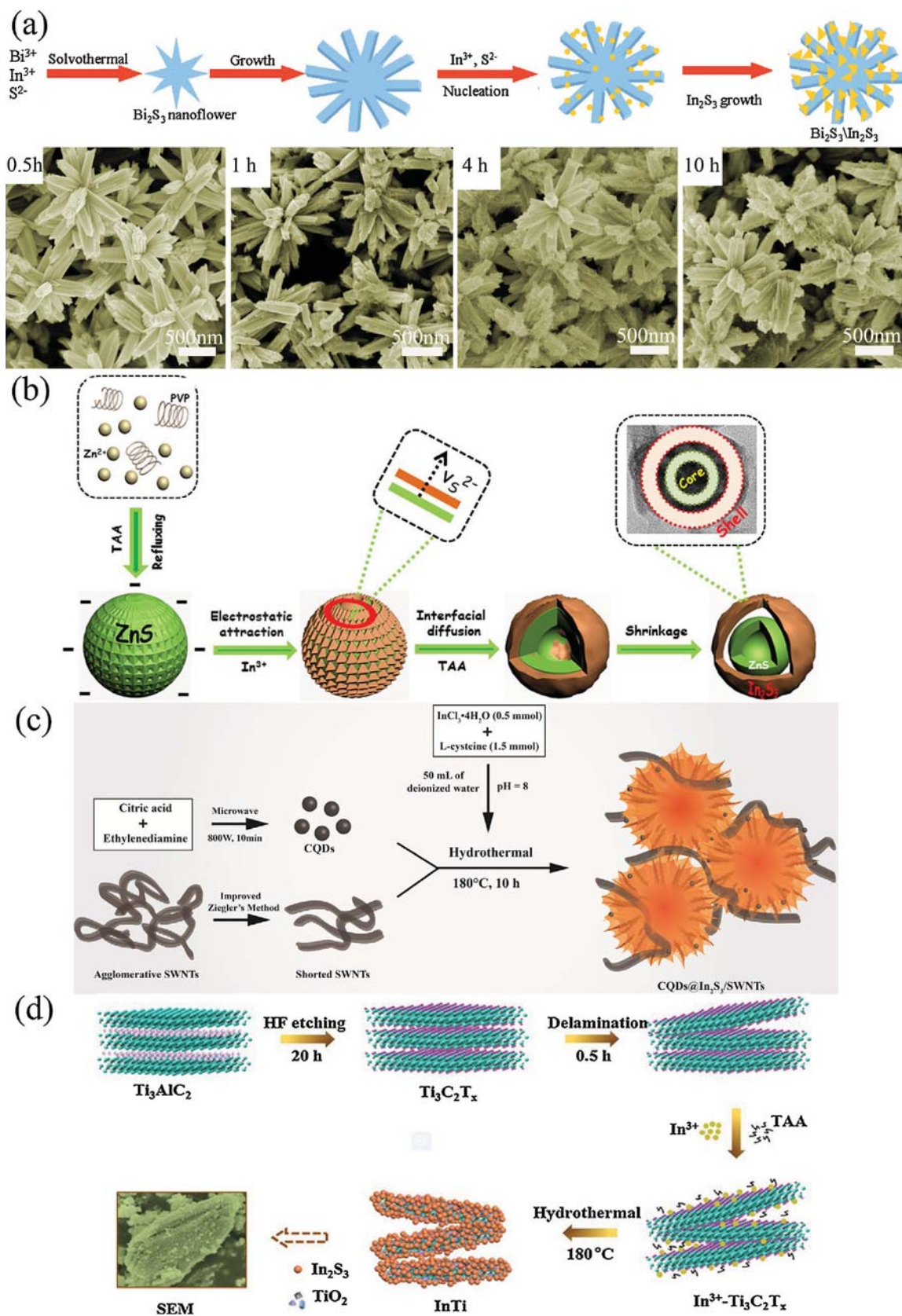


Fig. 6. (a) Top: formation scheme of $\text{Bi}_2\text{S}_3/\text{In}_2\text{S}_3$ composite; Bottom: SEM images of the products obtained at different reaction times. Reproduced with permission [134]. Copyright 2015, Royal Society of Chemistry. (b) Formation scheme of the $\text{ZnS}@\text{In}_2\text{S}_3$ core@shell hollow spheres. Adapted with permission [135]. Copyright 2017, Nature. (c) Formation scheme of $\text{CQDs}@\text{In}_2\text{S}_3/\text{SWNTs}$ composite. Adapted with permission [32]. Copyright 2016, Elsevier. (d) Formation scheme of $\text{In}_2\text{S}_3/\text{Ti}_3\text{C}_2\text{T}_x$ hybrids. Adapted with permission [26]. Copyright 2018, Elsevier.

based on ion-exchange Ostwald ripening (Fig. 6b) [135]. In order to prevent the agglomeration of ZnS nanospheres, the surfactant polyvinylpyrrolidone (PVP) was added to provide the intense repulsive forces among the polyvinyl groups [135]. Under the strong interaction between pyrrolidone ring of PVP and Zn^{2+} , the initiate ZnS tiny nanocrystals tended to self-assemble into solid spheres for minimizing the surface energy after the addition of CH_3CSNH_2 (TAA) [135]. Subsequently, the In^{3+} ions were added and attached on the negative surface of ZnS spheres by virtue of the electrostatic attraction. Through the interfacial diffusion of S^{2-} , In_2S_3 nanoparticles grew on the surface of ZnS crystals and then core@shell $\text{ZnS@In}_2\text{S}_3$ structure developed with another addition of TAA [135]. Similarly, the different solubility of ZnS and In_2S_3 was also served as the main driving force for the formation of core@shell structure [135]. Apart from the seeded growth routes, the catalyst-assisted growth principle was applied to synthesize $\text{Cu}_2\text{S/In}_2\text{S}_3$ heterostructured nanocrystals with various shapes under the high-temperature precursor-injection condition [125]. The intrinsic cationic deficiency of $\text{Cu}_{1.94}\text{S}$ nanocrystals catalyzed the growth of In_2S_3 nanocrystals after the injection of $\text{In}(\text{CH}_3\text{COO})_3$ -obtained dodecanethiol in the hot reaction system. Under different controlled parameters, the matchstick-like $\text{Cu}_2\text{S/In}_2\text{S}_3$ heterostructured nanorods and teardrop-like quasi-core/shell $\text{Cu}_2\text{S@In}_2\text{S}_3$ nanocrystals formed [125].

Carbonaceous nanomaterials are promising supports and charge carriers due to chemical inertness, stability, tunable structure and electrical properties [10,136]. In_2S_3 integrated carbonaceous nanomaterials, such as carbon quantum dots, carbon nanotubes, carbon nanofibers, graphene, graphene oxide, have been proven to be effective approaches for enhancing the photoelectrochemical properties of In_2S_3 -based photocatalysts [32,126,137–139]. The carbon quantum dots@3D daisy-like In_2S_3 /single-wall carbon nanotubes composite was fabricated via a one-pot hydrothermal approach [32]. As shown in Fig. 6c, a certain amount of carbon quantum dots (CQDs) and shorted single-wall carbon nanotubes (SWNTs) were simultaneously added in the synthetic process of In_2S_3 [32]. Carboxyl group was served as the nucleation sites for CQDs and In_2S_3 nanoflowers on SWNTs. In heterostructured CQDs@ In_2S_3 /SWNTs system, the CQDs efficiently linked three parts of the composite materials and became the bridge for transferring electron between In_2S_3 and SWNTs [32]. Post-modification assisted hydrothermal process is the main strategy for the preparation of In_2S_3 /graphene composite [123,140,141]. Typically, positively charged In^{3+} ions (or (3-aminopropyl) trimethoxysilane- In_2S_3) were immobilized onto the negative surface of graphene oxide (GO). Then, In_2S_3 particles formed during the self-assembly process and the graphene oxide was reduced into graphene via reducing agent like cysteine, hydrothermal or calcination reduction [138]. A similar method has been applied to synthesize the In_2S_3 /g- C_3N_4 heterostructure [142,143]. The cubic In_2S_3 nanoparticles with a diameter of about 10–20 nm were uniformly dispersed on the g- C_3N_4 nanosheets surface [32].

Other promising materials including noble metal, metal oxide and metal-organic frameworks have also been coupled with In_2S_3 to form binary or ternary heterostructures [128,131,144–146]. Li et al prepared $\text{In}_2\text{S}_3/\text{TiO}_2$ composites by employing three different electrodeposition processes (cyclic voltammetry electrodeposition, potentiostatic electrodeposition and pulse electrodeposition) [128]. Under the electric field conditions, S^{2-} ions were originated from the reaction between the electrons and the $\text{S}_2\text{O}_3^{2-}$ ions in the electrolyte. During the rapidly diffused process along the inner surface of the TiO_2 nanotube channels, the S^{2-} would react with In^{3+} , resulting in the nucleation and growth of In_2S_3 nanoparticles. Compared with the composites prepared by cyclic voltammetry electrodeposition and potentiostatic electrodeposition, the $\text{In}_2\text{S}_3/\text{TiO}_2$ composites prepared by the pulse technique

showed the optimal dispersion of ultra-fine In_2S_3 nanoparticles on the TiO_2 nanotube array [128]. To make full use of porous characters of metal-organic frameworks (MOFs), our groups firstly reported a core-shell $\text{In}_2\text{S}_3@\text{MIL-125}(\text{Ti})$ photocatalyst prepared by microemulsion-assisted solvothermal method [146]. Non-polar CS_2 dissolved in polar ethanol mixture (In^{3+} , NO_3^{2-} with H_2O) and then formed the oil/water emulsion. The hydrophobic group (C_2H_5) of polar molecules enveloped non-polar solvent droplets and the In^{3+} was bonded with the hydrophilic group (OH). Such micelles were absorbed on the hydrophilic surface of MIL-125(Ti). Under solvothermal conditions, the In^{3+} was surrounded by the soluble $\text{C}_2\text{H}_5\text{NS}$ in polar phases to initiate the growth and crystallization of In_2S_3 along the micelle interface to form the In_2S_3 “shell” on the external of MIL-125(Ti) [146]. Very recently, novel quasi-core-shell $\text{In}_2\text{S}_3/\text{anatase TiO}_2@\text{metallic Ti}_3\text{C}_2\text{T}_x$ MXene heterostructures were also fabricated via a simple hydrothermal process, as shown in Fig. 6d [26]. The $\text{Ti}_3\text{C}_2\text{T}_x$ nanosheets with abundant groups (e.g. -F, -OH and -O) had a hydrophilic surface and negative charge. When the In^{3+} ion was added into the reaction solution, multi-layer hydrophilic $\text{Ti}_3\text{C}_2\text{T}_x$ nanosheets could adsorb In^{3+} ions. Then, the adsorbed In^{3+} reacted with S^{2-} ionized from thioacetamide, thus leading to the growth of a large amount of irregular In_2S_3 nanoparticles on the surface of $\text{Ti}_3\text{C}_2\text{T}_x$ nanosheets [26]. Meanwhile, TiO_2 nanoparticles also formed as secondary product owing to the defects of $\text{Ti}_3\text{C}_2\text{T}_x$, leading to the formation of final core-shell $\text{In}_2\text{S}_3/\text{TiO}_2@\text{Ti}_3\text{C}_2\text{T}_x$ MXene heterostructures.

Despite the significant advances in the preparation of abundant In_2S_3 -based hybrids were made, coupling In_2S_3 with latest materials, such as MXene, black phosphorus, boronene, phosphine, may achieve a huge leap forward against the existing photoconversion. Moreover, the deep understanding of the growth mechanism also needs to be advanced.

4. Applications

4.1. Photochemically environmental decontamination

Different from traditional catalysis via reducing the energy barrier for promoting redox reaction, photocatalytic technology can directly utilize photon energies to overcome the energy barrier for the formation of electron excitation phase [2,147,148]. Take the environmental remediation into consideration, photochemical pollutant elimination is involved in the indirect reaction, direct interaction, or both. On the one hand, the excited electrons usually move to the surface of photocatalyst and react with oxygen (O_2) for the generation of superoxide radical anions ($^{\bullet}\text{O}_2^-$) [131]. Simultaneously, the corresponding holes travel to the exterior and oxidize surface adsorbed water molecules (H_2O) or hydroxyl groups (-OH) to produce hydroxyl radicals ($^{\bullet}\text{OH}$) [149]. These reactive radical species can decompose and mineralize pollutants into carbon dioxide, water and other inorganic ions finally [150]. On the other hand, the photogenerated holes (or electron) directly oxidize (or reduce) pollutants remaining adsorbed on the photocatalyst surface via the nucleophilic reaction or electrophilic reaction [151,152]. However, solar-light utilization efficiency, cost-performance ratio, secondary toxicity, etc. are the major concerns for such photocatalysts. It has been extensively demonstrated that the In_2S_3 with excellent stability and low-toxic feature can be served as a promising full-solar-spectrum (UV-vis-NIR) photocatalyst and a sensitizer for another semiconductor photocatalyst due to the presence of defect band [33,153]. In order to improve the efficiency of pollutant removal, the separation and transport of photoinduced charge carriers for In_2S_3 -based materials is the most crucial influences for more accessibly reductive electron and oxidizing holes. Therefore, many efforts have been devoted to lowering the recom-

bination of photogenerated electron-hole pairs by morphology design, doping or constructing heterostructure. In the applications of In_2S_3 -based photocatalysts in water and gas pollution, most of the pollutants are focused on organic dyes, heavy metals, pharmaceuticals and personal care products, fluorine-containing phenolic derivatives, gaseous ortho-dichlorobenzene and microorganisms [128,134,135,152,154–160].

Controlling specific morphology with favorable microstructure (e.g. porosity) is feasible to adjust the mass-transfer pathway towards photocatalytic removal performance of pollutants in the liquid-phase system. For instance, tetragonal In_2S_3 nanoparticles with a particle size of 5–20 nm showed stable and excellent photocatalytic performance for methyl orange (MO) removal over the entire solar light spectrum. The MO reduction efficiency could reach 96.2% within 30 min under UV light, 95.4% within 3 h under Vis light and 67.2% within 3 h under NIR light, respectively [33]. This kind of 0D In_2S_3 nanoparticle structure exhibited very broad light absorption region (the absorption edges reached 650 nm) and two broad absorption peaks at 1440 nm and 1940 nm in the NIR region due to the presence of a defect band located above the VB of In_2S_3 . The photocurrent response reached up to 10.5 μA in the NIR light [33]. Besides, Wu et al. engineered 3D hierarchical porous microsphere-like (3HPM) In_2S_3 stacked by 2D ultrathin nanosheets, which exhibited 3 times higher photo-degradation efficiency of MO than that of 3D solid microsphere-like In_2S_3 [100]. This could be attributed to the relatively higher specific surface area and more exposed reaction sites, which in turn accelerated the surface separation of photoinduced electrons (or holes) and interfacial charge-carrier transfer [100]. Similar researches have also been reported by Qiu et al. and Wei et al. [66,161,162]. Although the microstructure adjustment has significant improvement in photo-degradation efficiency, the quantified relationship between morphology (or materials dimension) and photocatalytic performance is not clear.

Doping is also able to modulate the electronic properties and extend the absorption spectrum of In_2S_3 . Rare earth ions doping such as Dy^{3+} , Tb^{3+} , Eu^{3+} , Yb^{3+} and Tm^{3+} have also been devoted to increasing the light absorption of In_2S_3 , as they could convert low energy photons (NIR) into higher energy emitted photons (UV or Vis light) via nonlinear optical effect of up-conversion process [28,163–166]. Recently, our group designed the $\text{Yb}^{3+}/\text{Tm}^{3+}$ co-doped In_2S_3 crystal structure, which remarkably increased the photo-activity of In_2S_3 towards chromium(VI) reduction and RhB oxidation [28]. The reduction efficiency of Cr (VI) reached 97.9% under NIR light irradiation for 100 min, 99.3% under Vis light for 10 min and 98.3% under UV light for 10 min. As well, the $\text{Yb}^{3+}/\text{Tm}^{3+}$ co-doped In_2S_3 retained stable efficiency for the RhB degradation of 98.4% (NIR, 100 min), 97.3% (Vis, 14 min), and 96.3% (UV, 14 min) [28]. As shown in Fig. 7a, through the up-conversion process of $\text{Yb}^{3+}/\text{Tm}^{3+}$, the adsorbed NIR light photons were converted into higher energy emitted photons, which excited the In_2S_3 to generate electron-hole pairs [28]. In detail, the Yb^{3+} ions were firstly excited by the pump photons of 980 nm under NIR light. Through three successive energy transfer from Yb^{3+} to Tm^{3+} , the higher energy levels $^3\text{H}_5$, $^3\text{F}_2$ and $^1\text{G}_4$ of Tm^{3+} were populated [28]. While the $^1\text{D}_2$ energy level of Tm^{3+} was populated via the cross-relaxation process between Tm^{3+} ions. During the decays of high state level, a certain amount of photons at high energy levels were emitted to the low energy levels [28]. Further, the fluorescence emission energy was absorbed by the photocatalyst to produce electrons and holes. Notably, the excited electrons could be captured by the intermediate energy states and vacancies, accelerating the separation of photogenerated charges [28]. Intermediate band semiconductors have raised interest as materials to promote photocatalytic activity. Conesa et al. demonstrated that V-substituted In_2S_3 as an intermediate band (IB) material could enhance the photo-conversion

efficiency by combining two photons to obtain a higher energy electron excitation [119,167]. The partial substitution of In by V in the In_2S_3 could yield in-gap levels within the crystalline structure, further causing the shift of Fermi energy level, and both valence and conduction bands positions [119,167]. The photo-degradation of HCOOH under different wavelengths light (Fig. 7b) demonstrated that the V-substituted In_2S_3 was able to photodegrade HCOOH in the wavelengths light between 700 and 750 nm, confirming its ability to use photons with energy clearly below the band gap of pure In_2S_3 [119]. Also, it was proved that the photo-degradation rates of V-substituted In_2S_3 were comparable to the pure In_2S_3 [119]. Yang et al. examined the photocatalytic performance of Ca^{2+} doped In_2S_3 towards RhB degradation under visible light. The introduction of Ca^{2+} not only induced the spherical hierarchical structures of In_2S_3 but also promoted the formation of the indirect band gap, thus accelerating the RhB degradation rates 3 folds as fast as TiO_2 (P25) under the same condition [75].

Additionally, In_2S_3 -based heterostructured photocatalyst via coupling with another charge acceptor (and/or carrier) is also endowed with good photo-degradation activity. Recently, a novel quasi-core-shell $\text{In}_2\text{S}_3/\text{TiO}_2@\text{Ti}_3\text{C}_2\text{T}_x$ ternary heterostructure was proposed by our research group. The MO removal efficiency of $\text{In}_2\text{S}_3/\text{TiO}_2@\text{Ti}_3\text{C}_2\text{T}_x$ hybrids reached above 90% under Vis light exposure within 60 min, which was about 6.2 and 3.2 times higher than that of pure $\text{Ti}_3\text{C}_2\text{T}_x$ and In_2S_3 . According to the pseudo-first-order model $\ln(C/C_0) = -kt$, the photocatalytic degradation rate parameter (k) (y -axis in Fig. 7c) was used for evaluating the performance of five In_2S_3 -based photocatalysts [26]. Compared with other types of In_2S_3 -based photocatalysts including $\text{In}_2\text{S}_3/\text{MoS}_2$, $\text{In}_2\text{S}_3/\text{TiO}_2$, $\text{In}_2\text{S}_3/\text{reduced graphene oxide (rGO)}$ and $\text{In}_2\text{S}_3/\text{carbon nanotube (CNT)}$, the $\text{In}_2\text{S}_3/\text{TiO}_2@\text{Ti}_3\text{C}_2\text{T}_x$ hybrids showed the highest photocatalytic degradation rate of 0.04977 min^{-1} for MO (Fig. 7c) [26]. The constructed double heterojunction structure composed of type-II heterojunction and Schottky junction provided plentiful charge transfer channels, thus accelerating the separation and transfer of photogenerated charge carriers [26]. Yan et al. constructed a Z-scheme $\text{Ag}_3\text{PO}_4/\text{In}_2\text{S}_3$ photocatalyst via loading ultra-low Ag_3PO_4 (0.086 wt %) on hierarchical In_2S_3 microspheres. The hierarchical $\text{In}_2\text{S}_3/\text{Ag}_3\text{PO}_4$ composites degraded almost all dyes (MO, MB and RhB) under Vis light within 7 min [131]. As shown in Fig. 7d, Ag nanoparticles produced in the synthetic process acted as a charge transmission mediator to neutralize photogenerated holes from the VB of In_2S_3 and electrons from the CB of Ag_3PO_4 , thus restraining the photocorrosion of In_2S_3 and keeping the strong reducibility of electrons [131]. As for the photocatalytic removal of pharmaceuticals and personal care products pollution, a multi-dimensional ternary carbon quantum dots (CQD)@3D daisy-like $\text{In}_2\text{S}_3/\text{single-wall carbon nanotubes (SWNTs)}$ heterostructure was reported to exhibit superior activity (Fig. 7e) for the photo-degradation of ciprofloxacin (CIP), tetracycline (TC) and levofloxacin tablets (LEV) [32]. With the addition of SWNTs and CQDs in sequence, the photodegradation rates of all the antibiotic increased gradually under Vis light irradiation for 60 min [32]. The remarkable increment in photo-degradation efficiency was ascribed to the addition of charge transfer bridge (CQDs), increased specific surface area and improved light absorbance [32]. Recently, the $\text{In}_2\text{O}_3/\text{In}_2\text{S}_3/\text{CdS}$ ternary porous heterostructure films were reported to exhibit exceptional Vis-light photoelectrocatalytic (PEC) activity towards the degradation of 4-Fluoro-3-methylphenol [155]. The PEC degradation efficiency reached 87.3% with the fastest degradation rate of 0.279 h^{-1} . Correspondingly, the $\text{In}_2\text{O}_3/\text{In}_2\text{S}_3/\text{CdS}$ photoelectrode had the strongest photocurrent response compared with pure In_2O_3 and $\text{In}_2\text{O}_3/\text{In}_2\text{S}_3$ films (Fig. 7f) [155]. The favorable performance was considered to the rapid separation of charge carriers

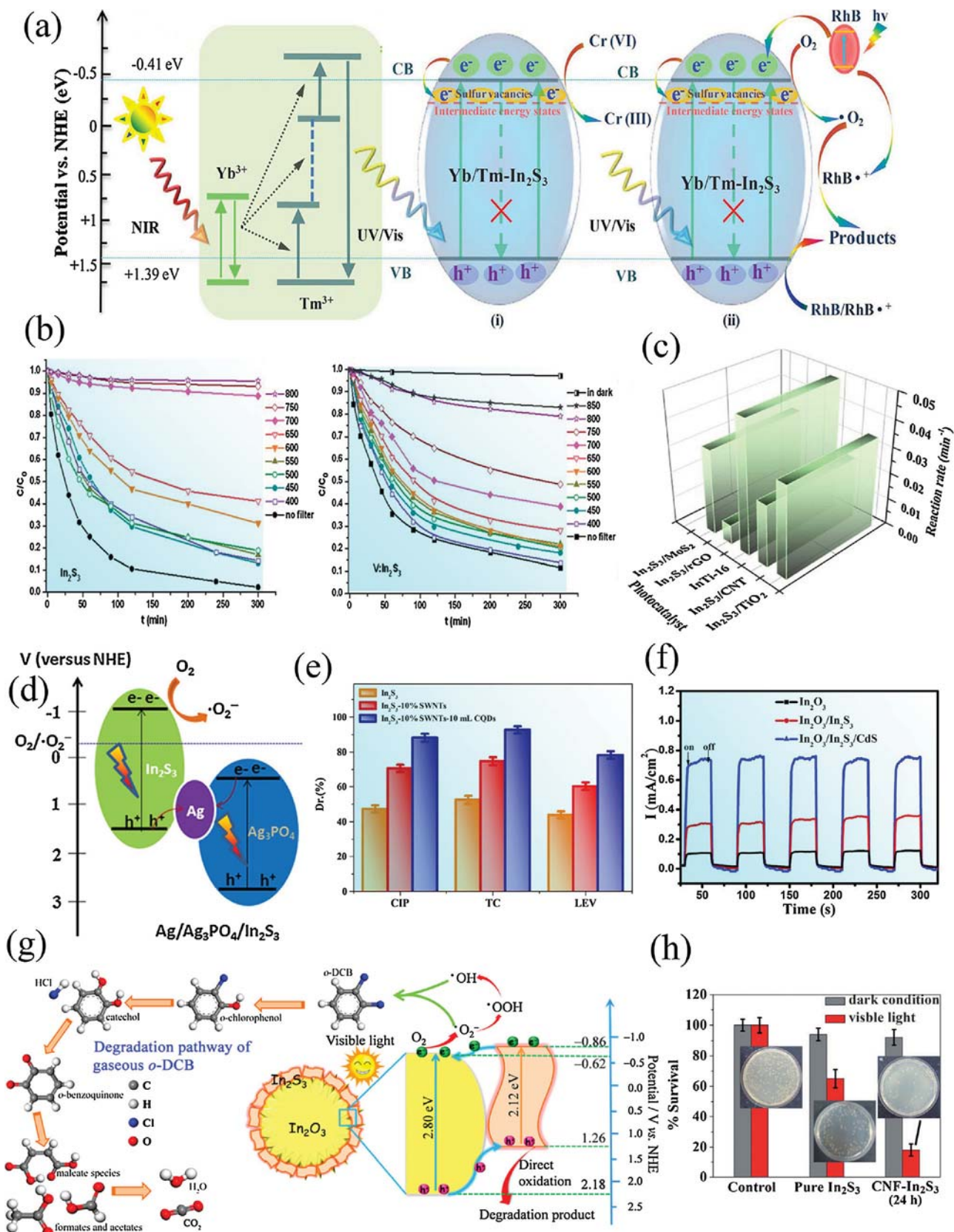


Fig. 7. (a) Photocatalytic process of $\text{Yb}^{3+}/\text{Tm}^{3+}$ co-doped In_2S_3 for Cr(VI) and RhB degradation. Adapted with permission [28]. Copyright 2017, Elsevier. (b) Photocatalytic degradation of HCOOH under different wavelengths light for In_2S_3 and V doped In_2S_3 . Adapted with permission [119]. Copyright 2014, Royal Society of Chemistry. (c) Photocatalytic degradation of MO for different In_2S_3 -based hybrids. Adapted with permission [26]. Copyright 2018, Elsevier. (d) Schematic of electron-hole pairs separation mechanism for Z-scheme $\text{In}_2\text{S}_3/\text{Ag}_3\text{PO}_4$ composites. (e) Photodegradation rates of CIP, TC and LEV with In_2S_3 , In_2S_3 /SWNTs and In_2S_3 /SWNTs/CQD for 60 min under Vis light. Adapted with permission [131,32]. Copyright 2016, Elsevier. (f) The chronoamperometry of In_2O_3 , $\text{In}_2\text{O}_3/\text{In}_2\text{S}_3$ and $\text{In}_2\text{O}_3/\text{In}_2\text{S}_3/\text{CdS}$. Adapted with permission [155]. Copyright 2017, Elsevier. (g) Left: schematic degradation pathway of gaseous o -DCB, Right: schematic of the electron-hole separation mechanism for the 3D $\text{In}_2\text{S}_3/\text{In}_2\text{O}_3$ heterostructures under Vis light. Adapted with permission [152]. Copyright 2016, American Chemical Society. (h) E. coli inactivation performance under various reaction conditions (inset: corresponding photographs of agar plates). Adapted with permission [172]. Copyright 2014, Wiley.

generated from the double type-II modes, and the enhanced super-hydrophilicity and Vis light utilization [155].

Gaseous ortho-dichlorobenzene (o-DCB), a kind of chlorinated volatile organic compound generated from the incineration of medical and municipal wastes, could be efficiently photodegraded as well [152]. A 3D $\text{In}_2\text{S}_3/\text{In}_2\text{O}_3$ heterostructure was constructed with the In_2O_3 microflowers and the adherent In_2S_3 nanoflakes. The $\text{In}_2\text{S}_3/\text{In}_2\text{O}_3$ heterostructure exhibited 16.4 times higher photodegradation rate of gaseous o-DCB than that of TiO_2 (P25) under Vis light exposure [152]. The schematic degradation pathway was shown in Fig. 7g, through the type II heterojunction system, the photogenerated electron-hole pairs effectively separated and transferred to the surface of $\text{In}_2\text{S}_3/\text{In}_2\text{O}_3$. Then, the absorbed o-DCB was oxidized by radical species ($\cdot\text{O}_2^-$, $\cdot\text{OH}$, and photogenerated h^+) to form phenolate species, formates, acetates, and maleates. Ultimately, these reaction products were transferred into H_2O and CO_2 [152].

Pathogenic microbes have caused millions of mortalities via the media of water or air according to the literature and World Health Organization [168–170]. Distinguished from the traditional disinfection method (UV, ozonation or chlorination disinfection), photocatalytic disinfection is more environmentally friendly for its nontoxicity and cost-effective [171]. Gao et al. firstly investigated the photocatalytic inactivation of *Escherichia coli* by coupling carbon nanofiber (CNF) and In_2S_3 nanoflowers to build hierarchical CNF- In_2S_3 nanostructures, which possessed large specific surface area ($162.91 \text{ m}^2 \text{ g}^{-1}$) and improved light absorption [172]. As shown in Fig. 7h, nearly 80% *Escherichia coli* (*E. coli*) cells could be killed by CNF- In_2S_3 under Vis light irradiation due to the occurrence of oxidative stress, which was 2 times higher than that of the In_2S_3 (40%) [172]. Because of the effective separation of photogenerated electrons and holes on the heterostructure surface, *E. coli* cells were finally inactivated by the oxidation of generated superoxide anion radicals and holes conjointly [172].

Based on the achievement of In_2S_3 -based photocatalysts in the field of environmental remediation, we deem that there is still a long way to go for its industrialization due to the complex constituents in an actual environment. Novel In_2S_3 -based photocatalysts with universal photo-activity towards various organic contaminant under Vis or NIR light are still in demand. Besides, there still remains a big gap between the In_2S_3 -based photocatalytic technology and the volatile organic compounds pollution. The elimination of emerging volatile organic compounds over In_2S_3 -based photocatalysts is still in its infancy and the degradation pathways of contaminant need to be deeply explored for better comprehension with regard to the photocatalytic reaction.

4.2. Artificially photosynthetic renewable fuels

4.2.1. Hydrogen energy via water splitting

4.2.1.1. Solid powder reaction system. Hydrogen gas (H_2) with the highest energy density (140 MJ kg^{-1}) on a gravimetric basis becomes an alternative fuel in contrast to the hydrocarbon fuels (i.e. petrol and diesel) with the energy density range from 40 to 50 MJ kg^{-1} [11]. Artificially photosynthetic hydrogen energy, a promising energy source without depending on fossil reserves, owns three main processes including (i) absorption of photons to form electron-hole pairs, (ii) separation and migration of photogenerated carriers to the photocatalyst surface (or interface) and (iii) surface chemical reactions on the active sites and surface area [173,174]. Over the past few years, a large number of In_2S_3 -based nanomaterials with enhanced activity for the photocatalytic H_2 generation have been developed. As shown in Fig. 2f, the bottom level of CB (-0.8 V vs. NHE) in pure In_2S_3 is more negative than the redox potential of H^+/H_2 (0 V vs. NHE) [34]. The VB (1.5 V vs. NHE) is slightly positive than the redox potential of $\text{O}_2/\text{H}_2\text{O}$ (1.23 V vs NHE)

[34,97]. It provides the thermodynamically sufficient potentials for H_2 generation via water splitting. The inherent defective nature and easily regulatory micro/nanostructures endow In_2S_3 with an excellent platform, which facilitates the separation and migration of available photoinduced carriers and the decoration of cocatalyst in surface chemical reactions.

In the experimentally pioneering work of Naik and co-workers, the authors prepared tetragonal and cubic $\beta\text{-In}_2\text{S}_3$ dandelion flowers by rapid microwave solvothermal process. The tetragonal and cubic $\beta\text{-In}_2\text{S}_3$ were applied to photocatalytic H_2 evolution from H_2S photo-decomposition under Vis-light irradiation [93]. The maximum hydrogen production rate was $1856 \mu\text{mol h}^{-1}$ [93]. Fu et al. further demonstrated that the cubic $\beta\text{-In}_2\text{S}_3$ exhibited steadily photocatalytic activity for H_2 production via water splitting with the maximum hydrogen generation rate of $736 \mu\text{mol g}^{-1} \text{ h}^{-1}$ at the Pt loading amount of ca.2.0 wt% while the tetragonal $\beta\text{-In}_2\text{S}_3$ showed no activity, which was related to the vacancy ordered/disordered degree of In_2S_3 [43]. They proposed that sulfur-bridged indium ions were important for the transfer of photogenerated charges. The presence of ordered indium vacancies blocked the transportation efficiency of the carrier transfer pathway. In parallel, partial indium vacancies ordered $\beta\text{-In}_2\text{S}_3$ was considered as the intermediate phase between tetragonal and cubic $\beta\text{-In}_2\text{S}_3$, which was reported to show photo-activity for H_2 evolution with a generation rate of $442 \mu\text{mol g}^{-1} \text{ h}^{-1}$ and the apparent quantum yields of 1.45% at 400 nm [175]. To enhance photogenerated carrier separation of In_2S_3 , various semiconductors (i.e. TiO_2 , In_2O_3 , $\text{Na}_2\text{Ti}_3\text{O}_7$) have been integrated in the presence of Pt cocatalyst [176–178]. Chai et al. observed that the $\text{In}_2\text{S}_3/(1.0 \text{ wt\% Pt-TiO}_2)$ nanocomposite with a mass ratio of 3 : 2 had the maximum photocatalytic hydrogen production rate of 135 mol h^{-1} , much more superior than that of pure In_2S_3 and pure TiO_2 [179]. The charge separation process was particularly probed by Wang et al. through photoelectrochemical transient photo-current measurements and optical pump-terahertz probe spectroscopic [176]. It was verified that the photocurrent of the $\text{In}_2\text{S}_3/\text{Pt-TiO}_2$ was stronger than that of the neat In_2S_3 electrode, implying the more efficient separation of photo-induced charge carriers in the nanocomposite. The type-II migration of photoinduced electrons from the In_2S_3 CB to the TiO_2 CB and subsequently into the external Pt nanoparticles occurred on a $\sim 5 \text{ ps}$ timescale (Fig. 8a) [176]. Besides, the loading amount and nature of cocatalyst also affected the photocatalytic H_2 generation. With the same loading amount, the hydrogen production rate of noble-metal-loaded $\beta\text{-In}_2\text{S}_3$ followed this order $\text{Pd} > \text{Pt} > \text{Ru} > \text{Au}/\beta\text{-In}_2\text{S}_3$ [43]. Noble metals with the low activation potentials and work functions are not only served as the active sites for promoting H_2 evolution, but also promoting the separation of photoexcited electrons and holes.

In order to substitute high-cost noble metals, achieve outstanding quantum yields and reduce photocorrosion simultaneously, building In_2S_3 -based binary or ternary heterostructured materials can be an efficient strategy. These composited photocatalysts include $\text{In}_2\text{S}_3\text{-MoS}_2$, $\text{In}_2\text{S}_3\text{-MnS}$, $\text{In}_2\text{S}_3\text{-ZnS-Ag}_2\text{S}$, $\text{In}_2\text{S}_3\text{-ZnS-CuS}$, $\text{In}_2\text{S}_3\text{-MoS}_2\text{-CdS}$, and $\text{In}_2\text{S}_3\text{-WO}_3\text{-graphene}$ [35,97,180–183]. For instance, 2D layered $\text{MnS}/\text{In}_2\text{S}_3$ heterostructure exhibited highly enhanced Vis-light photocatalytic H_2 production from H_2S in the absence of noble metals cocatalyst [35]. The maximum H_2 production rate was about $8360 \mu\text{mol g}^{-1} \text{ h}^{-1}$, which was approximately 50 times higher than that of $\beta\text{-In}_2\text{S}_3$ alone [35]. The apparent quantum yield (AQE) reached 34.2% at 450 nm, the corresponding H_2 evolution amount was $36,440 \mu\text{mol h}^{-1}$. More importantly, the $\text{MnS}/\text{In}_2\text{S}_3$ composite displayed a good stability and anti-photocorrosion [35]. In the photocatalytic process of splitting H_2S (Fig. 8b), the $\text{MnS}/\text{In}_2\text{S}_3$ photocatalyst was excited to produce electron-hole pairs. Because of the matched energy band, the photogenerated charges separated with the holes left in the VB of

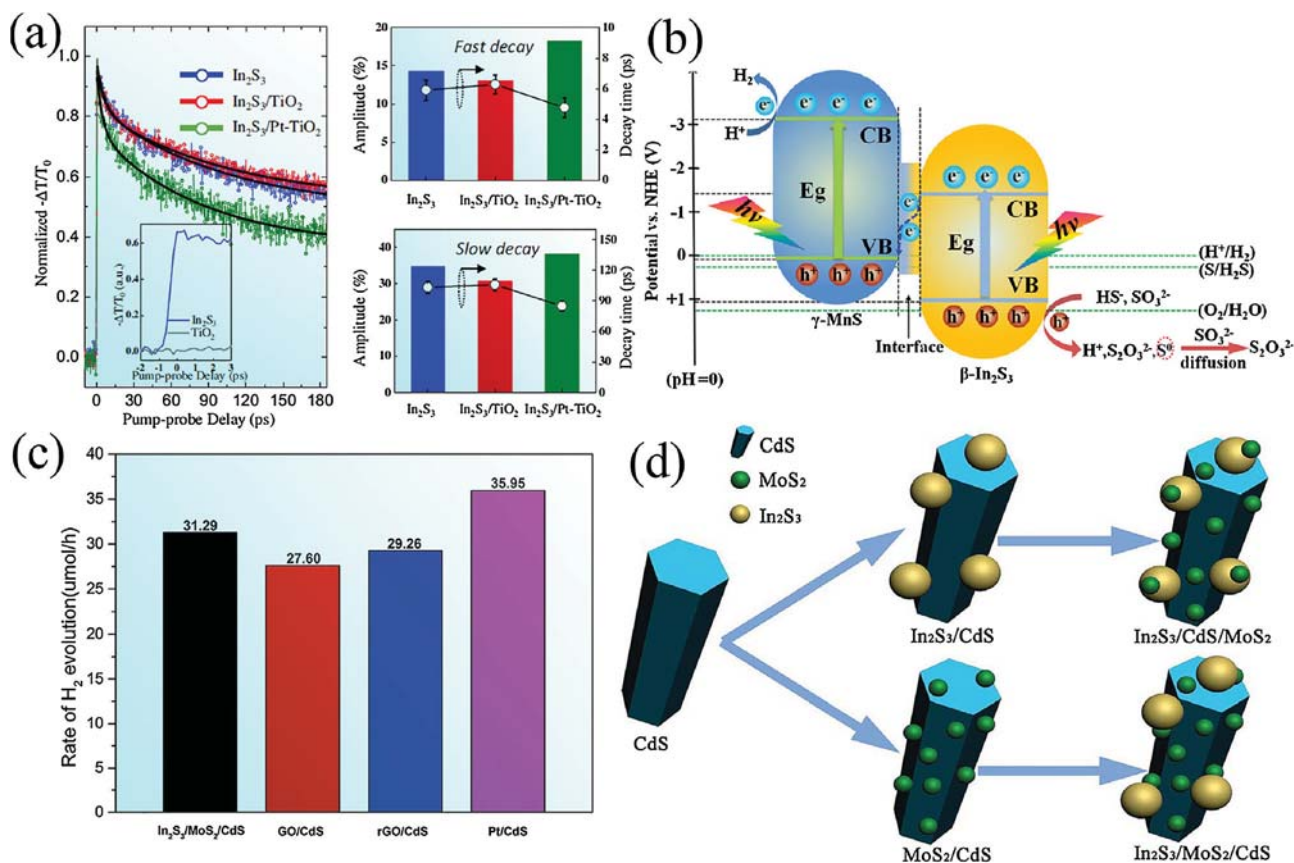


Fig. 8. (a) Right: normalized THz photoconductivity signals for In_2S_3 , $\text{In}_2\text{S}_3/\text{TiO}_2$, and $\text{In}_2\text{S}_3/\text{Pt-TiO}_2$ and the inset is the OPTP signals for In_2S_3 and TiO_2 . Left: the extracted amplitude (column) and decay times (circles) for the fast and slow decay components, respectively [176]. Adapted with permission. Copyright 2016, Elsevier. (b) Photocatalytic process of splitting H_2S in $0.6\text{ M Na}_2\text{SO}_3/0.1\text{ M Na}_2\text{S}/3\text{ M H}_2\text{S}$ solution for $\text{MnS}/\text{In}_2\text{S}_3$ composite. Adapted with permission [35]. Copyright 2017, Elsevier. (c) Photocatalytic rate of H_2 evolution on $\text{In}_2\text{S}_3/\text{MoS}_2/\text{CdS}$, GO/CdS , rGO/CdS and Pt/CdS under Vis light. (d) Schematic of $\text{In}_2\text{S}_3/\text{CdS}/\text{MoS}_2$ and $\text{In}_2\text{S}_3/\text{MoS}_2/\text{CdS}$ heterostructures. Adapted with permission [182]. Copyright 2015, Royal Society of Chemistry.

In_2S_3 and electrons left in the CB of MnS . The photogenerated holes were consumed by the additional sacrificial reagents Na_2SO_3 and Na_2S , thus improving the anti-photocorrosion ability of $\text{MnS}/\text{In}_2\text{S}_3$ photocatalysts. Moreover, both the solid S and the lightproof yellow disulfide ions (S_2^{2-}) originated from the photooxidation of holes were reduced by SO_3^{2-} ions into colorless thiosulfate ions ($\text{S}_2\text{O}_3^{2-}$), which ensured the long-term photocatalytic stability [35]. Fang et al. constructed a dual-defective and strongly-binding $\text{MoS}_2/\text{In}_2\text{S}_3$ photocatalyst, in which defective MoS_2 layers with abundant exposed edges in situ grown on the layered and defective In_2S_3 nanosheets [97]. With the 1 wt% MoS_2 layers loading in $\text{MoS}_2/\text{In}_2\text{S}_3$, a ca. 12-fold enhancement of the H_2 evolution rate using lactic acid as scavenger agent compared with bare In_2S_3 . The cocatalyst MoS_2 served as the active site for H_2 spillover, helped to harvest light and occupy the unstable positions of In_2S_3 . Long-term stability in photocatalysis was proposed that the existing disorder crystal structures broke the strict crystal anisotropy of In_2S_3 for the formation of homogenous bond situations in all orientations, which made the separated holes difficult in breaking the isotropic energy-balanced bonds. Further, Jiang et al. designed a hierarchical ternary $\text{In}_2\text{S}_3/\text{MoS}_2/\text{CdS}$ heterostructured photocatalyst (Fig. 8c), which was declared to display higher activity without noble metal photocatalyst for photocatalytic H_2 evolution than that of graphene oxide/CdS, graphene/CdS composites and co-catalyst Pt contained systems [182]. The important advantage is the structure sequence and deposition site (Fig. 8d), that is, MoS_2 deposited on the interface of CdS and In_2S_3 is more efficient in promoting charge transfer and inhibiting the recombination of photoinduced electrons and holes. Moreover, the well-matched band position between CdS and In_2S_3

prevented the accumulation of holes in CdS and inhibited corrosion of CdS. From the above analysis, rational and multifunctional heterostructure design is a developing trend for highly-efficient H_2 generation and anti-photocorrosion via combining the superiority of respective composition and the directional carrier transfer pathway [182]. It is promising to extend atomically thin In_2S_3 to the preparation of heterojunctions via coupling with different materials for efficient solar energy conversion. Significant work is still required towards manipulating the crystal structure of In_2S_3 for adjustable vacancies or filling the vacancies with a heteroatom (P, N, Cl, etc.) to tailor the intrinsic properties, and identifying the structure sequence and deposition site when building multiple In_2S_3 heterostructures.

4.2.1.2. Photoelectrochemical cell. Photoelectrochemical (PEC) water splitting via In_2S_3 -based semiconductor is the other promising approach to the scalable generation of renewable fuels. Coupled with solar energy conversion, PEC water splitting can achieve the rapid kinetic processes for both water reduction and oxidation with a minimal carbon footprint. In the PEC cell, three processes are included, carriers generation from the absorption of the photons of semiconductor firstly, the rapid separation and transfer of carriers due to the additional electric field, and the redox reaction for water splitting. Several characteristics are crucial for efficient water splitting in PEC cell systems, including low onset potential of photoanode, favorable photocurrent, and long-term stability.

The research on PEC properties of In_2S_3 films was firstly reported by Zhang et al, in which the wedge-like In_2S_3 films exhibited a photocurrent density of 0.48 mA cm^{-2} [184]. Subsequently, the relation

between In_2S_3 morphologic structures and PEC characteristics was investigated by Ehsan et al. [185]. Through controlling the precursor's nature (i.e. alkyl groups, metal-ligand designs, and deposition temperatures), different morphologies of $\beta\text{-In}_2\text{S}_3$ including lumps, pyramidal, flakes and granular crystallites were deposited on the substrate surface. Among them, the $\beta\text{-In}_2\text{S}_3$ thin films with pyramidal crystallites exhibited the highest photocurrent density of 1.25 mA cm^{-2} vs at Ag/AgCl of 0.23 V [185]. Tian et al. further investigated the PEC performance of 2D ultrathin $\beta\text{-In}_2\text{S}_3$ nanocrystals (nanobelts and nanoflakes) with a thickness of 2 nm [62]. Due to the more convenient pathway and active sites derived from the 2D ultrathin structure, the photocurrent density of $\beta\text{-In}_2\text{S}_3$ nanoflakes (0.37 mA cm^{-2}) and nanobelts (0.12 mA cm^{-2}) were both higher than that of the $\beta\text{-In}_2\text{S}_3$ nanoparticles (0.02 mA cm^{-2}). The 2D $\beta\text{-In}_2\text{S}_3$ nanocrystals showed excellent stability for PEC water splitting with a constant potential of 0.22 V vs. Ag/AgCl under irradiation for 160 min [62]. Su et al. demonstrated that n-type flower-like In_2S_3 porous films possessed higher anodic photocurrent of ca. 1.3 mA cm^{-2} at 0.2 V vs reversible hydrogen electrode (RHE), which was ascribed to the more efficient carrier passway from the ideal porous structure. The maximum incident photon-to-electron conversion efficiency of In_2S_3 porous films reached 2.57% at 420 nm and 0 V [186].

Metal ion doping into the host lattice structure also makes significant progress in the PEC efficiency of $\beta\text{-In}_2\text{S}_3$, through which the electron density, trap states, energy levels, and surface defects are tailored to retain charge balance for the doped system. Therefore, the unique photoelectric properties of doped $\beta\text{-In}_2\text{S}_3$ are induced for superior PEC water splitting. As an example, Zr^{4+} doped $\beta\text{-In}_2\text{S}_3$ 2D nanoflakes was reported to exhibit 10 folds higher photocurrent density (1.1 mA cm^{-2} at $1.3 V_{\text{RHE}}$) than pure $\beta\text{-In}_2\text{S}_3$ [118]. The onset potential of Zr^{4+} doped $\beta\text{-In}_2\text{S}_3$ was $1.05 V_{\text{RHE}}$, which was lower than that of pure $\beta\text{-In}_2\text{S}_3$ ($1.2 V_{\text{RHE}}$). After being illuminated at $1.2 V_{\text{RHE}}$ for 240 min, the Zr^{4+} doped $\beta\text{-In}_2\text{S}_3$ retained favorable stability for PEC water splitting. A redshift of 0.22 eV in the absorption spectrum and negative shift in energy levels were observed after the introduction of Zr^{4+} , thus leading to the improved PEC activity in the extended visible light edge from 450 to 490 nm [118]. Remarkably, atomic layer confined doping of Co ions into cubic In_2S_3 three atomic layers (3ALs) was achieved by Lei et al. [105]. As revealed by the density functional calculations, the Co ions doping resulted in the increased density of states at CB and several new energy levels from the splitting of Co 3d states. Hence, the d-d internal transition of Co ions in tetrahedral coordination was built for the electrons to be excited easily, making it possible for Co-doped In_2S_3 3ALs to achieve more outstanding photoconversion efficiency. As shown in Fig. 9a, the practical photocurrent of Co-doped In_2S_3 3ALs photoelectrode (1.17 mA cm^{-2} at $1.5 V_{\text{RHE}}$) was 10 and 17 times higher than that of the three atomic layers In_2S_3 and the bulk In_2S_3 respectively. The experimental incident photoconversion efficiency (IPCE) of Co-doped In_2S_3 3ALs photoelectrode reached up to 46% at 450 nm and two sharp increases in the Vis-NIR spectrum (750–900 and 1500–1750 nm) were observed (Fig. 9b). The recovery lifetime of Co-doped In_2S_3 3ALs (360 ps) was 25 folds longer than In_2S_3 3ALs, indicating the superior electron-hole separation efficiency. As a result, the experimental water splitting rates of Co-doped In_2S_3 3ALs reached the verge of its theoretical values [105].

To further enhance the PEC performance for water splitting, variety of binary or ternary In_2S_3 -based heterostructures have been constructed including $\text{In}_2\text{S}_3/\text{ZnO}$, $\text{In}_2\text{S}_3/\text{TiO}_2$, $\text{In}_2\text{S}_3/\text{MoS}_2$, $\text{In}_2\text{S}_3/\text{g-C}_3\text{N}_4$, $\text{In}_2\text{O}_{3-x}/\text{In}_2\text{S}_3$, $\text{TiO}_2/\text{In}_2\text{S}_3/\text{AgInS}_2$, Pt- $\text{In}_2\text{S}_3/\text{CuInS}_2$, $\text{In}_2\text{S}_3/\text{anatase/rutile TiO}_2$ and Pt- $\text{In}_2\text{S}_3/\text{Cu}_3\text{BiS}_3$ [25,63,124,142,187–190]. Typically, Yang et al. reported a 3D $\text{In}_2\text{S}_3/\text{anatase/rutile TiO}_2$ nanostructured array ($\text{In}_2\text{S}_3/\text{ANP/RND}$) to exhibit outstanding PEC water (and seawater) splitting perfor-

mance [187]. By the deposition of In_2S_3 on the surface of ANP/RND array, additional staggered heterojunction was built to enlarge the band bending in the neutral electrolyte for efficient charge separation (Fig. 9c). The photocurrent density of the $\text{In}_2\text{S}_3/\text{ANP/RND}$ array photoanode (1.57 mA cm^{-2} at $1.23 V_{\text{RHE}}$) in the neutral electrolyte was equal to that of ANP/RND in alkaline electrolyte. The onset potentials of $\text{In}_2\text{S}_3/\text{ANP/RND}$ photoanode were as low as $0.36 V_{\text{RHE}}$. Improved charge separation efficiency from 82 to 94% was observed after the deposition of In_2S_3 , which profited from the dual-staggered heterojunctions. The amount of O_2 generated from PEC water splitting of $\text{In}_2\text{S}_3/\text{ANP/RND}$ photoanode was close to the theoretical value in the neutral electrolyte. And the faradaic efficiency of $\text{In}_2\text{S}_3/\text{ANP/RND}$ photoanode was over 90% during 2 h irradiation, indicating the superior stability and high efficiency [187]. Besides, the deposition of Pt with small hydrogen overpotential is usually a useful technique to improve cathodic photocurrent. Kamimura et al. integrated n-type In_2S_3 and p-type Cu_3BiS_3 to construct p-n $\text{In}_2\text{S}_3/\text{Cu}_3\text{BiS}_3$ heterojunction electrode with Pt deposition [124]. The photocurrent onset potential of the Pt- $\text{In}_2\text{S}_3/\text{Cu}_3\text{BiS}_3$ (0.2 V vs. Ag/AgCl) electrode was more positive than the Pt- Cu_3BiS_3 (0.2 V vs. Ag/AgCl). The photocurrent of the Pt- $\text{In}_2\text{S}_3/\text{Cu}_3\text{BiS}_3$ electrode reached ca. $-110 \mu\text{A cm}^{-2}$ at $0 V_{\text{RHE}}$, 100 times higher than that of Pt- Cu_3BiS_3 (ca. $-2 \mu\text{A cm}^{-2}$ at 0 V), which was ascribed to the efficient charge separation in the depletion region of p-n heterojunction [124]. Thus, the amount of generated H_2 increased with the more negative electrode potential and the calculated faradaic efficiencies kept ca. 80–93% at an entire potential (Fig. 9d) [124]. Very recently, Hou et al. exploited atomically thin 2D mesoporous $\text{In}_2\text{O}_{3-x}/\text{In}_2\text{S}_3$ lateral heterostructure as a photoelectrode for PEC water splitting [25]. Through an in-situ oxygen plasma induced strategy, the In_2S_3 atomic layers were oxidized to mesoporous $\text{In}_2\text{O}_{3-x}/\text{In}_2\text{S}_3$ heterostructures. The $\text{In}_2\text{O}_{3-x}/\text{In}_2\text{S}_3$ mesoporous layers possessed much larger specific surface area ($63 \text{ m}^2 \text{ g}^{-1}$) than the reported In_2S_3 nanosheets ($12 \text{ m}^2 \text{ g}^{-1}$), providing enough contact area for electrolyte penetration. According to density functional theory calculations (Fig. 9e), massive peaks in the band gap of the $\text{In}_2\text{O}_{3-x}/\text{In}_2\text{S}_3$ heterostructures were induced by the oxygen and oxygen-vacancies confined in the In_2S_3 atomic layers. Therefore, the photoconversion efficiency became much higher owing to the strong coupling effects at the atomically thin $\text{In}_2\text{O}_{3-x}/\text{In}_2\text{S}_3$ interface. The photocurrent of $\text{In}_2\text{O}_{3-x}/\text{In}_2\text{S}_3$ photoelectrode reached 1.28 mA cm^{-2} at $1.23 V_{\text{RHE}}$, which was 21 and 79 times larger than that of In_2S_3 atomic layers and bulk In_2S_3 respectively, indicating the significant improvement of lateral heterostructures in the PEC water splitting [25]. The faradaic efficiency of $\text{In}_2\text{O}_{3-x}/\text{In}_2\text{S}_3$ electrode nearly reached 96%. Besides, the $\text{In}_2\text{O}_{3-x}/\text{In}_2\text{S}_3$ photoelectrode exhibited more stable photocurrent than In_2S_3 atomic layers, which proved the anti-photocorrosion of $\text{In}_2\text{O}_{3-x}/\text{In}_2\text{S}_3$ heterostructure (Fig. 9f). Compared with In_2S_3 atomic layers, an increased lifetime of the $\text{In}_2\text{O}_{3-x}/\text{In}_2\text{S}_3$ excited carriers was observed via transient absorption spectroscopy, indicating efficient interfacial charge transport for the enhanced photocatalytic performance. Therefore, the structural benefits of the atomically thin mesoporous $\text{In}_2\text{O}_{3-x}/\text{In}_2\text{S}_3$ accounted for the remarkable PEC water splitting (Fig. 9g) [25]. Distinctly, coupling 2D In_2S_3 atomic layers with lateral or vertical heterostructures is promising to achieve band engineering within the atomic plane for robust high performance in solar-to-fuel conversion.

4.2.2. Biology-assisted photocatalytic hydrogen and oxygen production

To date, constructing an effective electron transfer between inorganic semiconductor and biocatalysts (enzyme or microorganism) for photosynthetic H_2 from water has attracted considerable attention. The photosynthetic biohybrid systems have incorporated the merits of inorganic semiconductors with outstanding

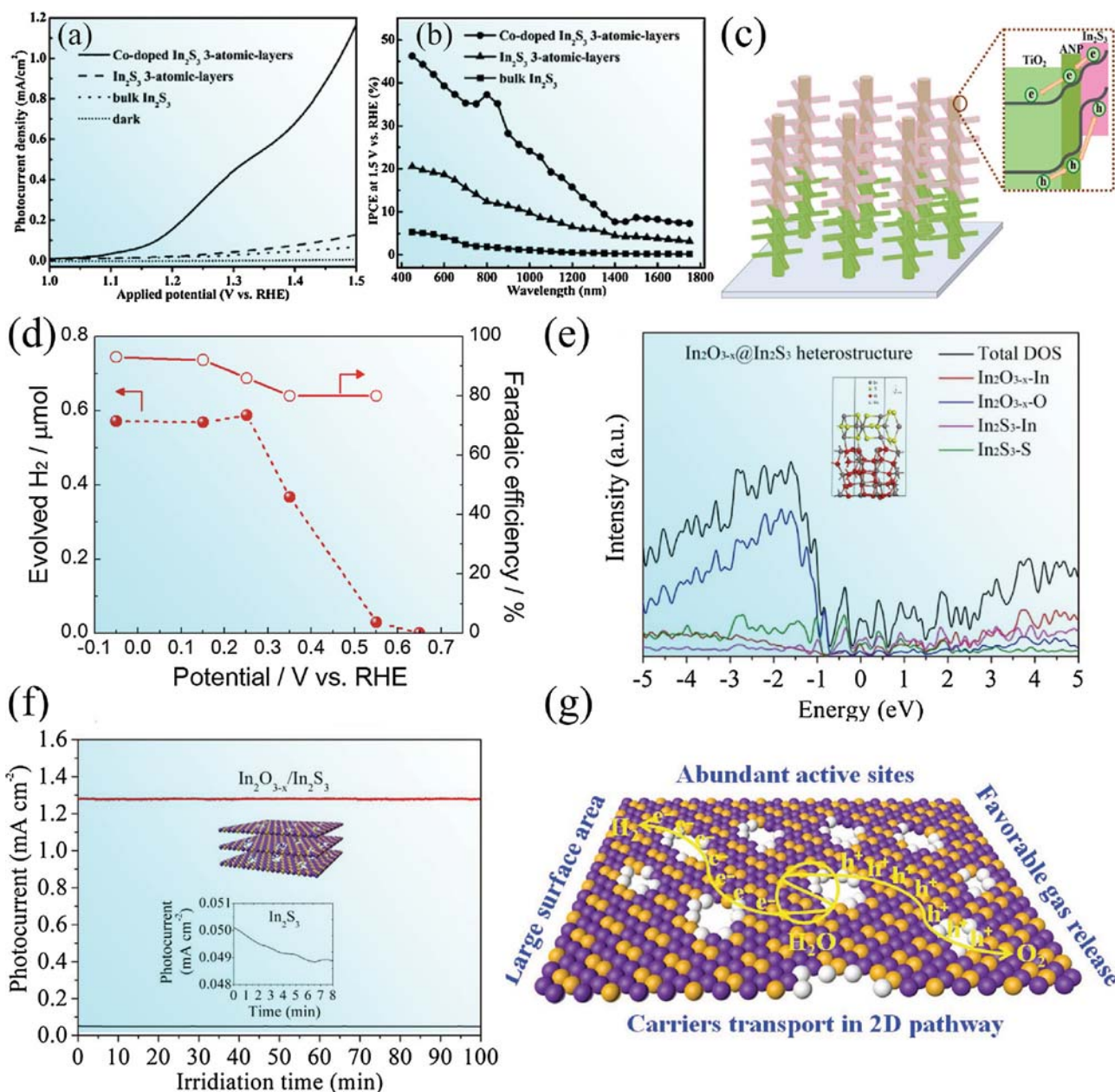


Fig. 9. (a) Photocurrent density and (b) IPCE of Co-doped In_2S_3 three atomic layers, pure In_2S_3 three atomic layers and the bulk counterpart. Adapted with permission [105]. Copyright 2015, Wiley. (c) Schematic of $\text{In}_2\text{S}_3/\text{ANP/RND}$ array photoanode. Adapted with permission [187]. Copyright, 2018, American Chemical Society. (d) H_2 evolution over $\text{Pt-In}_2\text{S}_3/\text{Cu}_3\text{BiS}_3$ electrode in Na_2SO_4 solution (pH 6) at different applied potential. Adapted with permission [124]. Copyright, 2017, Royal Society of Chemistry. (e) The density of states and simulation models of atomically thin $\text{In}_2\text{O}_{3-x}/\text{In}_2\text{S}_3$ heterostructures. (f) Photocurrent density versus time of In_2S_3 layers and $\text{In}_2\text{O}_{3-x}/\text{In}_2\text{S}_3$. (g) Structural benefits for robust broadband-light PEC water splitting of $\text{In}_2\text{O}_{3-x}/\text{In}_2\text{S}_3$ heterostructures. Adapted with permission [25]. Copyright 2017, Wiley.

light-absorbing efficiency and biocatalysts with superior H_2 (or O_2) generation [191–194].

In the pioneering work of Tapia and co-workers, In_2S_3 particles were firstly combined with [NiFeSe] Hydrogenase (Hase) from *Desulfovibrio vulgaris* for photobioproduction of H_2 [192]. In order to build a direct electron transfer between In_2S_3 and Hase, a highly porous surface of In_2S_3 was designed for the immobilization of enzyme into the cavities. As shown in Fig. 10a, the photobiocatalytic generation of H_2 occurred only when Hase was injected and under Vis light irradiation. Further, the incubation time was found to make an influence on the specific activity of hydrogenase and H_2 photobioproduction. The overall activity of Hase attached to the In_2S_3 reached 89% and photobioproduction rate reached highest of $672 \mu\text{mol} (\text{mg of Hase})^{-1} \text{min}^{-1}$ after incubated for 6 h. And the

turnover frequency of the NiFeSe Hase for H_2 photobioproduction reached 986 s^{-1} [192]. Tapia et al. reported a hybrid $\text{In}_2\text{S}_3/\text{Trametes hirsuta}$ laccase ($\text{In}_2\text{S}_3/\text{Thlc}$) photocatalyst for photoelectrochemical oxygen evolution [193]. The current density of $\text{In}_2\text{S}_3/\text{laccase}$ with covalent bond photocatalyst ($50 \mu\text{A cm}^{-2}$) was about 10-fold higher than that of the laccase physically deposited on In_2S_3 photocatalyst. The average turnover frequency $\text{In}_2\text{S}_3/\text{Thlc}$ photoanode for O_2 evolution reached $4.6 \pm 0.1 \text{ s}^{-1}$, equal to that for photosystem II. The onset potential of an $\text{In}_2\text{S}_3/\text{Thlc}$ photocatalyst for the photoelectrochemical oxygen evolution was as low as 1.24V vs RHE at pH 7.1. However, the inactivation of the biocatalyst occurred under Vis light illumination for 6 min because of the photodegradation of enzyme [193].

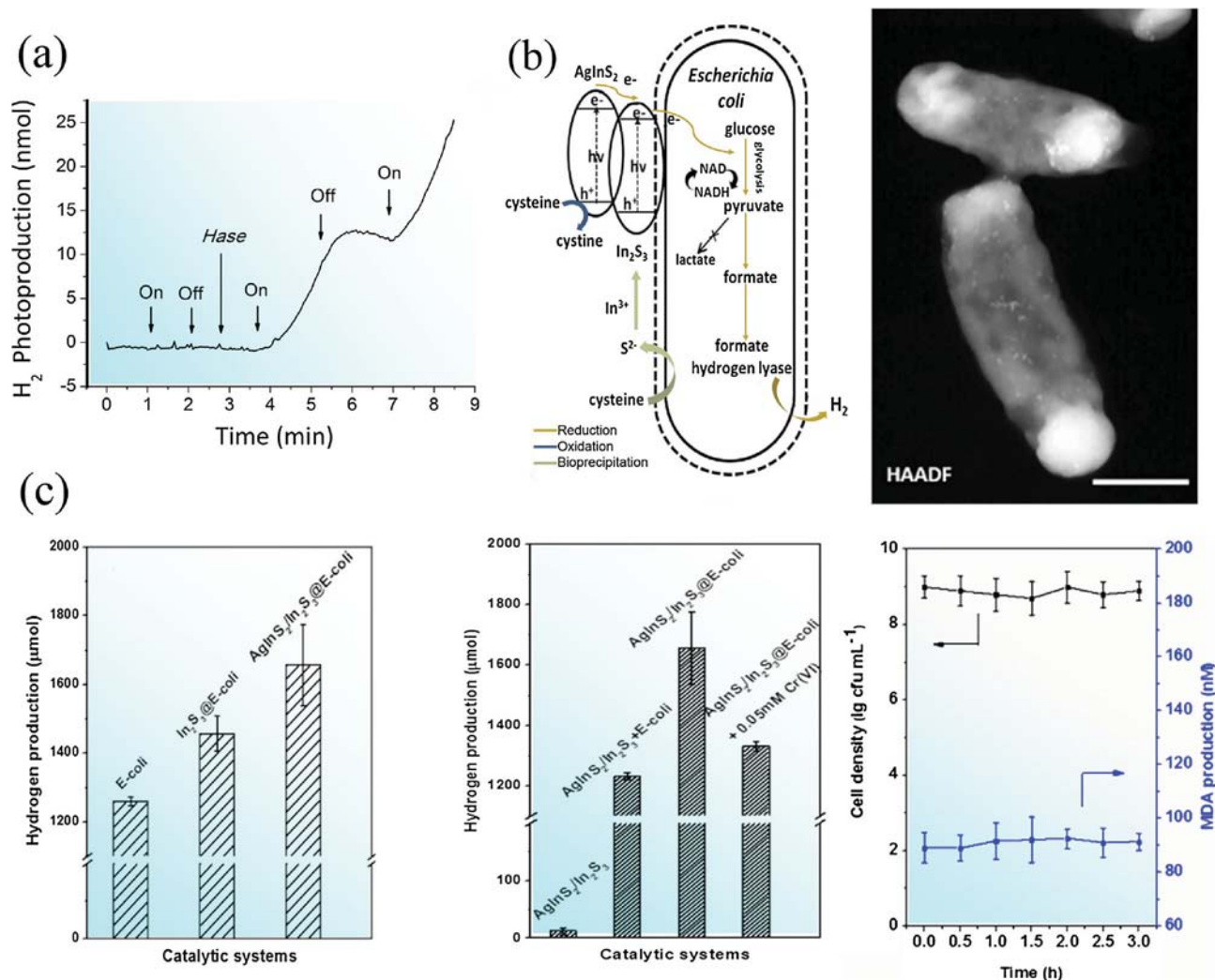


Fig. 10. (a) Photocatalytic H₂ production of In₂S₃ particles and the arrows mark the time at which the lamp is turned on or off and of Hase injection into the reactor vessel. Adapted with permission [192]. Copyright 2016, American Chemical Society. (b) Schematic pathway diagram and HAADF image of AgInS₂/In₂S₃@*E. coli* hybrid. (c) Photocatalytic H₂ production of different hybrid systems, and Cell viability and MDA production during the H₂ production process. Adapted with permission [194]. Copyright 2018, Elsevier.

Recently, without any enzyme purification and genetic modification, Jiang et al. established the AgInS₂/In₂S₃@*E. coli* photosynthetic biohybrid systems by employing low-cost bacterial cell directly [194]. Through the precipitation of In³⁺ ions with sulfide produced from *E. coli*, In₂S₃ nanoparticles were biologically grown on the cell surface. AgInS₂/In₂S₃ heterojunction was formed via in-situ ion exchange and anchored on the surface *E. coli* cells (Fig. 10b). From Fig. 10c, the AgInS₂/In₂S₃@*E. coli* hybrid system exhibited an H₂ evolution amount of 1660 μmol and excellent photobio-stability compared with pure *E. coli*, In₂S₃@*E. coli* hybrid, AgInS₂/In₂S₃ composite and AgInS₂/In₂S₃ + *E. coli* under Vis light for 3 h. And the AQE of the AgInS₂/In₂S₃@*E. coli* hybrid system (3.3% at 720 nm) was higher than many photoheterotrophic bacteria, like *Rhodobacter sphaeroides*, *Rhodobacter capsulatus* etc [195]. Due to the matched band structure, photogenerated electrons transferred from AgInS₂ CB to In₂S₃ CB and finally to *E. coli*, the hybrid cells hence was under the higher stress of reduction potential. As a result, fermentative H₂ production was enhanced under Vis light to maintain the redox balance [194]. Inspired by these favorable semiconductor-biological system, such catalysts struggle to compete with the high-specificity and the self-replicating, self-repairing properties of the biologically photocatalytic energy evolution system.

4.2.3. Carbon-based fuel production from carbon dioxide reduction

Photocatalytic conversion of CO₂ into renewable fuels, imitating natural photosynthesis, has drawn considerable attention to address the environment pressure and global energy [5,6,9,37–39]. In order to break C=O bond of CO₂, a large of energy from the multiple electrons are in demand. Besides, the reduction of highest chemical state (C⁴⁺) of C atoms could only be achieved with the assist of reducing agents (H₂O, H₂, S²⁻, SO₃²⁻, and amines) [5]. H₂O as the most preferred reducing agent has been widely used in the photocatalytic CO₂ reduction, which is an uphill reaction with positive Gibbs free energy to overcome reaction barriers. Exactly, the CB bottom of In₂S₃ is more negative than CO₂ reduction potentials, and the top of VB is more positive than the oxidation potential of H₂O, indicating the possibility of In₂S₃ to the photocatalytic reduction of CO₂ with H₂O into fuels (Fig. 2f).

Photocatalytic reduction of CO₂ via the artificial Z-scheme system, mimicking the overall natural photosynthetic (photosystem I and photosystem II), has aroused the great passion of researchers. Our recent research reported the photocatalytic selective reduction of CO₂ into CO using In₂S₃-CdIn₂S₄ tubular heterostructure as photocatalysts [27]. Owing to the high BET surface area (68 m² g⁻¹) originated from the hierarchical mesoporous structure, In₂S₃-

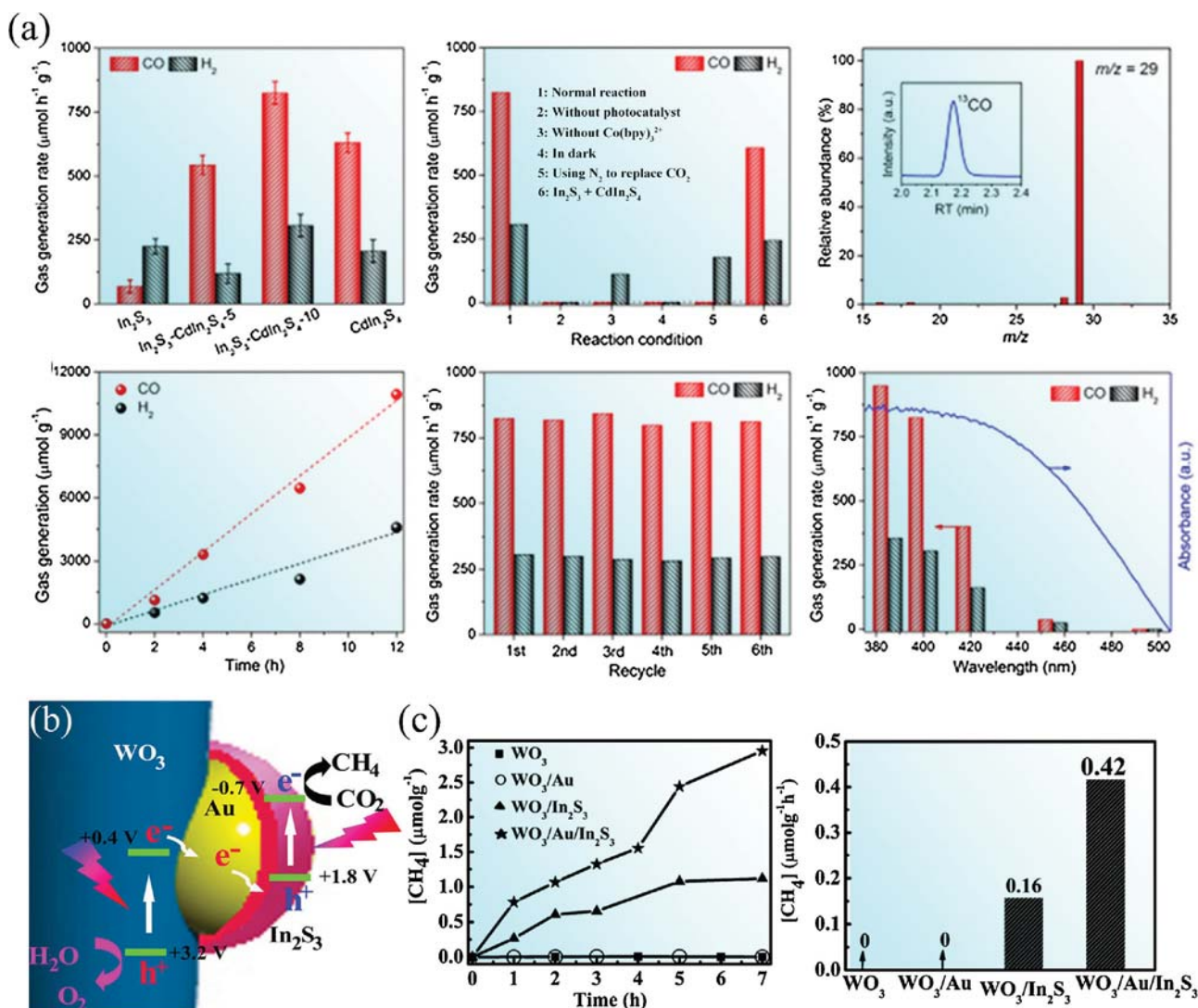


Fig. 11. (a) CO₂ photoreduction performance of In₂S₃-CdIn₂S₄ heterostructured photocatalyst. Adapted with permission [27]. Copyright 2017, American Chemical Society. (b) Schematic of charge separation and transfer in the Z-scheme system of WO₃/Au/In₂S₃. (c) Comparison of photocatalytic activity for CO₂ reduction over different photocatalysts. Adapted with permission [196]. Copyright 2016, American Chemical Society.

CdIn₂S₄ showed a high CO₂ absorption of ca. 25 cm³ g⁻¹ at 760 mm Hg and 0 °C. In the photocatalytic process, H₂O/acetonitrile mixture with Co(bpy)₃²⁺ (bpy = 2'2'-bipyridine) was used as cocatalyst instead of noble metal. The In₂S₃-CdIn₂S₄ heterostructured nanotube exhibited excellent CO production rate of 825 μmol h⁻¹ g⁻¹ (Fig. 11a), which was 12 times higher than pure In₂S₃ nanotubes. Besides, the cocatalyst of Co(bpy)₃²⁺ was found indispensable to efficient CO₂ reduction performance. Then, the production of CO was proved from the photocatalytic reduction of CO₂ through ¹³C-isotopic tracer experiments. The In₂S₃-CdIn₂S₄ heterostructures also possessed superior stability for CO₂ reduction distinguished from most other single metal sulfides, which was attribute to the hierarchical tubular nanostructures [27]. Li et al. constructed a Z-scheme WO₃/Au/In₂S₃ photocatalyst for selective CO₂ reduction to CH₄, in which Au nanoparticles acted as charge mediator between WO₃ and In₂S₃ for a more efficient charge carrier separation. From Fig. 11b, the photoexcited electrons in the CB of WO₃ transferred to the VB of the In₂S₃, which was detected by Kelvin probe force microscopy technique via the change of surface potential. Hence, electrons in the CB of In₂S₃ (-0.7 V vs NHE) reduced CO₂ into CH₄ (-0.24 V vs NHE) and holes in the VB of WO₃ (+3.2 V vs NHE) oxidized H₂O into O₂. Selective CH₄ evolution in the Z-scheme

WO₃/Au/In₂S₃ of 0.42 μmol g⁻¹ h⁻¹ was observed, 2.6 times higher than that in WO₃/In₂S₃ (Fig. 11c) [196]. These works inspired the development of complex photosynthetic assemblies for artificial solar energy-related synthesis.

4.3. Solar cell

The efficient conversion of solar light energy into electric power has been a research hotspot since the discovery of the photoelectric effect by Henri Becquerel. The silicon-based solar cells were the first to appear and be commercialized due to its outstanding conversion efficiency. However, shortcomings of the silicon-based solar cells like low linear absorption coefficients and uneconomic thicker absorbing layers stimulated the generation of thin film solar cells and nanocrystalline solar cells [4]. Owing to the superior photoconductivity and photoelectric conversion efficiency originated from the defect state within the bandgap, In₂S₃ has been widely used as photovoltaic device components in the advance of solar cells, such as buffer layer, emitter, counter electrode, quantum dot sensitizer, passivation layer and electron transport layer [50,139,197–200].

In₂S₃ is famous as an alternative to CdS buffer layer in solar cells because of its low toxicity and comparative performance. The In₂S₃

buffer layer based-Cu(In,Ga)Se₂ (CIGSSe) thin film solar cell exhibited an outstanding power conversion efficiency of 16.4%, achieving a perfect substitute to CdS/CIGSSe solar cell (efficiency of 18.8%) in terms of the balance between environment and energy efficiency [197]. Then, Cu₂ZnSnS₄ and Cu₂ZnSn(S,Se)₄ (CZTSSe) thin film solar cell emerges as a new candidate because of the abundant constituent elements in the earth and relative non-toxicity compared with the well-developed CIGSSe solar cell. Siol et al. utilized pure β-In₂S₃ buffer layers in the Cu₂ZnSnS₄ thin film solar cells by a reactive sputter deposition technique, which could achieve the deposition of pure β-In₂S₃ over a broad range of substrate temperatures via adjusting sulfur partial pressure [201]. The photovoltaic performance of In₂S₃/Cu₂ZnSnS₄ solar cell was found to be strongly related to substrate temperature and thickness. When the substrate temperature was 290 °C, In₂S₃/Cu₂ZnSnS₄-based devices with a thickness of 60–65 nm exhibited equal efficiency (2.0%) to CdS/Cu₂ZnSnS₄ reference cells [201]. Then, Jiang et al. reported a post-heating treatment to improve the conversion efficiency of In₂S₃ buffer layer/Cu₂ZnSnS₄ solar cells [202]. When the thickness of In₂S₃ buffer layer was about 90 nm, the performance of In₂S₃/Cu₂ZnSnS₄ solar cells reached the best with the short-circuit current density (J_{SC}), open-circuit voltage (V_{OC}), fill factor (FF) and power conversion efficiency (PCE) of 585 mV, 17 mA cm⁻², 0.450, and 4.5%, respectively. After a post-heating treatment, improved V_{OC}, J_{SC}, FF, and PEC of 621 mV, 20 mA/cm⁻², 0.545, and 6.9% were achieved in the In₂S₃/Cu₂ZnSnS₄ solar cells, which equally matched the V_{OC} (705 mV), J_{SC} (18 mA cm⁻²), and FF (0.632) of the CdS buffer layer/Cu₂ZnSnS₄ solar cell [202,203]. Through this post-heating treatment, In element vertically diffused into voids of Cu₂ZnSnS₄ grain, leading to a built-in potential across the n-type In₂S₃/Cu₂ZnSnS₄ junction and the final improvement of V_{OC} of the solar cell [202].

In order to address open circuit voltage (V_{OC}) deficit, the essential gap between CIGSSe and CZTSSe solar cell performance, In₂S₃/CdS double emitters were employed in the CZTSSe solar cells by Kim et al. [198]. They deposited In₂S₃ layers on the CdS component and annealed the double-emitter structure to diffuse indium (In) from In₂S₃ into the CdS/CZTSSe layers via rapid thermal annealing, which exhibited 20% improvement of V_{OC} (547 mV) and an improved cell efficiency of 12.7% compared with single CdS emitter. In doping was found to enhance the electron density of CdS and the hole density of CZTSSe, which in turn endowed the CZTSSe solar cells with comparative photovoltaic performance to CIGSSe solar cells [198,204]. As shown in Fig. 12a, the double-emitter CZTSSe cell overcame the efficiency collapse at low temperature (lower than 200 °C) and the V_{OC} monotonically increased with the light intensity without any saturation, which behaved efficiently as CIGSSe solar cells [198].

Serving as a counter electrode in dye-sensitized solar cells, the In₂S₃ nanotubes/reduced graphene oxide (In₂S₃/rGO NTs) composites have been exploited by Guo et al. in which the composites showed remarkably higher PCE of 8.01% than that of the commercial Pt-counter electrode (7.18%) [139]. The In₂S₃/rGO NTs also exhibited the best J_{SC} of 15.48 mA cm⁻², V_{OC} of 0.78 V and FF of 0.66 compared with Pt, bulk In₂S₃/rGO, and pure In₂S₃ counter electrodes [139]. In the traditional I⁻/I₃⁻ electrolyte, the smooth large surface of In₂S₃/rGO NTs accelerated electron transfer across the counter electrode/substrate interface, which was beneficial to the electrocatalytic reduction of I⁻/I₃⁻ and finally promoted the power conversion efficiency [139]. Kim et al. utilized In₂S₃ particles as scattering layer of the incident light path to fabricate TiO₂/In₂S₃ double layered electrode for dye-sensitized solar cells [205]. The maximum PCE, V_{OC}, J_{SC}, FF of TiO₂/In₂S₃ dye-sensitized solar cells reached 5.80%, 0.69 V, 12.36 mA cm⁻² and 0.68, respectively. From Fig. 12b, the deposition of In₂S₃ on TiO₂ electrode brought about a more matched band structure between the N719 dye and the

TiO₂ electrode, thus making it easier for charge carriers transfer to improve the power conversion efficiency [205].

Due to the advantages over organic dyes sensitizer like low-cost, satisfactory molar extinction coefficient, quantum size effect and multiple faction generations of quantum dots, quantum dot-sensitized solar cells have evolved from the dye-sensitized solar cells. Duan et al. firstly employed In₂S₃ quantum dot as sensitizer on the TiO₂ anodes. And the In₂S₃ quantum dot sensitized solar cells possessed a power conversion efficiency of 1.30% [200]. Wang et al. prepared a CuInS₂ quantum dots/In₂S₃ co-sensitized TiO₂ photoanodes, which showed improved photovoltaic performance with PCE of 1.62%, J_{SC} of 6.49 mA cm⁻², V_{OC} of 0.50 V, FF of 0.50 [206]. In₂S₃ as a buffer layer on the interface of TiO₂ and CuInS₂ quantum-dots not only extend optical adsorption but also suppress the charge recombination, thus leading to the enhanced power conversion efficiency [206]. Further, Basit et al. reported In₂S₃ as a passivation layer for PbS quantum dot-based photoanodes to coalesce the improvement of J_{SC} and V_{OC} [199]. The PCE of In₂S₃/PbS multilayered photoanode was 3.75%, which was 18% higher than that of PbS standard quantum dot-sensitized solar cells. The passivation of the surface states of PbS quantum dots, which acted as recombination centers, was achieved by the deposition of the In₂S₃ passivation layer. In Fig. 12c, the deposition of In₂S₃ as a passivation layer restricted the recombination with the electrolyte for the higher CB position, resulting in an improved open-circuit voltage. While the hole transfer at PbS quantum dots/electrolyte interface was more difficult because of the lower VB position of In₂S₃, hindering the increase of short-circuiting photocurrent density [199]. Hence, Basit and co-workers deposited CdS layer prior to PbS to construct a CdS/PbS/In₂S₃ multilayered photoanode. The J_{SC} was increased from 21.6 to 25.7 mA cm⁻² by the improved loading of PbS quantum dots originated from the deposition of CdS (Fig. 12d) [199,207]. The PCE of CdS/PbS/In₂S₃ solar cell finally reached 4.3% [199].

To date, In₂S₃ nanoflakes array was reported to be used as an electron transport layer (ETL) in organic-inorganic perovskite solar cells (PSCs) as shown in Fig. 12e [50]. The perovskite solar cells based on In₂S₃ ETL showed significantly higher PCE of 18.22% than that on TiO₂ ETL (15.70%). According to the current density-voltage (J–V) characteristics of In₂S₃ ETL and TiO₂ ETL based CH₃NH₃PbI₃ PSCs (Fig. 12f), the In₂S₃ ETL based device demonstrated a J_{SC} of 22.40 mA cm⁻², V_{OC} of 1020.00 mV and FF of 0.69. While the TiO₂ ETL based device exhibited poor J–V performance with lower J_{SC} (19.70 mA cm⁻²) and V_{OC} (982.19 mV). The more matched band structure between In₂S₃ and CH₃NH₃PbI₃ leads to a lower energy barrier for electron transfer from the perovskite layer into In₂S₃ ETL than that of TiO₂ ETL (Fig. 12e). Besides, the improved light harvesting ability and high charge recombination resistance by the deposition of In₂S₃ ETL accounts for the superior power conversion efficiency [50]. Indeed, many In₂S₃-based photovoltaic systems have also served as remarkable photocatalysts in the similar heterostructures or the individual state, which in turn makes it feasible to excavate more efficient In₂S₃-based components for the solar cell from its optimized photocatalytic systems.

5. Conclusions and perspectives

Solar-energy conversion and utilization can be divided into three areas on the basis of different reaction induced by the solar light, that is, photocatalytic environmental decontamination, artificial photosynthesis for renewable fuels, and solar cells. As an efficient visible-light harvester, In₂S₃-based photocatalytic, photoelectrocatalytic and photovoltaic systems have been extensively investigated in the photoconversion field. Distinctively, In₂S₃ with a host of vacancies or defects possesses many fascinating properties including superior photo-absorption coefficient, photoelectric

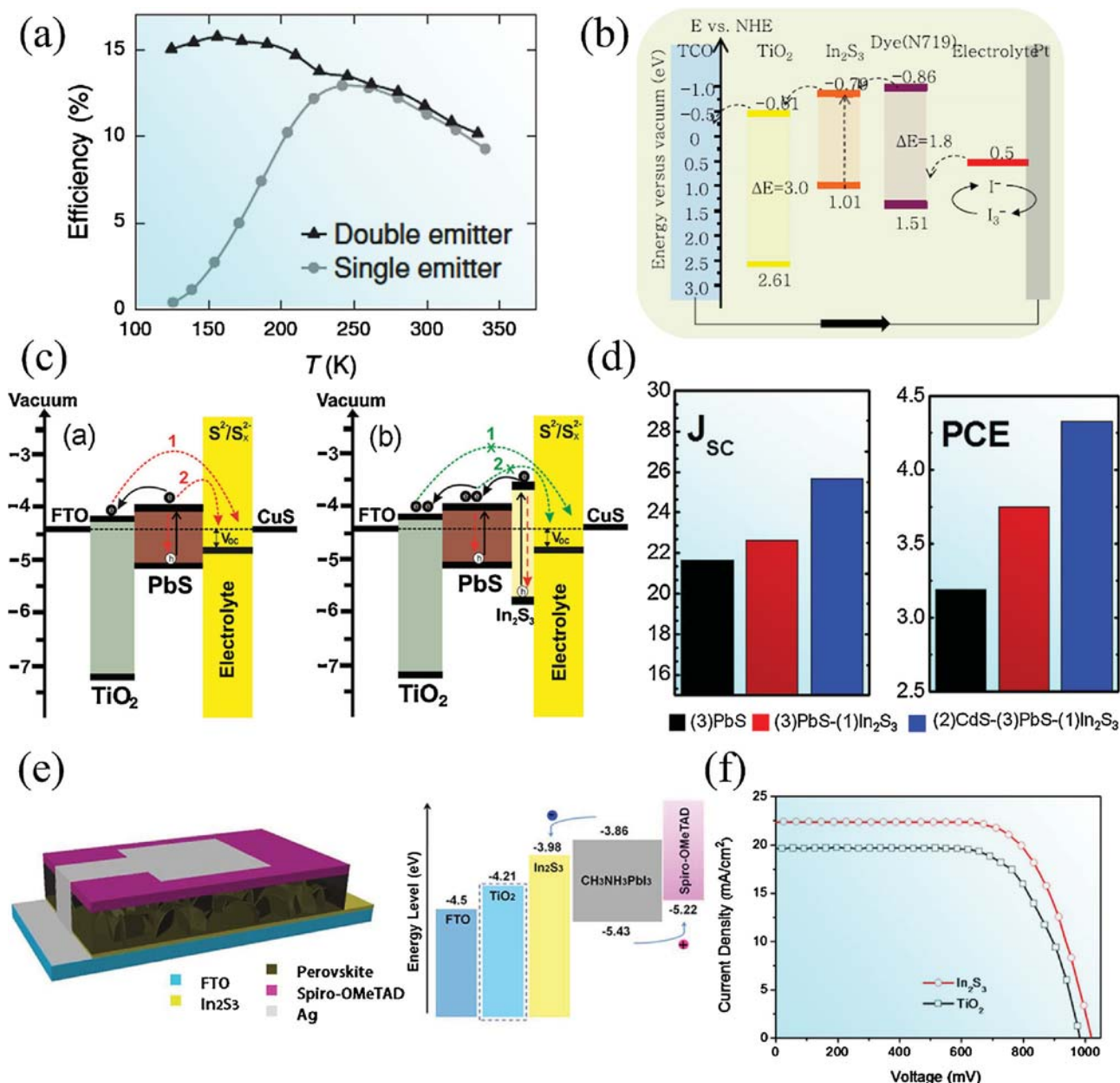


Fig. 12. (a) Efficiency versus temperature of a single-emitter cell and a double-emitter cell. Adapted with permission [198]. Copyright 2014, Wiley. (b) Schematic of electronic band structure of TiO₂/In₂S₃ dye-sensitized solar cells. Adapted with permission [205]. Copyright 2015, Elsevier. (c) Schematic of electronic band structure of PbS standard quantum-dot-sensitized solar cells and In₂S₃/PbS/TiO₂ quantum-dot-sensitized solar cells. Adapted with permission [199]. Copyright 2016, Elsevier. (d) Trends in J_{SC} and PCE of all PbS-based quantum-dot-sensitized solar cells. Adapted with permission [199]. Copyright 2016, Elsevier. (e) Device architecture and electronic band structure of a typical perovskite solar cell. (f) Current density-voltage curves of perovskite solar cells based on In₂S₃ and TiO₂ ETLs. Adapted with permission [50]. Copyright 2017, Elsevier.

sensitivity, favorable carrier mobility ($17.6 \text{ cm}^2 \text{ V}^{-1} \text{ s}^{-1}$), moderate band gap (2.0–2.3 eV), excellent stability and low toxicity. These features provide a solid scaffold for In₂S₃ to be tailored for the optimized solar-to-chemical and solar-to-electric conversion.

To gain superior photoconversion performance in different fields, a massive effort has been devoted via defective engineering, doping, and hybridization with inorganic materials or bio-molecules. Firstly, defective designing towards modulation of atomic arrangement and vacancies distribution in crystalline structure or assembling 2D nanosheets into other dimensionalities in the morphologic structure is a promising direction. Secondly, the transition metal ions and rare earth ions doping mainly extend the absorption spectrum of In₂S₃ and make it possible for In₂S₃ to be responsive even in NIR light irradiation. Thirdly, coupling In₂S₃

with another semiconductor (metal sulfides, noble metal, metal-oxide, metal-organic frameworks) to building heterostructures achieves efficient charge separation and conquers the photo-corrosion of In₂S₃. Besides, In₂S₃-based bio-hybrid systems can happily combine the efficient light absorption of In₂S₃ and specific biological catalytic power to maximize solar energy.

Based on the vivid progress, we propose several perspectives favorable to the advance of In₂S₃-based photoconversion systems as following aspects: (i) Structure modulation towards atomic level is promising, such as regulating vacancy distribution of In₂S₃ atomic sheets, doping single atom in the atomic layers of In₂S₃ or filling intrinsic vacancy of In₂S₃ with heteroatom. What's more, fabricating 2D layered In₂S₃ with mixed low dimensions structure (0D/2D, 1D/2D, etc.) or coupling In₂S₃ with latest materials,

such as MXene, black phosphorus, boronene, and phosphine is likely to open a new door in solar energy maximum utilization. (ii) A comprehensive understanding of the photoconversion reaction mechanism is still necessary not only about the charge carrier transfer mechanism but also the kinetics and thermodynamics on the surface of the semiconductor. Based on the atomic level In_2S_3 structure, the combination of building models, theoretical calculation and in situ spectroelectrochemistry is accessible to meet this end and figure out the relationship between structure and photoactivity of In_2S_3 -based photoconversion systems [208]. (iii) From the perspective of photoconversion applications, a broad field for integrating In_2S_3 -based hybrids with bio-molecules/microorganism is open for the artificially photosynthetic renewable fuels and photo-biological CO_2 fixation [209]. Such catalysts struggle to compete with the high-specificity and the self-replicating, self-repairing properties of the biologically photocatalytic energy evolution system. Expanding the material library available through biologically induced In_2S_3 -based precipitation is a promising trend to increase the light-absorption capacity and raise the upper limit on In_2S_3 -bacteria photosynthetic efficiency. (iv) Ammonia synthesis from the N_2 fixation under ambient temperature and pressure is a hot direction. It has preliminarily indicated that the N_2 fixation activity of BiOBr and $g\text{-C}_3\text{N}_4$ were both improved by introducing oxygen vacancies and nitrogen vacancies, respectively [210–212]. Inspired by these pioneering studies, In_2S_3 has great potential for photocatalytic N_2 fixation due to its rich intrinsic sulfur vacancies. However, there is still a lack of reports with respect to In_2S_3 -based photocatalysts for N_2 fixation. What's more, In_2S_3 -based hybrids with favorable photochemical and photo-absorption properties can serve as an inspiration for the components of the solar cell, owing to the similar roots of light-harvesting systems. For example, the light is harvested with In_2S_3 -based materials-incorporating photocathode in a solar cell, where the sensitizer supplies the VB holes to the p-conducting metal oxide scaffold and accepts electrons from a redox-shuttle in the electrolyte. This strategy is further expected to extend to tandem cells combining a photocathode and a photoanode both absorbing the solar light and contributing to the photocurrent generation for bringing breakthrough of the solar cell efficiency. In a nutshell, research on In_2S_3 -based materials is a prosperous area but still needs much more attention under the framework of metal sulfide nanomaterials.

Conflicts of interest

There are no conflicts to declare.

Acknowledgments

The authors gratefully acknowledge the financial support provided by the Foundation for Innovative Research Groups of the National Natural Science Foundation of China (No. 51521006), the Key Project of National Nature Science Foundation of China (No. 71431006), Key research and development project of Hunan Province, China (No. 2016SK2015) and the Projects of the National Nature Science Foundation of China (No. 21776066, 51708195).

References

- [1] A. Fujishima, K. Honda, Electrochemical photolysis of water at a semiconductor electrode, *Nature* 238 (1972) 37–38.
- [2] J. Liu, Y. Liu, N. Liu, Y. Han, X. Zhang, H. Huang, Y. Lifshitz, S.T. Lee, J. Zhong, Z. Kang, Metal-free efficient photocatalyst for stable visible water splitting via a two-electron pathway, *Science* 347 (2015) 970–974.
- [3] Z.J. Han, F. Qiu, R. Eisenberg, P.L. Holland, T.D. Krauss, Robust photogeneration of H_2 in water using semiconductor nanocrystals and a nickel catalyst, *Science* 338 (2012) 1321–1324.
- [4] O. Stroyuk, A. Raevskaya, N. Gaponik, Solar light harvesting with multinary metal chalcogenide nanocrystals, *Chem. Soc. Rev.* (2018).
- [5] W. Tu, Y. Zhou, Z. Zou, Photocatalytic conversion of CO_2 into renewable hydrocarbon fuels: state-of-the-art accomplishment, challenges, and prospects, *Adv. Mater.* 26 (2014) 4607–4626.
- [6] W. Tu, Y. Zhou, Q. Liu, Z. Tian, J. Gao, X. Chen, H. Zhang, J. Liu, Z. Zou, Robust hollow spheres consisting of alternating titania nanosheets and graphene nanosheets with high photocatalytic activity for CO_2 conversion into renewable fuels, *Adv. Funct. Mater.* 22 (2012) 1215–1221.
- [7] H. Wang, Y. Wu, X. Yuan, G. Zeng, J. Zhou, X. Wang, J.W. Chew, Clay-inspired mxene-based electrochemical devices and photo-electrocatalyst: state-of-the-art progresses and challenges, *Adv. Mater.* 30 (2018) 1704561.
- [8] Y. Yan, J. Chen, N. Li, J. Tian, K. Li, J. Jiang, J. Liu, Q. Tian, P. Chen, Systematic bandgap engineering of graphene quantum dots and applications for photocatalytic water splitting and CO_2 reduction, *ACS Nano* 12 (2018) 3523–3532.
- [9] C. Gao, S. Chen, Y. Wang, J. Wang, X. Zheng, J. Zhu, L. Song, W. Zhang, Y. Xiong, Heterogeneous single-atom catalyst for visible-light-driven high-turnover CO_2 reduction: the role of electron transfer, *Adv. Mater.* 30 (2018) 1704624.
- [10] F. Bonaccorso, L. Colombo, G. Yu, M. Stoller, V. Tozzini, A.C. Ferrari, R.S. Ruoff, V. Pellegrini, Graphene, related two-dimensional crystals, and hybrid systems for energy conversion and storage, *Science* 347 (2015) 1246501.
- [11] W.J. Ong, L.L. Tan, Y.H. Ng, S.T. Yong, S.P. Chai, Graphitic carbon nitride ($g\text{-C}_3\text{N}_4$)-Based photocatalysts for artificial photosynthesis and environmental remediation: are we a step closer to achieving sustainability? *Chem. Rev.* 116 (2016) 7159–7329.
- [12] D.J. Martin, G. Liu, S.J. Moniz, Y. Bi, A.M. Beale, J. Ye, J. Tang, Efficient visible driven photocatalyst, silver phosphate: performance, understanding and perspective, *Chem. Soc. Rev.* 44 (2015) 7808–7828.
- [13] J.W. Fu, J.G. Yu, C.J. Jiang, B. Cheng, $g\text{-C}_3\text{N}_4$ -Based heterostructured photocatalysts, *Adv. Energy Mater.* 8 (2018) 1701503.
- [14] J. Low, J. Yu, M. Jaroniec, S. Wageh, A.A. Al-Ghamdi, Heterojunction photocatalysts, *Adv. Mater.* 29 (2017) 1601694.
- [15] Z. Zou, J. Ye, K. Sayama, H. Arakawa, Direct splitting of water under visible light irradiation with an oxide semiconductor photocatalyst, *Nature* 414 (2001) 625–627.
- [16] Q. Wang, T. Hisatomi, Q. Jia, H. Tokudome, M. Zhong, C. Wang, Z. Pan, T. Takata, M. Nakabayashi, N. Shibata, Y. Li, D.D. Sharp, A. Kudo, T. Yamada, K. Domen, Scalable water splitting on particulate photocatalyst sheets with a solar-to-hydrogen energy conversion efficiency exceeding 1, *Nat. Mater.* 15 (2016) 611–615.
- [17] C. Liu, D. Kong, P.C. Hsu, H. Yuan, H.W. Lee, Y. Liu, H. Wang, S. Wang, K. Yan, D. Lin, P.A. Maraccini, K.M. Parker, A.B. Boehm, Y. Cui, Rapid water disinfection using vertically aligned MoS_2 nanofilms and visible light, *Nat. Nanotechnol.* 11 (2016) 1098–1104.
- [18] J. Liu, H. Wang, J. Bai, T. Li, Y. Yang, Y. Peng, B. Wang, Gram-scale synthesis of aligned C_3N_4 -polypyrrole heterojunction aerogels with tunable band structures as efficient visible and near infrared light-driven metal-free photocatalysts, *J. Mater. Chem. A* 5 (2017) 24920–24928.
- [19] Z. Zhang, J. Huang, Y. Fang, M. Zhang, K. Liu, B. Dong, A nonmetal plasmonic Z-Scheme photocatalyst with UV- to NIR-Driven photocatalytic protons reduction, *Adv. Mater.* 29 (2017) 1606688.
- [20] Y. Li, Z. Wang, T. Xia, H. Ju, K. Zhang, R. Long, Q. Xu, C. Wang, L. Song, J. Zhu, Implementing metal-to-Ligand charge transfer in organic semiconductor for improved visible-near-infrared photocatalysis, *Adv. Mater.* 28 (2016) 6959–6965.
- [21] T. Simon, N. Bouchonville, M.J. Berr, A. Vaneski, A. Adrovic, D. Volbers, R. Wyrwich, M. Doblinger, A.S. Susha, A.L. Rogach, F. Jackel, J.K. Stolarczyk, J. Feldmann, Redox shuttle mechanism enhances photocatalytic H_2 generation on Ni-decorated CdS nanorods, *Nat. Mater.* 13 (2014) 1013–1018.
- [22] J. Li, X. Wu, W. Pan, G. Zhang, H. Chen, Vacancy-rich monolayer BiO_{2-x} as a highly efficient UV, visible, and near-infrared responsive photocatalyst, *Angew. Chem. Int. Ed. Engl.* 57 (2018) 491–495.
- [23] Y. Sang, Z. Zhao, M. Zhao, P. Hao, Y. Leng, H. Liu, From UV to near-infrared, WS_2 nanosheet: a novel photocatalyst for full solar light spectrum photodegradation, *Adv. Mater.* 27 (2015) 363–369.
- [24] W. Huang, L. Gan, H. Yang, N. Zhou, R. Wang, W. Wu, H. Li, Y. Ma, H. Zeng, T. Zhai, Controlled synthesis of ultrathin 2D $\beta\text{-In}_2\text{S}_3$ with broadband photoresponse by chemical vapor deposition, *Adv. Funct. Mater.* 27 (2017) 1702448.
- [25] J. Hou, S. Cao, Y. Sun, Y. Wu, F. Liang, Z. Lin, L. Sun, Atomically thin mesoporous $\text{In}_2\text{O}_{3-x}/\text{In}_2\text{S}_3$ lateral heterostructures enabling robust broadband-light photo-electrochemical water splitting, *Adv. Energy Mater.* 8 (2018) 1701114.
- [26] H. Wang, Y. Wu, T. Xiao, X. Yuan, G. Zeng, W. Tu, S. Wu, H.Y. Lee, Y.Z. Tan, J.W. Chew, Formation of quasi-core-shell In_2S_3 /anatase TiO_2 @metallic $\text{Ti}_3\text{C}_2\text{T}_x$ hybrids with favorable charge transfer channels for excellent visible-light-photocatalytic performance, *Appl. Catal. B* 233 (2018) 213–225.
- [27] S. Wang, B.Y. Guan, Y. Lu, X.W.D. Lou, Formation of hierarchical $\text{In}_2\text{S}_3\text{-CdIn}_2\text{S}_4$ heterostructured nanotubes for efficient and stable visible light CO_2 reduction, *J. Am. Chem. Soc.* 139 (2017) 17305–17308.
- [28] Z. Wu, X. Yuan, G. Zeng, L. Jiang, H. Zhong, Y. Xie, H. Wang, X. Chen, H. Wang, Highly efficient photocatalytic activity and mechanism of $\text{Yb}^{3+}/\text{Tm}^{3+}$ codoped In_2S_3 from ultraviolet to near infrared light towards chromium (VI) reduction and rhodamine B oxydative degradation, *Appl. Catal. B* 225 (2018) 8–21.

- [29] X. Xie, G. Shen, Single-crystalline In_2S_3 nanowire-based flexible visible-light photodetectors with an ultra-high photoresponse, *Nanoscale* 7 (2015) 5046–5052.
- [30] C.H. Ho, Y.P. Wang, Y.S. Huang, Optical characterization of band-edge property of In_6S_7 compound, *Appl. Phys. Lett.* 100 (2012) 131905.
- [31] J.A. Hollingsworth, D.M. Poojary, A. Clearfield, W.E. Buhro, Catalyzed growth of a metastable InS crystal structure as colloidal crystals, *J. Am. Chem. Soc.* 122 (2000) 3562–3563.
- [32] J. Li, Y. Ma, Z. Ye, M. Zhou, H. Wang, C. Ma, D. Wang, P. Huo, Y. Yan, Fast electron transfer and enhanced visible light photocatalytic activity using multi-dimensional components of carbon quantum dots@3D daisy-like In_2S_3 /single-wall carbon nanotubes, *Appl. Catal. B* 204 (2017) 224–238.
- [33] W. Gao, W. Liu, Y. Leng, X. Wang, B. Hu, D. Yu, Y. Sang, H. Liu, In_2S_3 nanomaterial as a broadband spectrum photocatalyst to display significant activity, *Appl. Catal. B* 176–177 (2015) 83–90.
- [34] A. Kudo, Y. Miseki, Heterogeneous photocatalyst materials for water splitting, *Chem. Soc. Rev.* 38 (2009) 253–278.
- [35] M. Dan, Q. Zhang, S. Yu, A. Prakash, Y. Lin, Y. Zhou, Noble-metal-free $\text{MnS}/\text{In}_2\text{S}_3$ composite as highly efficient visible light driven photocatalyst for H_2 production from H_2S , *Appl. Catal. B* 217 (2017) 530–539.
- [36] W. Tu, Y. Zhou, Z. Zou, Versatile graphene-promoting photocatalytic performance of semiconductors: basic principles, synthesis, solar energy conversion, and environmental applications, *Adv. Funct. Mater.* 23 (2013) 4996–5008.
- [37] W. Tu, Y. Zhou, Q. Liu, S. Yan, S. Bao, X. Wang, M. Xiao, Z. Zou, An in situ simultaneous reduction-hydrolysis technique for fabrication of TiO_2 -Graphene 2D sandwich-like hybrid nanosheets: graphene-promoted selectivity of photocatalytic-driven hydrogenation and coupling of CO_2 into methane and ethane, *Adv. Funct. Mater.* 23 (2013) 1743–1749.
- [38] S. Wang, B.Y. Guan, X.W.D. Lou, Construction of ZnIn_2S_4 - In_2O_3 hierarchical tubular heterostructures for efficient CO_2 photoreduction, *J. Am. Chem. Soc.* 140 (2018) 5037–5040.
- [39] S. Wang, B.Y. Guan, X.W. Lou, Rationally designed hierarchical N-doped carbon@ NiCo_2O_4 double-shelled nanoboxes for enhanced visible light CO_2 reduction, *Energy Environ. Sci.* 11 (2018) 306–310.
- [40] R. Diehl, R. Nitsche, Vapour growth of three In_2S_3 modifications by iodine transport, *J. Cryst. Growth* 28 (1975) 306–310.
- [41] X. Lai, F. Zhu, Y. Wu, R. Huang, X. Wu, Q. Zhang, K. Yang, S. Qin, New high-pressure polymorph of In_2S_3 with defect Th_3P_4 -type structure, *J. Solid State Chem.* 210 (2014) 155–159.
- [42] R. Bayon, J. Herrero, Structure and morphology of the indium hydroxy sulfide thin films, *Appl. Surf. Sci.* 158 (2000) 49–57.
- [43] X. Fu, X. Wang, Z. Chen, Z. Zhang, Z. Li, D.Y.C. Leung, L. Wu, X. Fu, Photocatalytic performance of tetragonal and cubic β - In_2S_3 for the water splitting under visible light irradiation, *Appl. Catal. B* 95 (2010) 393–399.
- [44] P. Pistor, J.M. Merino Alvarez, M. Leon, M. di Michiel, S. Schorr, R. Klenk, S. Lehmann, Structure reinvestigation of alpha-, beta- and gamma- In_2S_3 , *Acta Crystallogr. Sect. B: Struct. Sci. Cryst. Eng. Mater.* 72 (2016) 410–415.
- [45] P. Ghaderi Sheikhi abadi, M. Salavati-Niasari, F. Davar, Hydrothermal synthesis, characterization and optical properties of 3D flower like indium sulfide nanostructures, *Superlattices Microstruct.* 53 (2013) 76–88.
- [46] Y. Sim, J. Kim, M.-J. Seong, Simple synthesis of ultra-high quality In_2S_3 thin films on InAs substrates, *J. Alloys Compd.* 685 (2016) 518–522.
- [47] R. Jayakrishnan, T.T. John, C.S. Kartha, K.P. Vijayakumar, D. Jain, L.S.S. Chandra, V. Ganesan, Do the grain boundaries of β - In_2S_3 thin films have a role in sub-band-gap photosensitivity to 632.8nm? *J. Appl. Phys.* 103 (2008) 053106.
- [48] R.K. Sharma, Y.N. Chouryal, S. Chaudhari, J. Saravanakumar, S.R. Dey, P. Ghosh, Adsorption-driven catalytic and photocatalytic activity of phase tuned In_2S_3 nanocrystals synthesized via ionic liquids, *ACS Appl. Mater. Interfaces* 9 (2017) 11651–11661.
- [49] Y. Sharma, P. Srivastava, Electronic, optical and transport properties of α -, β - and γ -phases of spinel indium sulphide: an ab initio study, *Mater. Chem. Phys.* 135 (2012) 385–394.
- [50] Y. Hou, X. Chen, S. Yang, Y.L. Zhong, C. Li, H. Zhao, H.G. Yang, Low-temperature processed In_2S_3 electron transport layer for efficient hybrid perovskite solar cells, *Nano Energy* 36 (2017) 102–109.
- [51] Q.-L. Meng, S. Kong, Z. Huang, Y. Zhu, H.-C. Liu, X. Lu, P. Jiang, X. Bao, Simultaneous enhancement in the power factor and thermoelectric performance of copper sulfide by In_2S_3 doping, *J. Mater. Chem. A* 4 (2016) 12624–12629.
- [52] Y.X. Chen, A. Yamamoto, T. Takeuchi, Doping effects of Mg for In on the thermoelectric properties of β - In_2S_3 bulk samples, *J. Alloys Compd.* 695 (2017) 1631–1636.
- [53] Z. Zhao, Y. Cao, J. Yi, X. He, C. Ma, J. Qiu, Band-edge electronic structure of beta- In_2S_3 : the role of s or p orbitals of atoms at different lattice positions, *Chemphyschem* 13 (2012) 1551–1556.
- [54] Y.X. Chen, K. Kitahara, T. Takeuchi, Thermoelectric properties of β -Indium sulfide with sulphur deficiencies, *J. Appl. Phys.* 118 (2015) 245103.
- [55] C.-H. Ho, The study of below and above band-edge imperfection states in In_2S_3 solar energy materials, *Physica B Condens. Matter* 407 (2012) 3052–3055.
- [56] H. Cansizoglu, M.F. Cansizoglu, M. Finckenor, T. Karabacak, Optical absorption properties of semiconducting nanostructures with different shapes, *Adv. Opt. Mater.* 1 (2013) 158–166.
- [57] W. Jiang, W. Luo, J. Wang, M. Zhang, Y. Zhu, Enhancement of catalytic activity and oxidative ability for graphitic carbon nitride, *J. Photochem. Photobiol. C* 28 (2016) 87–115.
- [58] D. Chen, R.A. Caruso, Recent progress in the synthesis of spherical titania nanostructures and their applications, *Adv. Funct. Mater.* 23 (2013) 1356–1374.
- [59] R. Sumi, A.R. Warrier, C. Vijayan, Visible-light driven photocatalytic activity of β -indium sulfide (In_2S_3) quantum dots embedded in Nafion matrix, *J. Phys. D: Appl. Phys.* 47 (2014) 105103.
- [60] X. Cao, L. Gu, L. Zhuge, W. Qian, C. Zhao, X. Lan, W. Sheng, D. Yao, Template-free preparation and characterization of hollow indium sulfide nanospheres, *Colloids Surf. A* 297 (2007) 183–190.
- [61] A. Mumtaz, N.M. Mohamed, M. Mazhar, M.A. Ehsan, M.S. Mohamed Saheed, Core-shell vanadium modified Titania/ β - In_2S_3 hybrid nanorod arrays for superior interface stability and photochemical activity, *ACS Appl. Mater. Interfaces* 8 (2016) 9037–9049.
- [62] Y. Tian, L. Wang, H. Tang, W. Zhou, Ultrathin two-dimensional β - In_2S_3 nanocrystals: oriented-attachment growth controlled by metal ions and photoelectrochemical properties, *J. Mater. Chem. A* 3 (2015) 11294–11301.
- [63] M. Li, X. Tu, Y. Su, J. Lu, J. Hu, B. Cai, Z. Zhou, Z. Yang, Y. Zhang, Controlled growth of vertically aligned ultrathin In_2S_3 nanosheet arrays for photoelectrochemical water splitting, *Nanoscale* 10 (2018) 1153–1161.
- [64] S. Sarkar, A.D.P. Leach, J.E. Macdonald, Folded nanosheets: a new mechanism for nanodisk formation, *Chem. Mater.* 28 (2016) 4324–4330.
- [65] B. Chai, P. Zeng, X. Zhang, J. Mao, L. Zan, T. Peng, Walnut-like In_2S_3 microspheres: ionic liquid-assisted solvothermal synthesis, characterization and formation mechanism, *Nanoscale* 4 (2012) 2372–2377.
- [66] Y. Cheng, H. Niu, J. Chen, J. Song, C. Mao, S. Zhang, C. Chen, Y. Gao, Highly stable hierarchical flower-like β - In_2S_3 assembled from 2D nanosheets with high adsorption-photodecoloration activities for the treatment of wastewater, *J. Nanopart. Res.* 19 (2017) 166.
- [67] S. Rengaraj, S. Venkataraj, C.W. Tai, Y. Kim, E. Repo, M. Sillanpaa, Self-assembled mesoporous hierarchical-like In_2S_3 hollow microspheres composed of nanofibers and nanosheets and their photocatalytic activity, *Langmuir* 27 (2011) 5534–5541.
- [68] J. Ning, K. Men, G. Xiao, L. Zhao, L. Wang, B. Liu, B. Zou, Synthesis, optical properties and growth process of In_2S_3 nanoparticles, *J. Colloid Interface Sci.* 347 (2010) 172–176.
- [69] Y.H. Kim, J.H. Lee, D.W. Shin, S.M. Park, J.S. Moon, J.G. Nam, J.B. Yoo, Synthesis of shape-controlled beta- In_2S_3 nanotubes through oriented attachment of nanoparticles, *Chem. Commun.* 46 (2010) 2292–2294.
- [70] J.N. Coleman, M. Lotya, A. O'Neill, S.D. Bergin, P.J. King, U. Khan, K. Young, A. Gaucher, S. De, R.J. Smith, I.V. Shvets, S.K. Arora, G. Stanton, H.Y. Kim, K. Lee, G.T. Kim, G.S. Duesberg, T. Hallam, J.J. Boland, J.J. Wang, J.F. Donegan, J.C. Grunlan, G. Moriarty, A. Shmeliov, R.J. Nicholls, J.M. Perkins, E.M. Griesevon, K. Theuwissen, D.W. McComb, P.D. Nellist, V. Nicolosi, Two-dimensional nanosheets produced by liquid exfoliation of layered materials, *Science* 331 (2011) 568–571.
- [71] B. Xue, F. Xu, B. Wang, A. Dong, Shape-controlled synthesis of β - In_2S_3 nanocrystals and their lithium storage properties, *CrystEngComm* 18 (2016) 250–256.
- [72] M.J. Bierman, S. Jin, Potential applications of hierarchical branching nanowires in solar energy conversion, *Energy Environ. Sci.* 2 (2009) 1050.
- [73] W. Yue, F. Wei, C. He, D. Wu, N. Tang, Q. Qiao, l-Cysteine assisted-synthesis of 3D In_2S_3 for 3D CuInS_2 and its application in hybrid solar cells, *RSC Adv.* 7 (2017) 37578–37587.
- [74] W. Du, J. Zhu, S. Li, X. Qian, Ultrathin β - In_2S_3 nanobelts: shape-controlled synthesis and optical and photocatalytic properties, *Cryst. Growth Des.* 8 (2008) 2130–2136.
- [75] S. Yang, C.Y. Xu, B.Y. Zhang, L. Yang, S.P. Hu, L. Zhen, Ca(II) doped beta- In_2S_3 hierarchical structures for photocatalytic hydrogen generation and organic dye degradation under visible light irradiation, *J. Colloid Interface Sci.* 491 (2017) 230–237.
- [76] G.A.M. Hutton, B.C.M. Martindale, E. Reisner, Carbon dots as photosensitisers for solar-driven catalysis, *Chem. Soc. Rev.* 46 (2017) 6111–6123.
- [77] N. Revaprasadu, M.A. Malik, J. Carstens, P.O. Brien, Novel single-molecule precursor routes for the direct synthesis of InS and InSe quantum dots, *J. Mater. Chem.* 9 (1999) 2885–2888.
- [78] C. Kaito, Y. Saito, K. Fujita, Studies on the structure and morphology of ultrafine particles of metallic sulfides, *J. Cryst. Growth* 94 (1989) 967–977.
- [79] W.T. Kim, C.D. Kim, Optical energy gaps of β - In_2S_3 thin films grown by spray pyrolysis, *J. Appl. Phys.* 60 (1986) 2631–2633.
- [80] M. Bedir, M. Oztas, D. Korkmaz, Y. Ozdemir, Influence of preparation conditions on the dispersion parameters of sprayed In_2S_3 films, *Arabian J. Sci. Eng.* 39 (2013) 503–509.
- [81] P.F. Herrasti, E., Characterization of In_2S_3 films obtained by slurry painting, *J. Mater. Sci.* 25 (1990) 3535–3540.
- [82] I.V. Bodnar, V.A. Polubok, V.F. Gremenok, V.Y. Rud', Y.V. Rud', Schottky barriers based on n- In_2S_3 films obtained by laser-induced evaporation, *Semicond.* 41 (2007) 47–51.
- [83] S. Avivi, O. Palchik, V. Palchik, M.A. Slifkin, M.A. Weiss, A. Gedanken, Sonochemical synthesis of nanophase indium sulfide, *Chem. Mater.* 13 (2003) 2195–2200.
- [84] M.A. Mughal, R. Engelken, R. Sharma, Progress in indium (III) sulfide (In_2S_3) buffer layer deposition techniques for CIS, CIGS, and CdTe-based thin film solar cells, *Sol. Energy* 120 (2015) 131–146.

- [85] N. Barreau, S. Marsillac, J.C. Bernede, T. Ben Nasrallah, S. Belgacem, Optical properties of wide band gap indium sulphide thin films obtained by physical vapor deposition, *Phys. Status Solidi A* 184 (2001) 179–186.
- [86] F. Biegger, F. Jungwirth, M.S. Seifner, C. Rameshan, S. Barth, Aerosol-assisted CVD of thioether-functionalised indium aminoalkoxides, *Monatsh. Chem.* 148 (2017) 1385–1392.
- [87] M. Afzaal, M.A. Malik, P. O'Brien, Indium sulfide nanorods from single-source precursor, *Chem. Commun.* 3 (2004) 334–335.
- [88] M.J. Zhang, L.L. Tian, S. Li, L.P. Lin, F. Pan, Mesoporous and carbon hybrid structures from layered molecular precursors for Li-ion battery application: the case of beta-In₂S₃, *Chem. Commun.* 52 (2016) 4788–4791.
- [89] Y.X. Yujie Xiong, Guoan Du, Xiaobo Tian, A solvent-reduction and surface-modification technique to morphology control of tetragonal In₂S₃ nanocrystals, *J. Mater. Chem.* 12 (2001) 98–102.
- [90] C.D. Lokhande, A. Ennaoui, P.S. Patil, M. Giersig, K. Diesner, M. Muller, H. Tributsch, Chemical bath deposition of indium sulphide thin films: preparation and characterization, *Thin Solid Films* 340 (1999) 18–23.
- [91] R.S. Mane, C.D. Lokhande, Chemical deposition method for metal chalcogenide thin films, *Mater. Chem. Phys.* 65 (2000) 1–31.
- [92] Y. Xiong, Y. Xie, G. Du, X. Tian, Y. Qian, A novel in situ oxidation–Sulfidation growth route via self-purification process to β-In₂S₃ dendrites, *J. Solid State Chem.* 166 (2002) 336–340.
- [93] S.D. Naik, T.C. Jagadale, S.K. Apte, R.S. Sonawane, M.V. Kulkarni, S.I. Patil, S.B. Ogale, B.B. Kale, Rapid phase-controlled microwave synthesis of nanostructured hierarchical tetragonal and cubic β-In₂S₃ dandelion flowers, *Chem. Phys. Lett.* 452 (2008) 301–305.
- [94] J. Jiang, J. Zou, Y. Zhang, J. Ma, H. Jiang, Q. Wan, A novel synthesis and characterization of 3D chrysanthemum-like β-In₂S₃ by surfactantfree hydrothermal method, *Mater. Lett.* 79 (2012) 132–135.
- [95] H. Zhu, X. Wang, W. Yang, F. Yang, X. Yang, Indium sulfide microflowers: fabrication and optical properties, *Mater. Res. Bull.* 44 (2009) 2033–2039.
- [96] F. Ye, C. Wang, G. Du, X. Chen, Y. Zhong, J.Z. Jiang, Large-scale synthesis of In₂S₃ nanosheets and their rechargeable lithium-ion battery, *J. Mater. Chem.* 21 (2011) 17063.
- [97] Z. Fang, X. Huang, Y. Wang, W. Feng, Y. Zhang, S. Weng, X. Fu, P. Liu, Dual-defective strategy directing in situ assembly for effective interfacial contacts in MoS₂ cocatalyst/In₂S₃ light harvester layered photocatalysts, *J. Mater. Chem. A* 4 (2016) 13980–13988.
- [98] A. Datta, D. Mukherjee, S. Witanachchi, P. Mukherjee, On-the-surface photoconductive response of pelletized thin In₂S₃ nanosheets, *Mater. Res. Bull.* 55 (2014) 176–181.
- [99] B. Pejova, I. Bineva, Sonochemically synthesized 3D assemblies of close-packed In₂S₃ quantum dots: structure, size dependent optical and electrical properties, *J. Phys. Chem. C* 117 (2013) 7303–7314.
- [100] R. Wu, Y. Xu, R. Xu, Y. Huang, B. Zhang, Ultrathin-nanosheet-based 3D hierarchical porous In₂S₃ microspheres: chemical transformation synthesis, characterization, and enhanced photocatalytic and photoelectrochemical property, *J. Mater. Chem. A* 3 (2015) 1930–1934.
- [101] L. Jiang, X. Yuan, Y. Pan, J. Liang, G. Zeng, Z. Wu, H. Wang, Doping of graphitic carbon nitride for photocatalysis: a review, *Appl. Catal. B* 217 (2017) 388–406.
- [102] Z. Yu, X.Q. Chen, X. Kang, Y. Xie, H. Zhu, S. Wang, S. Ullah, H. Ma, L. Wang, G. Liu, X. Ma, Noninvasively modifying band structures of wide-bandgap metal oxides to boost photocatalytic activity, *Adv. Mater.* 30 (2018) 1706259.
- [103] Y. Dong, J. Choi, H.K. Jeong, D.H. Son, Hot electrons generated from doped quantum dots via upconversion of excitons to hot charge carriers for enhanced photocatalysis, *J. Am. Chem. Soc.* 137 (2015) 5549–5554.
- [104] I. Showin, S. Samireddi, Y.C. Chang, R. Putikam, P.H. Chang, A. Sabbah, F.Y. Fu, W.F. Chen, C.I. Wu, T.Y. Yu, P.W. Chung, M.C. Lin, L.C. Chen, K.H. Chen, Carbon-doped SnS₂ nanostructure with a high-efficiency solar fuel catalyst under visible light, *Nat. Commun.* 9 (2018) 169.
- [105] F. Lei, L. Zhang, Y. Sun, L. Liang, K. Liu, J. Xu, Q. Zhang, B. Pan, Y. Luo, Y. Xie, Atomic-layer-Confined doping for atomic-level insights into visible-light water splitting, *Angew. Chem. Int. Ed. Eng.* 54 (2015) 9266–9270.
- [106] I.A. de Castro, R.S. Datta, J.Z. Ou, A. Castellanosgomez, S. Sriram, T. Daeneke, K. Kalantarzadeh, Molybdenum oxides-from fundamentals to functionality, *Adv. Mater.* 29 (2017) 1701619.
- [107] Dattatri K. Nagesha, Xiaorong Liang, Arif A. Mamedov, Gordon Gainer, Margaret A. Eastman, Michael Giersig, Jin Joo Song, A. Tong Ni, Nicholas A. Kotov, In₂S₃ nanocolloids with excitonic emission: In₂S₃ vs CdS comparative study of optical and structural characteristics, *J. Phys. Chem. B* 105 (2001) 7490–7498.
- [108] W.T. Kim, W.S. Lee, C.S. Chung, C.D. Kim, Optical properties of In₂S₃:Co²⁺ single crystals, *J. Appl. Phys.* 63 (1988) 5472–5475.
- [109] N. Kamoun, S. Belgacem, M. Amlouk, R. Bennaceur, J. Bonnet, F. Touhari, M. Nouaoura, L. Lassabatere, Structure, surface composition, and electronic properties of β-In₂S₃ and β-In_{2-x}Al_xS₃, *J. Appl. Phys.* 89 (2001) 2766–2771.
- [110] M. Hasan Zadeh Maha, M.M. Bagheri-Mohagheghi, H. Azimi-Juybari, Tin doped β-In₂S₃ thin films prepared by spray pyrolysis: correlation between structural, electrical, optical, thermoelectric and photoconductive properties, *Thin Solid Films* 536 (2013) 57–62.
- [111] A. Datta, D. Ganguli, S. Chaudhuri, Hydrothermal synthesis of Co-doped In₂S₃ micropompons and their physical properties, *J. Mater. Res.* 23 (2011) 917–923.
- [112] L.-Y. Lin, J.-L. Yu, S.-Y. Cheng, P.-M. Lu, Influence of Ag and Sn incorporation in In₂S₃ thin films, *Chin. Phys. B* 24 (2015) 078103.
- [113] Z. Li, P. Wang, T. Yang, H. Yu, B. Xiao, M. Zhang, Enhanced luminescence with fast nanosecond lifetime in In₂S₃:Tb³⁺ nanophosphors, *J. Phys. Chem. C* 119 (2015) 27688–27694.
- [114] R.F. McCarthy, M.S. Weimer, R.T. Haasch, R.D. Schaller, A.S. Hock, A.B.F. Martinson, V_xIn_(2-x)S₃ intermediate band absorbers deposited by atomic layer deposition, *Chem. Mater.* 28 (2016) 2033–2040.
- [115] Z.F. Li, M.Y. Chuai, Q. Zhao, T.Y. Yang, H. Yu, M.Z. Zhang, Synthesis and investigations of In₂S₃:Ho³⁺ quantum dots on doping induced changes, *CrystEngComm* 19 (2017) 853–859.
- [116] B. Yao, P. Wang, S. Wang, M. Zhang, Ce doping influence on the magnetic phase transition in In₂S₃:Ce nanoparticles, *CrystEngComm* 16 (2014) 2584–2588.
- [117] Z. Li, T. Yang, Q. Zhao, M. Zhang, Tunable photoluminescence and room temperature ferromagnetism of In₂S₃:Dy⁽³⁺⁾,Tb⁽³⁺⁾ nanoparticles, *Phys. Chem. Chem. Phys.* 19 (2017) 16758–16764.
- [118] L. Wang, L. Xia, Y. Wu, Y. Tian, Zr-doped β-In₂S₃ ultrathin nanoflakes as photoanodes: enhanced visible-light-driven photoelectrochemical water splitting, *ACS Sustain. Chem. Eng.* 4 (2016) 2606–2614.
- [119] R. Lucena, J.C. Conesa, I. Aguilera, P. Palacios, P. Wahnón, V-substituted In₂S₃: an intermediate band material with photocatalytic activity in the whole visible light range, *J. Mater. Chem. A* 2 (2014) 8236–8245.
- [120] W.-T. Liu, B.-H. Wu, Y.-T. Lai, N.-H. Tai, T.-P. Perng, L.-J. Chen, Enhancement of water splitting by controlling the amount of vacancies with varying vacuum level in the synthesis system of SnO_{2-x}/In₂O_{3-y} heterostructure as photocatalyst, *Nano Energy* 47 (2018) 18–25.
- [121] D. Ma, J.-W. Shi, Y. Zou, Z. Fan, X. Ji, C. Niu, L. Wang, Rational design of CdS@ZnO core-shell structure via atomic layer deposition for drastically enhanced photocatalytic H₂ evolution with excellent photostability, *Nano Energy* 39 (2017) 183–191.
- [122] Z. Zhang, P. Chen, X. Duan, K. Zang, J. Luo, X. Duan, Robust epitaxial growth of two-dimensional heterostructures, multiheterostructures, and superlattices, *Science* 357 (2017) 788–792.
- [123] M.Q. Yang, B. Weng, Y.J. Xu, Improving the visible light photoactivity of In₂S₃-graphene nanocomposite via a simple surface charge modification approach, *Langmuir* 29 (2013) 10549–10558.
- [124] S. Kamimura, N. Beppu, Y. Sasaki, T. Tsubota, T. Ohno, Platinum and indium sulfide-modified Cu₃BiS₃ photocathode for photoelectrochemical hydrogen evolution, *J. Mater. Chem. A* 5 (2017) 10450–10456.
- [125] W. Han, L. Yi, N. Zhao, A. Tang, M. Gao, Z. Tang, Synthesis and shape-tailoring of copper sulfide/indium sulfide-based nanocrystals, *J. Am. Chem. Soc.* 130 (2008) 13152–13161.
- [126] X. Zhang, C. Shao, X. Li, N. Lu, K. Wang, F. Miao, Y. Liu, In₂S₃/carbon nanofibers/Au ternary synergetic system: hierarchical assembly and enhanced visible-light photocatalytic activity, *J. Hazard. Mater.* 283 (2015) 599–607.
- [127] H. Min Lim, S.K. Batabyal, S.S. Pramana, L.H. Wong, S. Magdassi, S.G. Mhaisalkar, Chemical welding of binary nanoparticles: room temperature sintering of CuSe and In₂S₃ nanoparticles for solution-processed CuIn₃(x)Se_(1-x) solar cells, *Chem. Commun.* 49 (2013) 5351–5353.
- [128] Y. Li, S. Luo, Z. Wei, D. Meng, M. Ding, C. Liu, Electrodeposition technique-dependent photoelectrochemical and photocatalytic properties of an In₂S₃/TiO₂ nanotube array, *Phys. Chem. Chem. Phys.* 16 (2014) 4361–4368.
- [129] Y. Wang, Q. Zhang, Y. Li, H. Wang, Preparation of AgInS₂ quantum dot/In₂S₃ co-sensitized photoelectrodes by a facile aqueous-phase synthesis route and their photovoltaic performance, *Nanoscale* 7 (2015) 6185–6192.
- [130] Z. Shen, G. Chen, Q. Wang, Y. Yu, C. Zhou, Y. Wang, Sonochemistry synthesis and enhanced photocatalytic H₂-production activity of nanocrystals embedded in CdS/ZnS/In₂S₃ microspheres, *Nanoscale* 4 (2012) 2010–2017.
- [131] T. Yan, J. Tian, W. Guan, Z. Qiao, W. Li, J. You, B. Huang, Ultra-low loading of Ag₃PO₄ on hierarchical In₂S₃ microspheres to improve the photocatalytic performance: the cocatalytic effect of Ag and Ag₃PO₄, *Appl. Catal. B* 202 (2017) 84–94.
- [132] X.Y. Yu, X.W. David Lou, Mixed metal sulfides for electrochemical energy storage and conversion, *Adv. Energy Mater.* 8 (2018) 1701592.
- [133] Y. Zhang, Q. Zhou, J. Zhu, Q. Yan, S.X. Dou, W. Sun, Nanostructured metal chalcogenides for energy storage and electrocatalysis, *Adv. Funct. Mater.* 27 (2017) 1702317.
- [134] Y. Chen, G. Tian, Q. Guo, R. Li, T. Han, H. Fu, One-step synthesis of a hierarchical Bi₂S₃ nanoflower/In₂S₃ nanosheet composite with efficient visible-light photocatalytic activity, *CrystEngComm* 17 (2015) 8720–8727.
- [135] B. Liu, X. Hu, X. Li, Y. Li, C. Chen, K.H. Lam, Preparation of ZnS@In₂S₃ Core@shell composite for enhanced photocatalytic degradation of gaseous o-Dichlorobenzene under visible light, *Sci. Rep* 7 (2017) 16396.
- [136] C. Moreno, M. Vilas-Varela, B. Kretz, A. Garcia-Lekue, M.V. Costache, M. Paradinas, M. Paniguel, G. Ceballos, S.O. Valenzuela, D. Pena, A. Mugarza, Bottom-up synthesis of multifunctional nanoporous graphene, *Science* 360 (2018) 199–203.
- [137] M.-Q. Yang, B. Wang, Y.-J. Xu, Synthesis of In₂S₃-CNT nanocomposites for selective reduction under visible light, *J. Mater. Chem. A* 2 (2014) 1710–1720.
- [138] X. An, J.C. Yu, F. Wang, C. Li, Y. Li, One-pot synthesis of In₂S₃ nanosheets/graphene composites with enhanced visible-light photocatalytic activity, *Appl. Catal. B* 129 (2013) 80–88.

- [139] S.Q. Guo, X. Chen, F.Z. Hu, Q.C. Zhang, L. Liu, Ultralong In_2S_3 nanotubes on graphene substrate with enhanced electrocatalytic activity, *ACS Appl. Mater. Interfaces* 7 (2015) 20164–20169.
- [140] X. Yang, C.Y. Chan, H.T. Xue, J. Xu, Y.-B. Tang, Q. Wang, T.L. Wong, C.-S. Lee, One-pot synthesis of graphene/ In_2S_3 nanoparticle composites for stable rechargeable lithium ion battery, *CrystEngComm* 15 (2013) 6578.
- [141] X. Wang, J.Y. Hwang, S.T. Myung, J. Hassoun, Y.K. Sun, Graphene decorated by indium sulfide nanoparticles as high-performance anode for sodium-ion batteries, *ACS Appl. Mater. Interfaces* 9 (2017) 23723–23730.
- [142] S.B. Kokane, R. Sasikala, D.M. Phase, S.D. Sartale, In_2S_3 nanoparticles dispersed on $\text{g-C}_3\text{N}_4$ nanosheets: role of heterojunctions in photoinduced charge transfer and photoelectrochemical and photocatalytic performance, *J. Mater. Sci.* 52 (2017) 7077–7090.
- [143] C. Xing, Z. Wu, D. Jiang, M. Chen, Hydrothermal synthesis of $\text{In}_2\text{S}_3/\text{g-C}_3\text{N}_4$ heterojunctions with enhanced photocatalytic activity, *J. Colloid Interface Sci.* 433 (2014) 9–15.
- [144] G. Gunawan, W. Septina, S. Ikeda, T. Harada, T. Minegishi, K. Domen, M. Matsumura, Platinum and indium sulfide-modified CuInS_2 as efficient photocathodes for photoelectrochemical water splitting, *Chem. Commun.* 50 (2014) 8941–8943.
- [145] F. Wang, W. Li, S. Gu, H. Li, H. Zhou, X. Wu, Novel $\text{In}_2\text{S}_3/\text{ZnWO}_4$ heterojunction photocatalysts: facile synthesis and high-efficiency visible-light-driven photocatalytic activity, *RSC Adv.* 5 (2015) 89940–89950.
- [146] H. Wang, X. Yuan, Y. Wu, G. Zeng, H. Dong, X. Chen, L. Leng, Z. Wu, L. Peng, In situ synthesis of $\text{In}_2\text{S}_3@ \text{MIL-125}(\text{Ti})$ core-shell microparticle for the removal of tetracycline from wastewater by integrated adsorption and visible-light-driven photocatalysis, *Appl. Catal. B* 186 (2016) 19–29.
- [147] L. Jiang, X. Yuan, G. Zeng, Z. Wu, J. Liang, X. Chen, L. Leng, H. Wang, H. Wang, Metal-free efficient photocatalyst for stable visible-light photocatalytic degradation of refractory pollutant, *Appl. Catal. B* 221 (2017) 715–725.
- [148] L. Jiang, X. Yuan, G. Zeng, J. Liang, X. Chen, H. Yu, H. Wang, Z. Wu, J. Zhang, T. Xiong, In-situ synthesis of direct solid-state dual Z-scheme $\text{WO}_3/\text{g-C}_3\text{N}_4/\text{Bi}_2\text{O}_3$ photocatalyst for the degradation of refractory pollutant, *Appl. Catal. B* 227 (2018) 376–385.
- [149] H. Heng, Q. Gan, P. Meng, X. Liu, The visible-light-driven type III heterojunction $\text{H}_3\text{PW}_{12}\text{O}_{40}/\text{TiO}_2\text{-In}_2\text{S}_3$: a photocatalysis composite with enhanced photocatalytic activity, *J. Alloys Compd.* 696 (2017) 51–59.
- [150] J. Xiao, Q. Han, Y. Xie, J. Yang, Q. Su, Y. Chen, H. Cao, Is C_3N_4 chemically stable toward reactive oxygen species in sunlight-driven water treatment? *Environ. Sci. Technol.* 51 (2017) 13380–13387.
- [151] Y. Liu, M. Zhang, C.-H. Tung, Y. Wang, TiO_2 photocatalytic cyclization reactions for the syntheses of Aryltetralones, *ACS Catal.* 6 (2016) 8389–8394.
- [152] F. Zhang, X. Li, Q. Zhao, A. Chen, Facile and controllable modification of 3D In_2O_3 microflowers with In_2S_3 nanoflakes for efficient photocatalytic degradation of gaseous ortho-dichlorobenzene, *J. Phys. Chem. C* 120 (2016) 19113–19123.
- [153] J. Chen, W. Liu, W. Gao, Tuning photocatalytic activity of In_2S_3 broadband spectrum photocatalyst based on morphology, *Appl. Surf. Sci.* 368 (2016) 288–297.
- [154] T. Yan, T. Wu, Y. Zhang, M. Sun, X. Wang, Q. Wei, B. Du, Fabrication of $\text{In}_2\text{S}_3/\text{Zn}_2\text{GeO}_4$ composite photocatalyst for degradation of acetaminophen under visible light, *J. Colloid Interface Sci.* 506 (2017) 197–206.
- [155] Y. Xiao, G. Tian, Y. Chen, X. Zhang, H. Fu, H. Fu, Exceptional visible-light photoelectrocatalytic activity of $\text{In}_2\text{O}_3/\text{In}_2\text{S}_3/\text{CdS}$ ternary stereoscopic porous heterostructure film for the degradation of persistent 4-fluoro-3-methylphenol, *Appl. Catal. B* 225 (2018) 477–486.
- [156] J. Chen, W. Liu, Z. Song, H. Wang, Y. Xie, Photocatalytic degradation of β -O-4 lignin model compound by In_2S_3 nanoparticles under visible light irradiation, *Bioenergy Res.* 11 (2017) 166–173.
- [157] H. Heng, Q. Gan, P. Meng, X. Liu, The visible-light-driven type III heterojunction $\text{H}_3\text{PW}_{12}\text{O}_{40}/\text{TiO}_2\text{-In}_2\text{S}_3$: a photocatalysis composite with enhanced photocatalytic activity, *J. Alloys Compd.* 696 (2017) 51–59.
- [158] Z. Zhang, Y. Tang, C. Liu, L. Wan, Fabrication of In_2S_3 nanoparticle decorated TiO_2 nanotube arrays by successive ionic layer adsorption and reaction technique and their photocatalytic application, *J. Nanosci. Nanotechnol.* 14 (2014) 4170–4177.
- [159] J. Zhou, G. Tian, Y. Chen, Y. Shi, C. Tian, K. Pan, H. Fu, Growth rate controlled synthesis of hierarchical $\text{Bi}_2\text{S}_3/\text{In}_2\text{S}_3$ core/shell microspheres with enhanced photocatalytic activity, *Sci. Rep.* 4 (2014) 4027.
- [160] X. Yuan, L. Jiang, J. Liang, Y. Pan, J. Zhang, H. Wang, L. Leng, Z. Wu, R. Guan, G. Zeng, In-situ synthesis of 3D microsphere-like $\text{In}_2\text{S}_3/\text{InVO}_4$ heterojunction with efficient photocatalytic activity for tetracycline degradation under visible light irradiation, *Chem. Eng. J.* 356 (2019) 371–381.
- [161] C. Wei, W. Guo, J. Yang, H. Fan, J. Zhang, W. Zheng, Facile solvothermal synthesis of 3D flowerlike $\beta\text{-In}_2\text{S}_3$ microspheres and their photocatalytic activity performance, *RSC Adv.* 4 (2014) 50456–50463.
- [162] W. Qiu, M. Xu, X. Yang, F. Chen, Y. Nan, J. Zhang, H. Iwai, H. Chen, Biomolecule-assisted hydrothermal synthesis of In_2S_3 porous films and enhanced photocatalytic properties, *J. Mater. Chem.* 21 (2011) 13327.
- [163] J.B. Chen Wei, Alan G. Joly, Shaopeng Wang, Fuhai Su, Li Guohua, Full-color emission from In_2S_3 and $\text{In}_2\text{S}_3:\text{Eu}^{3+}$ nanoparticles, *J. Cheminf.* 35 (2004) 11927–11934.
- [164] M.S. Shujuan Zhuo, Shuit-Tong Lee, Upconversion and downconversion fluorescent graphene quantum dots ultrasonic preparation and photocatalysis, *ACS Nano* 6 (2012) 1059–1064.
- [165] X. Li, H. Ren, Z. Zou, J. Sun, J. Wang, Z. Liu, Energy gap engineering of polymeric carbon nitride nanosheets for matching with $\text{NaYF}_4:\text{Yb,Tm}$: enhanced visible-near infrared photocatalytic activity, *Chem. Commun.* 52 (2016) 453–456.
- [166] A.D. Liyanage, S.D. Perera, K. Tan, Y. Chabal, K.J. Balkus, Synthesis, Characterization, and Photocatalytic Activity of Y-Doped CeO_2 Nanorods, *ACS Catal.* 4 (2014) 577–584.
- [167] C. Tapia, S.P. Berglund, D. Friedrich, T. Dittrich, P. Bogdanoff, Y. Liu, S. Levchenko, T. Unold, J.C. Conesa, A.L. De Lacey, M. Pita, S. Fiechter, Synthesis and characterization of V-Doped $\beta\text{-In}_2\text{S}_3$ thin films on FTO substrates, *J. Phys. Chem. C* 120 (2016) 28753–28761.
- [168] R.P. Schwarzenbach, B.I. Escher, K. Fenner, T.B. Hofstetter, C.A. Johnson, U. von Gunten, B. Wehrli, The challenge of micropollutants in aquatic systems, *Science* 313 (2006) 1072–1077.
- [169] H. Ren, P. Koshy, W.F. Chen, S. Qi, C.C. Sorrell, Photocatalytic materials and technologies for air purification, *J. Hazard. Mater.* 325 (2017) 340–366.
- [170] WHO, Preventing Disease Through Healthy Environments: a Global Assessment of the Burden of Disease From Environmental Risks, World Health Organization (2016).
- [171] S. Cao, J. Low, J. Yu, M. Jaroniec, Polymeric photocatalysts based on graphitic carbon nitride, *Adv. Mater.* 27 (2015) 2150–2176.
- [172] P. Gao, A.R. Li, M.H. Tai, Z.Y. Liu, D.D. Sun, A hierarchical nanostructured carbon nanofiber- In_2S_3 photocatalyst with high photodegradation and disinfection abilities under visible light, *Chem. Asian J.* 9 (2014) 1663–1670.
- [173] D. Ma, J.W. Shi, Y. Zou, Z. Fan, J. Shi, L. Cheng, D. Sun, Z. Wang, C. Niu, Multiple carrier-transfer pathways in a flower-like $\text{In}_2\text{S}_3/\text{CdIn}_2\text{S}_4/\text{In}_2\text{O}_3$ ternary heterostructure for enhanced photocatalytic hydrogen production, *Nanoscale* 10 (2018) 7860.
- [174] N. Choudhary, M.A. Islam, J.H. Kim, T.-J. Ko, A. Schropp, L. Hurtado, D. Weitzman, L. Zhai, Y. Jung, Two-dimensional transition metal dichalcogenide hybrid materials for energy applications, *Nano Today* 19 (2018) 16–40.
- [175] B. Ma, M. Yue, P. Zhang, S. Li, R. Cong, W. Gao, T. Yang, Tetragonal $\beta\text{-In}_2\text{S}_3$: partial ordering of In^{3+} vacancy and visible-light photocatalytic activities in both water and nitrate reduction, *Catal. Commun.* 88 (2017) 18–21.
- [176] F. Wang, Z. Jin, Y. Jiang, E.H.G. Backus, M. Bonn, S.N. Lou, D. Turchinovich, R. Amal, Probing the charge separation process on $\text{In}_2\text{S}_3/\text{Pt-TiO}_2$ nanocomposites for boosted visible-light photocatalytic hydrogen production, *Appl. Catal. B* 198 (2016) 25–31.
- [177] X. Yang, J. Xu, T. Wong, Q. Yang, C.-S. Lee, Synthesis of $\text{In}_2\text{O}_3\text{-In}_2\text{S}_3$ core-shell nanorods with inverted type-I structure for photocatalytic H_2 generation, *Phys. Chem. Chem. Phys.* 15 (2013) 12688.
- [178] J. Liu, T. Ding, Z. Li, J. Zhao, S. Li, J. Liu, Photocatalytic hydrogen production over $\text{In}_2\text{S}_3\text{-Pt-Na}_2\text{Ti}_3\text{O}_7$ nanotube films under visible light irradiation, *Ceram. Int.* 39 (2013) 8059–8063.
- [179] B. Chai, T. Peng, P. Zeng, J. Mao, Synthesis of fluorinated In_2S_3 decorated with TiO_2 nanoparticles for efficient photocatalytic hydrogen production under visible light, *J. Mater. Chem.* 21 (2011) 14587.
- [180] Y. Li, G. Chen, C. Zhou, J. Sun, A simple template-free synthesis of nanoporous $\text{ZnS-In}_2\text{S}_3\text{-Ag}_2\text{S}$ solid solutions for highly efficient photocatalytic H_2 evolution under visible light, *Chem. Commun.* (2009) 2020–2022.
- [181] Y. Li, G. Chen, Q. Wang, X. Wang, A. Zhou, Z. Shen, Hierarchical $\text{ZnS-In}_2\text{S}_3\text{-CuS}$ nanospheres with nanoporous structure: facile synthesis, growth mechanism, and excellent photocatalytic activity, *Adv. Funct. Mater.* 20 (2010) 3390–3398.
- [182] W. Jiang, Y. Liu, R. Zong, Z. Li, W. Yao, Y. Zhu, Photocatalytic hydrogen generation on bifunctional ternary heterostructured $\text{In}_2\text{S}_3/\text{MoS}_2/\text{CdS}$ composites with high activity and stability under visible light irradiation, *J. Mater. Chem. A* 3 (2015) 18406–18412.
- [183] Q. Zhang, M. Luo, Y.P. Sun, Y. Liu, A. Cao, Efficient Z-scheme photocatalyst from simultaneous decoration of In_2S_3 nanosheets and WO_3 nanorods on graphene sheets, *Nanotechnology* 27 (2016) 285602.
- [184] L. Zhang, W. Zhang, H. Yang, W. Fu, M. Li, H. Zhao, J. Ma, Hydrothermal synthesis and photoelectrochemical properties of In_2S_3 thin films with a wedgelike structure, *Appl. Surf. Sci.* 258 (2012) 9018–9024.
- [185] M.A. Ehsan, T.A. Peiris, K.G. Wijayantha, M.M. Olmstead, Z. Arifin, M. Mazhar, K.M. Lo, V. McKee, Development of molecular precursors for deposition of indium sulphide thin film electrodes for photoelectrochemical applications, *Dalton Trans.* 42 (2013) 10919–10928.
- [186] F.-Y. Su, W.-D. Zhang, Y.-Y. Liu, R.-H. Huang, Y.-X. Yu, Growth of porous In_2S_3 films and their photoelectrochemical properties, *J. Solid State Electrochem.* 19 (2015) 2321–2330.
- [187] J.S. Yang, J.J. Wu, Toward eco-friendly and highly efficient solar water splitting using $\text{In}_2\text{S}_3/\text{Anatase/Rutile TiO}_2$ dual-staggered-Heterojunction nanodendrite array photoanode, *ACS Appl. Mater. Interfaces* 10 (2018) 3714–3722.
- [188] F. Liu, Y. Jiang, J. Yang, M. Hao, Z. Tong, L. Jiang, Z. Wu, MoS_2 nanodot decorated In_2S_3 nanoplates: a novel heterojunction with enhanced photoelectrochemical performance, *Chem. Commun.* 52 (2016) 1867–1870.
- [189] W. Gunawan, T. Septina, Y. Harada, S. Ikeda Nose, Investigation of the electric structures of heterointerfaces in Pt and In_2S_3 modified CuInS_2 photocathodes used for sunlight-induced hydrogen evolution, *ACS Appl. Mater. Interfaces* 7 (2015) 16086–16092.
- [190] X. Li, Z. Wang, Z. Zhang, L. Chen, J. Cheng, W. Ni, B. Wang, E. Xie, Light illuminated $\alpha\text{-Fe}_2\text{O}_3/\text{Pt}$ nanoparticles as water activation agent for photoelectrochemical water splitting, *Sci. Rep.* 5 (2015) 9130.

- [191] C.A. Caputo, L. Wang, R. Beranek, E. Reisner, Carbon nitride-TiO₂ hybrid modified with hydrogenase for visible light driven hydrogen production, *Chem. Sci.* 6 (2015) 5690–5694.
- [192] C. Tapia, S. Zacarias, I.A.C. Pereira, J.C. Conesa, M. Pita, A.L. De Lacey, In situ determination of photobioproduction of H₂ by In₂S₃-[NiFeSe] hydrogenase from *Desulfovibrio vulgaris hildenborough* using only visible light, *ACS Catal.* 6 (2016) 5691–5698.
- [193] C. Tapia, S. Shleev, J.C. Conesa, A.L. De Lacey, M. Pita, Laccase-catalyzed bioelectrochemical oxidation of water assisted with visible light, *ACS Catal.* 7 (2017) 4881–4889.
- [194] Z. Jiang, B. Wang, J.C. Yu, J. Wang, T. An, H. Zhao, H. Li, S. Yuan, P.K. Wong, AgInS₂/In₂S₃ heterostructure sensitization of *Escherichia coli* for sustainable hydrogen production, *Nano Energy* 46 (2018) 234–240.
- [195] I. Akkerman, M. Janssen, J. Rocha, R.H. Wijffels, Photobiological hydrogen production: photochemical efficiency and bioreactor design, *Int. J. Hydrogen Energy* 27 (2002) 1195–1208.
- [196] H. Li, Y. Gao, Y. Zhou, F. Fan, Q. Han, Q. Xu, X. Wang, M. Xiao, C. Li, Z. Zou, Construction and nanoscale detection of interfacial charge transfer of elegant Z-Scheme WO₃/Au/In₂S₃ nanowire arrays, *Nano Lett.* 16 (2016) 5547–5552.
- [197] N. Naghavi, S. Spiering, M. Powalla, B. Cavana, D. Lincot, High-efficiency copper indium gallium diselenide (CIGS) solar cells with indium sulfide buffer layers deposited by atomic layer chemical vapor deposition (ALCVD), *Prog. Photovoltaics* 11 (2003) 437–443.
- [198] J. Kim, H. Hiroi, T.K. Todorov, O. Gunawan, M. Kuwahara, T. Gokmen, D. Nair, M. Hopstaken, B. Shin, Y.S. Lee, W. Wang, H. Sugimoto, D.B. Mitzi, High efficiency Cu₂ZnSn(S,Se)₄ solar cells by applying a double In₂S₃/CdS emitter, *Adv. Mater.* 26 (2014) 7427–7431.
- [199] M.A. Basit, M.A. Abbas, E.S. Jung, Y.M. Park, J.H. Bang, T.J. Park, Strategic PbS quantum dot-based multilayered photoanodes for high efficiency quantum dot-sensitized solar cells, *Electrochim. Acta* 211 (2016) 644–651.
- [200] J. Duan, Q. Tang, B. He, L. Yu, Efficient In₂S₃ quantum dot-sensitized solar cells: a promising power conversion efficiency of 1.30%, *Electrochim. Acta* 139 (2014) 381–385.
- [201] S. Siol, T.P. Dhakal, G.S. Gudavalli, P.P. Rajbhandari, C. DeHart, L.L. Baranowski, A. Zakutayev, Combinatorial reactive sputtering of In₂S₃ as an alternative contact layer for thin film solar cells, *ACS Appl. Mater. Interfaces* 8 (2016) 14004–14011.
- [202] F. Jiang, C. Ozaki, T. Gunawan, Z. Harada, T. Tang, Y. Minemoto, S. Nose, Ikeda, Effect of indium doping on surface optoelectrical properties of Cu₂ZnSnS₄ photoabsorber and Interfacial/Photovoltaic performance of cadmium free In₂S₃/Cu₂ZnSnS₄ heterojunction thin film solar cell, *Chem. Mater.* 28 (2016) 3283–3291.
- [203] F. Jiang, S. Ikeda, Z. Tang, T. Minemoto, W. Septina, T. Harada, M. Matsumura, Impact of alloying duration of an electrodeposited Cu/Sn/Zn metallic stack on properties of Cu₂ZnSnS₄ absorbers for thin-film solar cells, *Prog. Photovoltaics* 23 (2015) 1884–1895.
- [204] D.-H. Kuo, M. Tsega, Electrical conduction and mobility enhancement in p-type In-doped Cu₂ZnSnSe₄ bulks, *Japanese J. Appl. Phys.* 53 (2014) 035801.
- [205] A.Y. Kim, T.S. Senthil, B.S. Kwak, M. Kang, Improved photovoltaic efficiency on TiO₂/In₂S₃ double layered electrodes, *Mater. Chem. Phys.* 149–150 (2015) 302–308.
- [206] Y.Q. Wang, Y.C. Rui, Q.H. Zhang, Y.G. Li, H.Z. Wang, A facile in situ synthesis route for CuInS₂ quantum-dots/In₂S₃ co-sensitized photoanodes with high photoelectric performance, *ACS Appl. Mater. Interfaces* 5 (2013) 11858–11864.
- [207] M.A. Hossain, J.R. Jennings, C. Shen, J.H. Pan, Z.Y. Koh, N. Mathews, Q. Wang, CdSe-sensitized mesoscopic TiO₂ solar cells exhibiting &5% efficiency: redundancy of CdS buffer layer, *J. Mater. Chem.* 22 (2012) 16235.
- [208] K.H. Hartstein, C.K. Brozek, S.O.M. Hinterding, D.R. Gamelin, Copper-coupled Electron transfer in colloidal plasmonic copper-sulfide nanocrystals probed by in situ spectroelectrochemistry, *J. Am. Chem. Soc.* 140 (2018) 3434–3442.
- [209] K.K. Sakimoto, A.B. Wong, P. Yang, Self-photosensitization of nonphotosynthetic bacteria for solar-to-chemical production, *Science* 351 (2016) 74–77.
- [210] G. Dong, W. Ho, C. Wang, Selective photocatalytic N₂ fixation dependent on g-C₃N₄ induced by nitrogen vacancies, *J. Mater. Chem. A* 3 (2015) 23435–23441.
- [211] H. Li, J. Shang, Z. Ai, L. Zhang, Efficient visible light nitrogen fixation with BiOBr nanosheets of oxygen vacancies on the exposed {001} facets, *J. Am. Chem. Soc.* 137 (2015) 6393–6399.
- [212] J. Li, H. Li, G. Zhan, L. Zhang, Solar water splitting and nitrogen fixation with layered bismuth oxyhalides, *Acc. Chem. Res.* 50 (2017) 112–121.